Universidad
Carlos III de Madrid

Tesis Doctoral

EMI shielding composites based on magnetic nanoparticles and nanocarbons

Autor:
María Crespo Ribadeneyra

Directores:
Dr. Javier Pozuelo de Diego
Dra. María González González

Departamento de Ciencia e Ingeniería de Materiales e Ingeniería Química
Grupo de Polímeros y Composites

Leganés, 11 de Diciembre de 2014

Universidad
Carlos III de Madrid

Tesis Doctoral

EMI shielding composites based on magnetic nanoparticles and nanocarbons

Autor:
María Crespo Ribadeneyra

Directores:
Dr. Javier Pozuelo de Diego
Dra. María González González

Firma del Tribunal Calificador

Firma

Presidente:

Dr. Humberto Terrones

Vocal:

Dra. Raquel Verdejo

Secretario:

Dr. Juan José Vilatela

Calificación:

Leganés, 11 de Diciembre de 2014

A mis padres

"... el vasto misterio de la concentración absoluta, que hace tanto al artista como al erudito, al verdadero sabio como al loco de remate, esa trágica felicidad y desgracia de la obsesión completa"

S. Zweig

Abstract

The response of nanocomposites towards electromagnetic (EM) radiation can be tailored through the electrical conductivity, permittivity and magnetic permeability. Several composites with singular microstructures and containing either conductive nanoinclusions, magnetic nanoparticles or the combination of both, have been prepared and characterized. The performance of our materials as EM interference (EMI) shields, has been determined from 1 to 18 GHz and elucidated in terms of their electric and magnetic behavior.

$Cu - Ni$ ferrite nanoparticles with varying stoichiometry were synthesized inside the pores of micro-silica particles. This inusulating, multiscale reinforcement was used to prepare epoxy composites. The EMI shielding performance of these materials was studied in order to determine the specific role of the magnetic nanoinclusions.

The combined effect of magnetism and conductivity in EMI blocking was studied in composites containing magnetite nanoparticles and carbon nanofibers (CNFs) or carbon nanotubes (CNTs). These latter were assembled into three-dimensional architectures (CNT-scaffolds and CNT-sponges) to study the interconnectivity between CNTs with regard to EMI shielding. In CNT-scaffolds, nanotubes were post-assembled with a polymeric binder. These structures showed that the conductivity and shielding ability could be up-shifted without increasing the reflectivity, since good CNT-interconnectivity is achieved at low nanotube loads. In CNT-sponges, it was observed that enhanced contact between nanotubes further improves EM blocking within the entire frequency range.

Resumen

En este trabajo se han preparado y caracterizado materiales compuestos con nanopartículas magnéticas y nanocarbonos con el fin de estudiar sus propiedades como apantallantes electromagnéticos en el rango de 1 a 18 GHz.

Se sintetizaron nanopartículas de ferrita con diferentes composiciones de Cu y Ni, usando como molde los poros de micropartículas de sílice mesoporosa. Los materiales híbridos de sílice-ferrita se incorporaron homogéneamente en una matriz epoxídica para estudiar el efecto de la carga magnética en la eficiencia de apantallamiento.

El rol de la conductividad en sí, y bajo la influencia de magnetismo, se evaluó en sistemas con nanotubos (CNTs) y nanofibras (CNFs) de carbono. Las CNFs se combinaron con nanopartículas de magnetita y fueron incorporadas en una matriz epoxi. Las propiedades electromagnéticas se estudiaron y se contrastaron con las de materiales análogos sin nanopartículas de magnetita. Con respecto a los CNTs, se prepararon dos tipos de estructuras tridimensionales: esponjas y aerogeles de CNTs. Los aerogeles se infiltraron con una resina y el alto apantallamiento electromagnético resultante sugiere que es posible favorecer la interconectividad entre CNTs formando redes segregadas del nanorefuerzo en la matriz. Este control de la nanoarquitectura, a su vez favorece la absorción de la radiación electromagnética incidente sin que en la superficie de los materiales, por el hecho de ser conductores, predomine la reflexión. Con las esponjas de CNTs, se pudo corroborar el efecto positivo de la interconectividad en el apantallamiento. En estas estructuras, los CNTs se encuentran muy cerca unos de otros y entre ellos no existen barreras poliméricas aislantes. Estos materiales ultraligeros presentaron una alta capacidad de apantallamiento en todo el rango de frecuencia estudiado.

Agradecimientos

Las tesis doctorales son documentos a los que uno tiene que enfrentarse con constancia, acompañado solamente de horas de improductividad, temores de ser un farsante, miradas inquisitivas a la pantalla brillante y monocromática o al deseo de dedicarse a tareas inútiles para evadir una etapa que se encuentra entre la figura de estudiante sempiterno y la de investigador sin un plan maestro en el bolsillo.

A pesar de este ejercicio de introspección, el autor de una tesis no es solamente quien la escribe. Javier y María, mis directores, la han escrito conmigo, con paciencia y todos los ánimos necesarios para gestar y finalmente imprimir este proyecto. Espero que con el tiempo pueda retribuirles por lo que me han ofrecido durante esta etapa, que como dice Javier, ha durado más que muchos matrimonios. Quisiera también agradecer a Juan, por permitirme ser parte del grupo de polímeros y composites, y a todos los miembros del departamento de Ciencia e Ingeniería de Materiales, que de una u otra forma han colaborado en el desarrollo de este trabajo, al igual que Mauricio Terrones, a quien le agradezco enormemente por abrirme su laboratorio, darme la oportunidad de trabajar con su equipo e inspirarme a pensar más creativamente con su ejemplo. A Yousef y a Lakshmy por su esfuerzo al ayudarme a corregir este texto.

A mi entender, toda la gente con la que convivimos aporta algo valioso a nuestras etapas vitales y ahora, en este fin de camino, me doy cuenta de que hay más personas de las que puedo nombrar antes de convertir estos agradecimientos en algo tedioso de leer. A mis compañeros de despacho, con los que hemos recorrido el camino y compartido la carga de darle sentido a nuestras tesis. Gracias a su ayuda, he podido completar muchas partes de este trabajo que no las habría podido hacer sola. Al resto de amigos con quienes todo este proceso se ha tornado más emocionante, al combinar el lindy con los capacitores, la reconstrucción de mi casa con las lecciones de extrusión de aceros, los tamales y los materiales 2D, al mezclar las artes culinarias con el saber hacer scaffolds o a entender la similitudes entre la física y la economía o la neurociencia.

Finalmente tengo que agradecer a mi familia. Son los que se quedan conmigo velando las armas antes de cualquier batalla. Esto se extiende también a los nuevos miembros. Al que ha sido referente de constancia y al que ha actuado como agente de bibliografía, reparador de gráficos, corrector de barbaridades matemáticas, reanimador múltiple o terapista.

Gracias a todos por su apoyo.

Contents

Abbreviations

CNF	**C**arbon **N**ano**F**iber
CNT	**C**arbon **N**ano**T**ube
MWCNT	**M**ulti**W**alled **CNT**
CNxCNT	**N**itrogen-doped **CNT**
3D	**T**hree **D**imensional
EM	**E**lectro**M**agnetic
EMI	**E**lectro**M**agnetic **I**nterference
SE	**S**hielding **E**fficiency
SE$_T$	**T**otal **S**hielding **E**fficiency
SE$_A$	**A**bsorption **S**hielding **E**fficiency
SE$_R$	**R**eflection **S**hielding **E**fficiency
CVD	**C**hemical **V**apor **D**eposition
NP	**N**ano**P**article
ICP	**I**ntrinsically **C**onductive **P**olymer
IPDT	**I**ntegral **P**rocedure **D**ecomposition **T**emperature

INSTRUMENTAL TECHNIQUES

XRD	**X** **R**ay **D**iffraction
BET	**B**runauer **E**mmett **T**eller surface area
BJH	**B**arret **J**oyner **H**aelender pore distribution
VSM	**V**ibrating **S**ample **M**agnetometry

TGA	**T**hermo **G**ravimetric **A**nalysis
DSC	**D**ifferential **S**canning **C**alorimetry
SEM	**S**canning **E**lectron **M**icroscopy
TEM	**T**ransmission **E**lectron **M**icroscopy
SAED	**S**elected **A**rea **E**lectron **D**iffraction
VNA	**V**ector **N**etwork **A**nalyzer
DC	**D**irect **C**urrent measurements
AC	**A**lternating **C**urrent measurements

Physical Constants

Speed of Light	$c = 2.997\ 924\ 58 \times 10^{8}\ m \cdot s^{-1}$
Vacuum permeability	$\mu_0 = 4\pi \times 10^{-7}\ H \cdot m^{-1}$
Vacuum permittivity	$\epsilon_0 = 8.854\ 187\ 817 \times 10^{-12}\ F \cdot m^{-1}$
Impedance of free space	$Z_0 = 377\ \Omega$
Imaginary unit	$j = \sqrt{-1}$
Shape factor for spherical crystallites	$K = 0.9$

Symbols

Symbol	Name	Unit
ω	angular frequency	$rads^{-1}$
f	frequency	Hz
P	power	W $(J \cdot s^{-1})$
ρ	density	$g \cdot cm^{-1}$
μ	complex permeability	$H \cdot m^{-1}$ $(\Omega \cdot s^{-1}m^{-1})$
μ_r	complex relative permeability	dimensionless
μ'	real component of μ_r	dimensionless
μ''	imaginary component of μ_r	dimensionless
ϵ	complex permittivity	$F \cdot m^{-1}$ $(s \cdot \Omega^{-1}m^{-1})$
ϵ_r	complex relative permittivity	dimensionless
ϵ'	real component of ϵ_r	dimensionless
ϵ''	imaginary component of ϵ_r	dimensionless
η_B	magnetic moment	$Nm \cdot T^{-1}$
H_C	coercitivity	Oe
M_r	remanent magnetization (remanence)	$emu \cdot g^{-1}$
M_s	saturation magnetization	$emu \cdot g^{-1}$
SE	shielding efficiency	dB
SSE	specific shielding efficiency	$dBcm^3 \cdot g^{-1}$
f_m	matching frequency	Hz
t_m	matching thickness	mm

R	resistance	Ω
σ	conductivity	$S \cdot cm^{-1}$
Z	impedance	Ω
δ	skin depth	mm
$\vec{E}$	electric field	$V \cdot m^{-1}$
$\vec{J}$	electric flux	Vm
λ	wavelength	cm^{-1}
λ_m	matching wavelength	cm^{-1}
θ	diffraction angle	degrees ($^\circ$)
β	diffraction peak broadening	$rads$
D_C	critical diameter	nm
T_g	glass transition temperature	$^\circ C$
ϕ	volume fraction	$vol\%$
ξ	tunneling distance	nm

CHAPTER 1

INTRODUCTION & OBJECTIVES

Electromagnetic interference reduction: Suitable materials and procedures

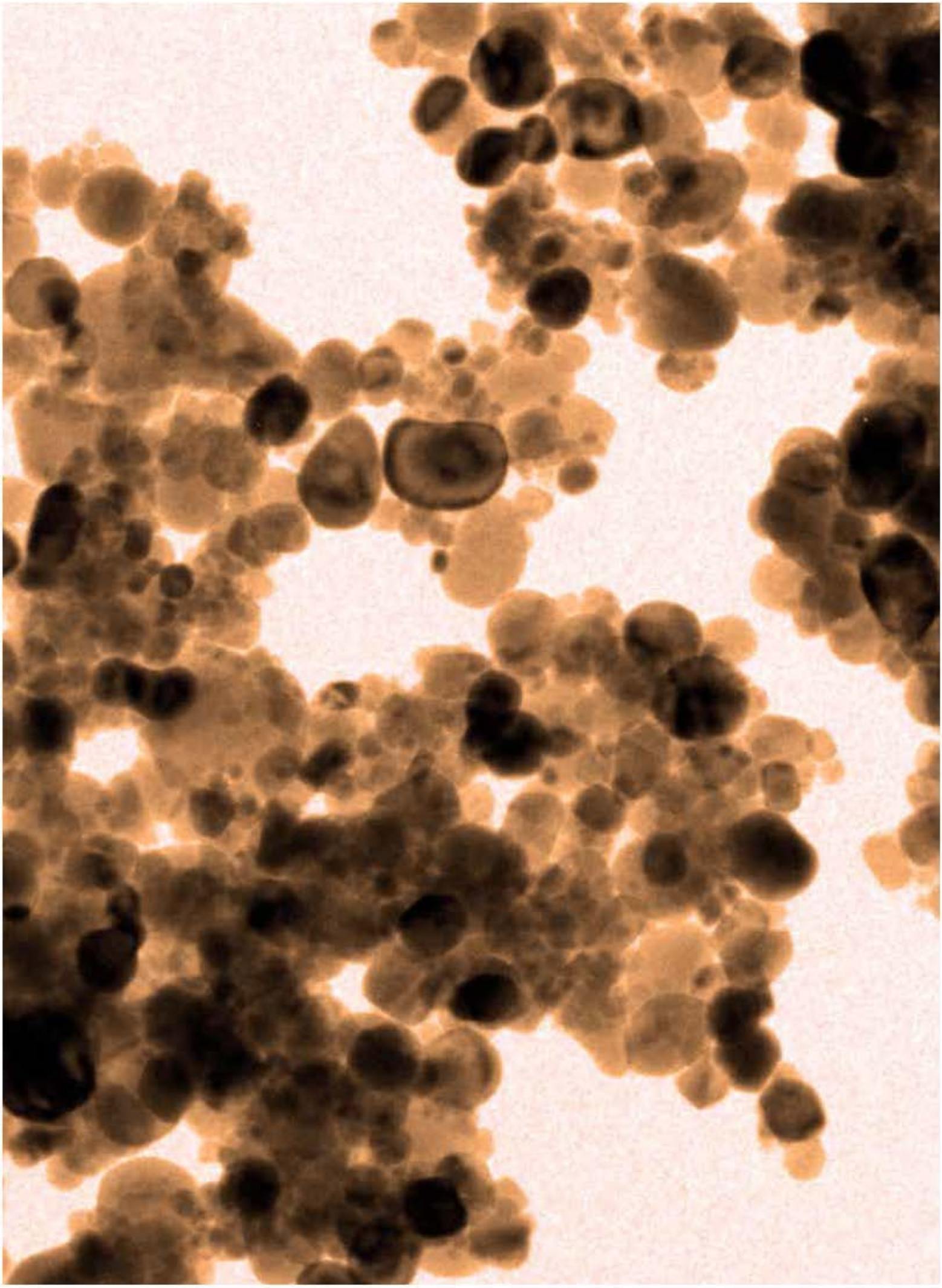

Introduction & objectives

1.1 Introduction to EMI and challenges for nontraditional shielding materials

Electromagnetic interferences (EMI) occur when EM signals are unintentionally transmitted by radiation and/or conduction, causing electrically operated elements to behave improperly [1]. A good example to illustrate the combination of both interference mechanisms is a power cord from a device connected to domestic electric supply (AC current) [2], intended to provide 50-60 Hz but in which higher frequency signals are also present. High-frequency signals can radiate out from the power cord as they are conducted. Alongside, the cord can behave as an antenna, picking up external radiation and transferring the outward signals to the circuit elements of the device. EMIs affect all electrical and electronic devices which are increasingly becoming more indispensable for the society.

Conduction coupling of EM signals is the primary path of interference in electronic circuits and can be circumvented by the circuit design and through the use of frequency filters or inductors. Radiation on the other hand, can be avoided by isolating the source (or the receiver) with a physical shield. EMI shielding is thereby devoted to suppress or attenuate EM radiation from emitters with materials that are able to interact with those signals.

Shields can disable an EM wave to penetrate into a certain space through reflection and/or by an absorption-dissipation process [3]. Conventionally, conductive metallic panes and meshes are used for isolating spaces or devices by reflecting the radiation. The concept of pure reflection shielding can be associated to Faraday cages, where the inside space is totally inaccessible to external electric fields. Shielding through absorption instead, is normally related to materials that are magnetically permeable

(ferro and ferrimagnetic materials). Magnetic absorbers prevent the incident magnetic field to propagate in other spaces by concentrating the field within themselves. In the case of metallic conductors, their heaviness, lack of flexibility and high costs of processing, are the main disadvantages. In addition, ferro and ferrimagnetic materials have an intrinsic cut-off frequency, normally below or not far from the low-GHz range, which restricts their use for GHz-shielding applications.

One of the present needs is thus to find broad-band shields, able to neutralize EM radiation not only among the MHz band, but up to the GHz range. This requirement arises from the fast development of electronics, which has led to microprocessors with greatly enhanced data transfer speeds that operate at higher frequencies. Furthermore, the miniaturization of such components demands high performance and lightweight materials for its manufacture. Apart from the proper electronic and electric circuitry performance, there is also an ever-growing awareness of the society to high-frequency EM pollution and its effects on human health [4].

The concern of EMI pollution is not restricted only to consumer electronic products. Due to the wide impact of telecommunications, several economically heavy industrial sectors are likewise eager on the progress of EMI shielding materials. These technological fields demand not only efficient shields, but also materials that meet specific criteria for each engineered design. For example, chemical and corrosion resistance, lightweight, flexibility, tunable morphology, processing easiness, and inexpensiveness are requirements that materials must fulfill in order to be applicable in flexible electronics (e.g. personal computers and mobile phones) or in aerospace (e.g. satellite and aircraft's manufacture) and automotive (e.g. integrated circuits) industries [5]. Another priority is the development of radar-absorbing materials for military stealth. Much effort has been made in this direction although total absorption of EM energy is still challenging because one needs to simultaneously minimize reflection in order to maximize absorption [6].

1.2 Design solutions: Polymer composites with carbonaceous and magnetic inclusions

Polymers offer several advantages over traditional metals and ceramics used for EMI shielding. They can be easily shaped into a wide variety of morphologies and are substantially lighter. Although polymers are *per se* electromagnetically transparent, different strategies are available to convert them into active EM shields.

To block magnetic fields, magnetically permeable particles such as spinel ferrites or ion-nickel alloys can be combined with polymers [7]. In addition to weight reduction, the incorporation of nanoparticles of these magnetic materials might enable to surpass their intrinsic cut-off frequency [8,9]. This can be traduced in broader band EMI shielding. Thereby, a fair amount of research is currently focused on the production of magnetic nanoparticles for the preparation of efficient shielding composites [10]. Moreover, interactions of magnetic nanoparticles with high-frequency EM fields are still not adequately understood and additional basic knowledge is needed to promote developments in this technological field.

Intrinsically conductive polymers (ICPs) and polymer composites with conductive particles are the preferred alternatives to shield radiated electric fields. These materials shield mainly by reflecting the incident EM radiation. Thus if the conductivity of the composites is low, so will be their ability to block of EM energy. Polypyrrole and polyaniline are the most frequently employed ICPs. They have been mixed with non-conductive polyester fibers [11] and polyvinyl chloride [12], polyurethane [13], polystyrene or Poly(methyl methacrylate) [14] matrices. In all these examples the non-conductive polymer is used to assure the mechanical integrity of the mixture, because ICPs are normally brittle. The drawback in most cases is the high load of ICP that is needed to attain high conductivities, which is detrimental for the processability of the blends [15].

In the case of composites with conductive inclusions, the two main alternatives are metallic and carbonaceous particles. For both options, it has been reported that EM shielding is enhanced with electrical conductivity [3]. Therefore, the tendency of using high aspect ratio particles has grown rapidly. Metallic particles of Ni [16], Ag [17] or Cu [18] and Al flakes [19], were first extensively incorporated in polymers such as polyimidesiloxane, polyurethane resins or polyethersulfone. Next, epoxies and thermoplastics loaded with higher aspect ratio conductive stainless steel fibers [20] or metallized glass [21], polyester [22] and carbon fibers [23] shifted the attention away from particles. And more recently flexible polymeric composites loaded with copper [24,25] or silver [26] nanowires have been reported. However, purely metallic particles are prone to corrosion, and in addition, it is difficult to obtain good dispersions with their incorporation into polymers. Carbonaceous particles in contrast, have gained increasing attention since they are chemically resistant, lightweight and are more compatible with polymers.

Graphite, carbon black and carbon fibers were the first to be combined with polymers for the fabrication of EMI shields [3,27,28]. The attention increasingly changed to nanocarbons since more conductive composites can be obtained with lower weight fractions of nanocarbons. In addition, to enable the entire cross-section of a filler to be active in shielding, the dimensions of the conductive filler should be comparable to, or be less than the rate of penetration of the incident radiation [29]. This rate of penetration is usually very small for good conductors at high frequencies. Thereby, nanodimensional carbon fillers could be adequate to shield in the GHz range.

In this context, carbon nanofibers, nanotubes and graphene, which have higher specific surface area and aspect ratio than their microscale analogues, are promising candidates for the preparation of efficient EMI shielding composites. Despite having been studied expansively in recent years, several factors affecting the performance of nanocarbon/polymer composites as high-frequency EM shields remain unexplored or not completely understood. Indeed, there are few reported reviews on the use of nanocarbons

for EMI shielding[30–33], which point out the need of new and reproducible experimental data that can facilitate the construction of realistic models.

The morphology of nanocomposites can be tailored through different strategies (e.g. spatial distribution of the nanophase, porosity of the matrix, assembly into complex macroscopic configurations), which opens a wide research field. Besides, the unique chemical nature of nanocarbons allows for their combination with a variety of species, which in turn permits the modification of the EM properties of composites. Particularly, hybrids including magnetic nanoparticles and nanocarbons might enhance the EM absorption ability of composites[31,34–38]. Thus, understanding these interactions is a key factor for the development of lightweight and high-performance EM absorbing materials.

1.3 Shielding efficiency: Reflection/absorption terms and their relationship with permeability and permittivity

Figure 1.1 illustrates the possible interactions of EM waves with matter. When the wave reaches the front-face of the material (input surface), part of the incident power is reflected. Alongside, the non-reflected power is transmitted into the sample. As the wave passes through, it can be absorbed and dissipated or transmitted out from slab.

Through this basic reflection and transmission concepts, it is possible to define the total shielding efficiency (SE_T). This parameter measures how well a material impedes EM energy of a certain frequency to pass through it. SE relates the incident EM energy to the transmitted one as:

$$SE_T = 10 \log \frac{P_I}{P_T} = 20 \log \frac{E_I}{E_T} = 20 \log \frac{H_I}{H_T} \tag{1.1}$$

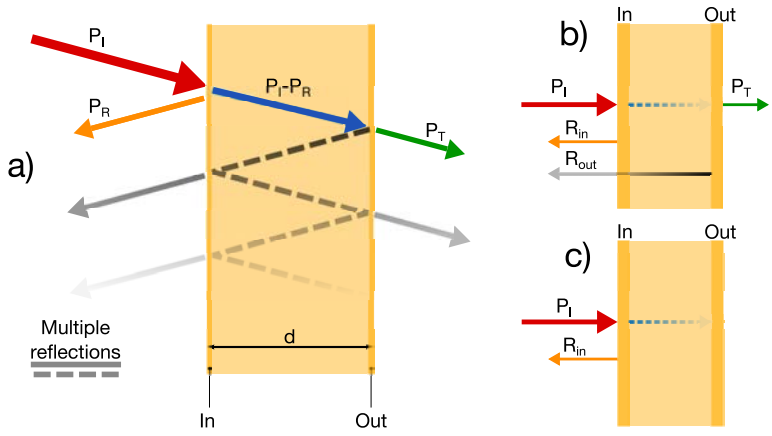

FIGURE 1.1: a) Possible reflection P_R and absorption P_A mechanisms of attenuation of the incident EM power P_I when it strikes a finite-dimensional media [39]. Sources of reflection (input and output interfaces, R_{in} and R_{out}) in electromagnetically thin (b) [40] and electromagnetically thick slabs (c) [25]

where SE_T is a logarithmic ratio, and therefore is given in decibels (dB); subscripts T and I respectively represent the transmitted and incident components and P, E and H refer to power and electric or magnetic field intensities respectively.

Taking into account that shields will either reflect or absorb (Figure 1.1) striking EM waves, the global SE (SE_T) can be rewritten as [41]:

$$SE_T = 10 \log \frac{P_I}{P_T} = SE_R + SE_A \tag{1.2}$$

$$SE_R = 10 \log \frac{P_I}{P_I - P_R} \tag{1.3}$$

$$SE_A = 10 \log \frac{P_I - P_R}{P_T} \tag{1.4}$$

where SE_A refers to shielding due to absorption and SE_R due to net reflection. Note that the term net involves the contributions of secondary reflections (output interface, Figure 1.1a and b) that occur in finite-dimensional media. These additional reflections are termed multiple reflections and their negative or positive contribution to global

shielding (SE_{MR}) can be neglected when the thickness of the shield is greater than depth of penetration of the wave (δ) or when SE_A is higher than 10 dB [42] (Figure 1.1c).

The depth of penetration, or the skin depth (δ), is defined as the thickness underneath the external surface at which the incident field is attenuated to $1/e$ of its initial value. This is equivalent to a power decay of about 9 dB ($20\log(1/e)$) within one skin depth [41,43,44]. For conductive materials, a 63.2% of the current flows within this superficial cross-section and 99% of the current flows within ∼4.6 skin depths.For electromagnetically thick monolithic shields (Figure 1.1c, when SE_{MR} can be ignored) SE_R can be expressed in terms of the impedance ratio between free space (Z_0) and the surface of the material (Z_{in}); and SE_A as a function the shield thickness (d) and its skin depth (δ) by: [1]

$$SE_R + SE_A = 20\log\frac{Z_0}{4Z_{in}} + 20\log e^{\frac{d}{\delta}} = SE_T \tag{1.5}$$

where $Z_0 = 377\Omega$ for a plane EM wave (far field). Thereby, reflection of the wave inherently occurs due to the impedance discontinuity that it encounters when striking a medium with different impedance than air. In contrast, absorption requires the existence of magnetic and/or electric dipoles that enable the interaction of the material with the incident EM energy. It can be seen that the extent at which absorption occurs depends upon the depth of penetration (δ) of the wave and the ability of the material to dissipate the field within its thickness (d). δ decreases with frequency (f), conductivity (σ) and permeability (ϵ) as shown by:

$$\delta = (\pi f \sigma \mu)^{\frac{-1}{2}} \tag{1.6}$$

For conductive monolithic shields SE_R and SE_A can therefore be rewritten in terms of σ and δ as [1,45]:

$$SE_R = 20 \log \frac{Z_0}{4Z_{in}} = 39.5 + 10 \log \frac{\sigma}{2\pi f \mu} \tag{1.7}$$

$$SE_A = 20 \log e^{\frac{d}{\sigma}} = 8.7 \frac{d}{\delta} = 8.7 d \sqrt{\pi f \mu \sigma} \tag{1.8}$$

where it can be seen that the reflection SE depends solely on σ/μ, while the absorption term is a function of $\mu \cdot \sigma$ and the sample thickness. This explains why non-magnetic metals (very low impedance) are prone to shield mainly by reflection while in magnetically permeable shields, even if they are conductive, SE is mostly related to attenuation rather than to reflection.

However the situation is quite different in composites. Although the above equations allow to qualitatively describe the tendency of SE_R and SE_A with frequency, conductivity and permeability, composites have a highly heterogeneous microstructure that is responsible for great variations in the local fields [31]. Here the nano and microscopic boundaries act as polarization sites, which generate the lag of the displacement current with respect to the conduction current. This is represented by the effective permittivity (ϵ) of the composite, in replacement of the conductivity of bulk metals[1].

Thus, both ϵ and μ would define how electric and magnetic fields interact with composite shields. These magnitudes are described by an imaginary component (ϵ'' or μ'') related to the loss of energy and a real component (ϵ' or μ''), which gives information about the stored EM energy [47]. In composites, since the matrix and the inclusions have very dissimilar electrical and magnetic properties, their bulk ϵ and μ are respectively referred to as effective permittivity and permeability. These effective properties depend on the complex association of ϵ and μ of each constituent, as well as on their volume fraction, geometry and conductivity [48,49].

[1] Permittivity represents the ratio of displacement current to conduction current, which in metals is small. Metals are not able to support the formation of an electric field within themselves, as the electric field ($\vec{E}$) is equal to the product of conductivity (σ) and electric flux ($\vec{J}$), which implies that for infinite conductivity, the electric field tends to be null [46].

In the case of magnetic inclusions, for EMI suppression it is thus beneficial to avoid high conductivities, to limit front-face reflection, and have a high effective permeability. In such situation, the material will be receptive to the magnetic field (high μ') and at the same time will be able to dissipate it (high μ'').

For composites with conductive inclusions such as nanocarbons, desired effective permittivity values will strongly depend on the final application. In a general way, composites with higher global SE are obtained whenever the conductivity is enhanced. Conductivity increases with the fraction of nanocarbons in the matrix. The imaginary part of the permittivity, which represents the loss of energy (ϵ'') and is related to ohmic and dielectric losses indistinctly [50], follows the same trend. Accordingly, increasing the fraction of nanocarbons in the matrix enhances the number of interfaces prone to polarization and therefore ϵ' increases as well. In such situation, reflection and absorption might be enhanced simultaneously, because both paths of EMI suppression are governed by the electrical conductivity of the shield ($SE_A \propto \sigma \cdot \mu$ and $SE_R \propto \sigma/\mu$).

Owing to this counter effect, for applications such as radar absorbing materials it is necessary to adjust the composites effective permittivity to certain values by which reflection can be minimized. This might be done for example, by adjusting the fillers weight fraction to the most optimum value, by adding a magnetically permeable component or by selecting low dielectric constant (ϵ') matrices. These strategies therefore permit to tune the composites reflectivity/absorptivity against EM waves, which is an added advantage over traditional bulk metals that are mostly limited to reflection.

1.4 Magnetic Nanocomposites

1.4.1 Magnetic nanoinclusions: size effects in permeability

The requisite for GHz magnetic shielding is that the material conserves its magnetic permeability value at this frequency range. The frequency of magnetic resonance (f_r)

represents the cut-off frequency of magnetic materials, since it is the value at which the permeability sharply vanishes. Both magnitudes (μ and f_r) are related to the saturation magnetization (M_s) by the Snoek's limit, $f_r(\mu_r - 1) \propto M_S$ [8]. Therefore, to obtain non-null values of μ at high f_r, a high M_s would also be necessary.

Ferromagnetic metals and alloys (Fe, Ni, Co) have high M_s and specific combinations do have a great permeability. Nevertheless, due to their highly conductive nature [51], eddy current losses[2] provoke permeability to drop at lower frequencies than expected (50 KHz-10 MHz). Ferrites in contrast, are semiconducting and their electrical resistance is several orders of magnitude higher than that of ferromagnetic metals and alloys. The primary drawback in this case is that their M_s is significantly lower and thereby, the f_r lays below few GHz. Both situations limit the use of most of these magnetic materials in their bulk form for EMI absorption in the GHz range.

Nonetheless, when the dimension of magnetic particles is below a critical small size, eddy current loses become negligible and the anisotropy energy has additional effects of size and surface [54,55]. These effects become predominant due to the breaking of a large number of exchange bonds [56]. Changes in the anisotropy energy lead to the modification of the spin relaxation time/frequency when the particle size/surface is varied. In this context, the dispersion of permeability in composites loaded with magnetic nanoparticles is governed by relaxation mechanisms rather than by the intrinsic resonance observed in bulk magnets [57]. According to the relaxation theory of magnetic moments, permeability can be thus maintained at a constant value until relaxation [58]. For fine nanoparticles, relaxation would coincide with the transition from a superparamagnetic to a ferromagnetic state. In superparamagnetic nanoparticles the magnetic spin fluctuates very rapidly and accordingly, relaxation is expected to occur at high frequencies (GHz).

[2] Eddy currents are closed loops of induced current that generate within conductors when subjected to changing magnetic fields [52]. These currents create magnetic fields that oppose to the source field, causing the skin effect on conductors carrying AC-current [53]. Eddy currents might provoke low-frequency shifts of the EM loss peak in ferromagnetic materials [7].

Small size effects have been observed in carbon-coated Ni nanocapsules in which relaxation occurred at 5.5 GHz thus, surpassing the value of the bulk material (several tens of MHz) [59] in the same maner than in $(Fe, Ni)/C$ nanocapsules [60]. Furthermore, superparamagnetic relaxation exceeding the natural resonance frequency has been predicted for systems of Fe nanoparticles [61] and experimentally corroborated for composites with 9 nm magnetite nanoparticles [62]. More recently, further anisotropy effects have been reported for ferromagnetic nanocomposites loaded with Fe-Co nanoparticles [63]. These particles were assembled into a uniaxial structure by applying an external magnetic field during polymerization of styrene. Composites showed magnetic anisotropy along the magnetization direction and the frequency of superparamagnetic resonance was seen to occur at 6.8 GHz, which was higher than that of composites prepared without any uniaxial anisotropy.

However, to be able to use magnetic nanoparticles in the preparation of efficient magnetic composites, parameters such as the physical contact between particles should also be controlled. Contacts can be viewed as dipole-dipole interactions that would obstruct the spin fluctuation [64] and would frustrate the effect of the small size of nanoparticles in the enhancement of the frequency of relaxation. Therefore, both the size and shape of the nanoparticles, and their aggregation within the matrix, should be carefully considered when designing magnetic composites for GHz-EMI absorption.

1.4.2 Advances in magnetic composites for EMI absorption: dispersion and nanoparticle size control

The synthesis of size-controlled magnetic nanoparticles within polymer matrixes may be accomplished either by in-situ polymerization during particle formation [65,66] or by dispersing preformed magnetic nanoparticles in the polymer matrix. In this latter case, many routes for synthesizing size-controlled particles involve the use of capping agents [67], precipitation in reverse microemulsions [68], or sol-gel processing [69] to avoid

their coalescence and further growth. Nevertheless, since geometry is also important, other methods that allow the synthesis of shape-controlled particles are being explored [67]. Nanocasting is a useful technique that involves using a template (either soft or hard), which is impregnated by liquid precursors of the particles [70]. Finally, homogeneously dispersed nanoparticles within the template are obtained as the negative image of the tamplate. Silica is one the most widely used hard templates, since its geometry is stable and can be obtained with different pore shapes and sizes *via* sol-gel [71]. Nanocasting using hard templates has been successfully employed for the preparation of ferrites with several transition metals as Cu, Co, Ni, Pd, Zn [72–75].

Despite many years of research [76–79], it remains challenging to achieve good and reproducible dispersions of nanoparticles in polymers [80,81]. In this context, surface modification is an alternative to avoid agglomeration. This method is expected to improve nanoparticle-polymer interactions either through weak Van der Waals forces or strong chemical bonds [82,83]. Silica coated magnetic nanoparticles have also been proposed as an alternative to increase compatibility and to avoid oxidation [84,85]. In addition, enhanced EMI absorption of such core-shell type structures has been reported [86,87]. Owing to the dielectric nature of the shells, in composites with SiO_2-coated Fe_3O_4 nanoparticles [88], Al_2O_3-coated $FeNi_3$ nanoparticles [51], Fe nanoflakes coated with SiO_2 [89], ZnO-coated Fe nanocapsules [90], or Co/graphite nanoparticles [91], enhanced interfacial polarization contributions and a better impedance matching has been observed.

Incorporation of magnetic nanoparticles within micron-sized mesoporous silica can also be found in literature as an alternative to facilitate the dispersion of the particles in epoxy resins [92]. This type of combination can enhance other properties of the matrix, as it has been described that pristine porous micron sized-silica improves the mechanical performance (fracture toughness, modulus, and deformation at break) and thermal stability [93,94]. When considering magnetically loaded polymer composites

for EMI shielding, it is well established that electromagnetic absorbers dissipate electromagnetic energy into heat. Therefore, materials which combine enhanced thermal stability, magnetic activity and lightweight, could be prospective candidates for this application.

1.5 Composites with nanocarbons

1.5.1 Shielding with nanocarbons

Although many studies do not separately report absorption and reflection contributions to the global SE, the general trend for composites with different carbonaceous nanoinclusions[31,32,95,96] is that SE is enhanced with electrical conductivity. Consequently, their SE depends on the nanofiller weight percentage as well as on its aspect ratio[97]. Hence, it has been reported that values of SE around 20 dB (desired value for most emerging applications) could be reached with 15 wt% of carbon black (CB), 5-10 wt% carbon nanofibres (CNF) and only 2-3wt% of multi-walled carbon nanotubes (MWCNTs)[43]. Moreover, due to its high electrical conductivity and high specific surface area, chemically derived graphene has also been included to the list of carbon nanofillers for EMI shielding applications[98–101]. For example, the SE of a CVD-grown graphene monolayer has shown a value of 2.27 dB, which corresponds to seven times the SE value of gold films with the same thickness[102].

Since the electrical conductivity of the composites depends on the dispersion degree of the nano-conductive filler, SE values above 20 dB have been achieved with high filler loadings (e.g. 20wt%), a fact that is neither economically desirable nor viable for processing. There are only few published works in which this target SE value has been attained with low loads (2-3wt% of MWCNTs)[43]. In most cases, reasonable SE values have only been achieved with loadings up to 20 wt% of single-walled CNTs[103–105], 5 and 10 wt% of MWCNTs[106] or 15 wt% of chemically derived graphene[100]. It

is worth emphasizing that high filler loadings are not suitable because the desired weight-reduction of the composites increases and high filler loads could induce unwanted particle agglomeration that significantly reduces the efficiency of the filler. It is therefore necessary to avoid high filler loadings and use alternative processes that ensure good filler dispersions and interconnectivity.

1.5.2 Dispersion of nanocarbons: advanced methodologies to attain high conductivity at limited nanocarbon loads

Numerous proposals on how to transfer the unique axial properties of CNTs and graphene to composites have been driven [107]. The benefits of good dispersions are directly related to the bulk properties of composites, e.g. enhanced tensile strength or high electrical and thermal conductivity at low percolation thresholds. Furthermore, the EM properties of composites having embedded filler particles are not solely function of their intrinsic properties. Interparticle interactions, such as filler clustering or polymer chain adsorption onto the filler surface, play an important role. Clustering, or aggregation, for example is a main issue that has extreme influence in polarization mechanisms and has been proven to alter the frequency dispersion of permittivity in such composites [108].

As for other nanodimensional fillers, in-situ polymerization [109], surface functionalization [110] or combination with surfactants [111], have been pursued to enhance the dispersion of nanocabons. Nevertheless, in most approaches disaggregation is done with high-energy dispersion techniques that can reduce the aspect ratio of nanocarbons, while chemical functionalization might truncate the electronic conjugation of graphitic structures. Both situations are detrimental for the electrical conductivity of nanocarbons. In contrast, those methodologies that explore the formation of segregated nanofiller networks [112] allow to elude the challenge of dispersing the nanofillers

within large matrix volumes, e.g. double percolation concept[113] (Figure 1.2). Additionally, the preferential localization of the conductive filler within the matrix enables an increase in the bulk conductivity of the composite at low fractions[114].

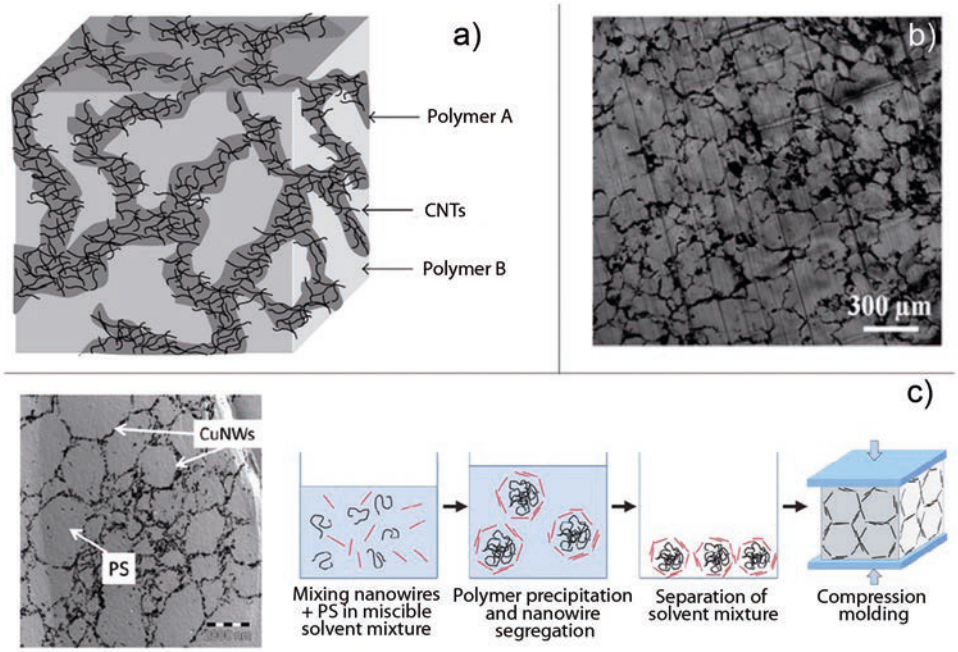

FIGURE 1.2: a) Double percolation found in materials were the filler is dispersed in a polymer A not mixable with B, which therefore forms segregated networks within the composite[115]. b) Segregated composites of graphene[116] and c) Cu-nanowires[117] prepared through solvent-assisted segregation/precipitation and subsequent hot compresion molding (d)[118]

Having in mind that weight reduction is always beneficial, some materials that incorporate this concept are CNT and graphene polymeric aerogels, foams and scaffolds[119] (Figure 1.3a, b and c). These materials are extremely lightweight and exhibit ultralow percolation thresholds[118]. Examples include microcellular foams of graphene (5 wt%) with electrical conductivities of 3.11 S/m and SE values of 15 dB[120], ultra light MWCNT aerogels (>1 wt%) with electrical conductivities of ca. 3.2 S/m[117], or

CNTs and CNFs polystyrene composite foams in which SE values of 19 dB and 9 dB were achieved with loadings close to 7 wt% of CNTs and CNFs, respectively[115].

These porous structures can be infiltrated or impregnated with polymers to enhance their mechanical performance (Figure 1.3d). Through polymer infusion, the conductive skeleton remains unaltered, thereby it is expected that composites attain high electrical conductivities and SE values even for virtually low filler loads. Indeed, very recently highly electrically conductive nanocomposites based on epoxy-infused graphene sponges were reported. In comparison to the neat epoxy, these materials showed an increase in conductivity of 12 orders of magnitude with graphene loads of only 2 wt%[121].

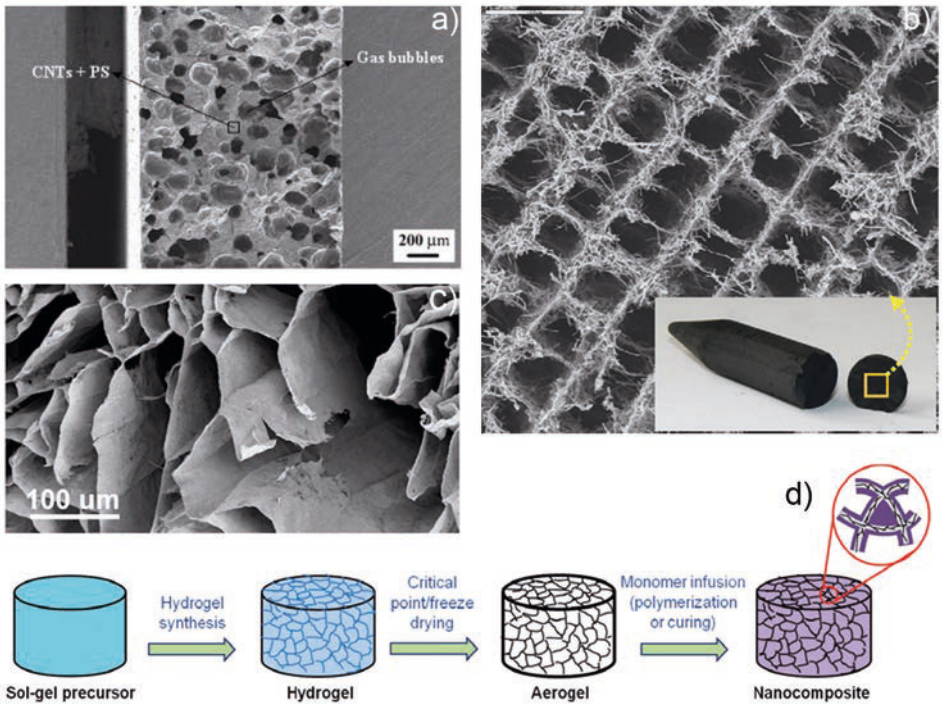

FIGURE 1.3: Lightweight CNT structures prepared with polymer binder and CNT dispersions: a) foams, b) scaffolds and c) aerogels. d) Illustrative scheme of the process for preparing percolative composites with low fractions of reinforcement by the infiltration of aerogels that are obtained by freeze-drying the preformed cryogels

Beyond the double percolation concept are the pioneering macroscopic structures of nanocarbons, which can be directly synthesized through CVD routes. Some examples include highly conductive continuous CNT [122] fiber and CNT-sponges [123,124] (Figure 1.4). In these structures polymer binders do not limit the connectivity between adjacent nanotubes, as in the case of aerogels foams and scaffolds, and in addition, CNTs are forming highly interlinked networks within macroscopical volumes. Since SE is favored by conductivity, it is expected that these structures present enhanced EMI shielding performances.

Recently a template-assisted CVD route has been successfully employed to fabricate graphene foams, without any polymer binder [125]. This graphene-based 3D interconnected network has shown outstanding values of specific SE in the X-band (∼333 $dBcm^3/g$) and electrical conductivities of about 100-120 $S \cdot cm^{-1}$. Conversely, the procedure involves an additional polydimethylsiloxane impregnation step to mechanically reinforce the porous structure; while the polymer does not interfere with the connectivity of the conducting nanomaterial, it does increase the bulk density of the foam.

It is therefore clear that the preassembling of nanoparticles into macroscopic architectures enables obtaining composites with a well-defined spatial distribution of nanoconstituents. Since the properties of composites are directly linked to the interactions between nanoparticles, the control of the nanophase's microscopic distribution is essential: The bulk characteristics of composites can be influenced by the modification of the nanoarchitecture [128]. Additionally, the drawback of working with fine powders of isolated nanoparticles can be avoided when they are assembled into easy to handle macroscopic solids. The direct applicability of this kind of nanomaterials in diverse technological fields is thereby enormously enhanced [129].

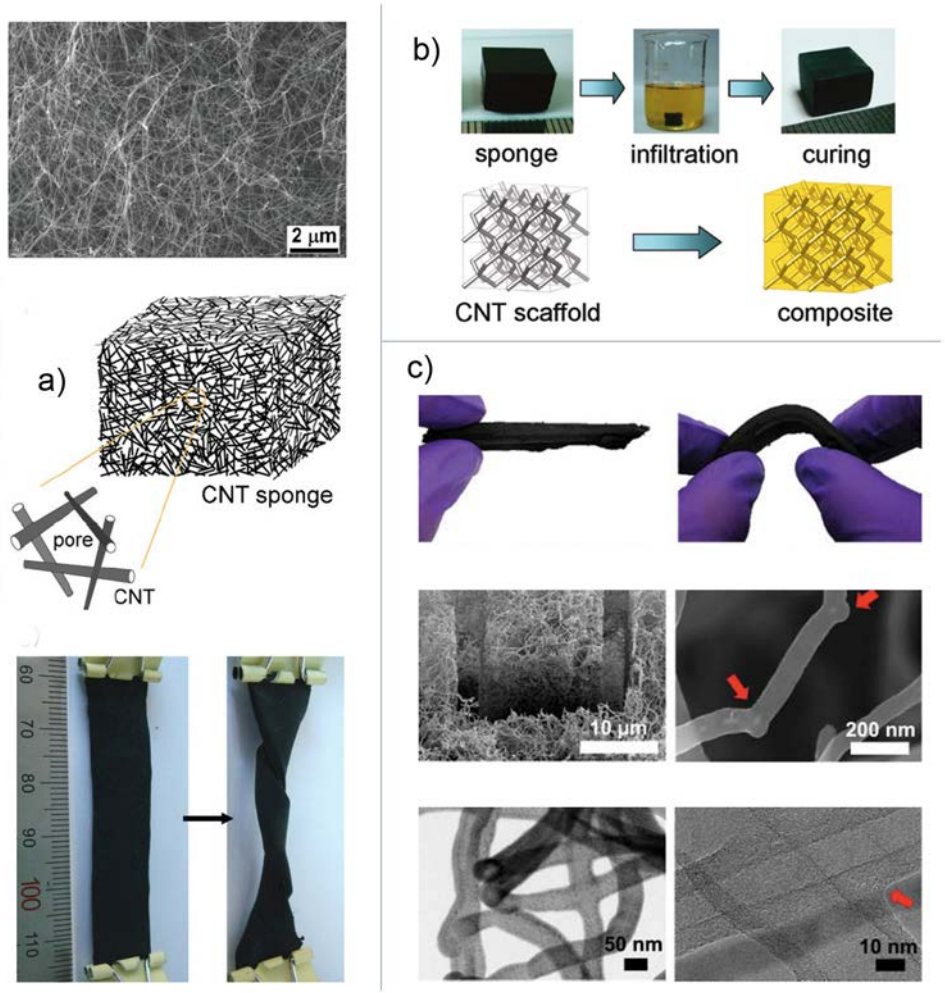

FIGURE 1.4: a) Flexible and highly porous CNT-sponges directly prepared through CVD [123], b) CNT-sponge infiltration with polymer for obtaining highly percolating CNT-sponge composites [126] and c) flexible and bendable boron doped CNT sponges in which the boron-induced entanglements and elbows are responsible of the spongy character [127]

1.5.3 Approaches to minimize reflection

One of the major goals in the development of conductive EMI shielding composites is to limit reflection and enhance absorption. However, reflection occurs prior to absorption and depends on the extent of non-reflected power at the material's front-face. Perfect transmission into the material or null reflection, is achieved when the surface impedance of the shield equals the impedance of free space, which is practically impossible to satisfy with monolayer shields. Methods to limit reflection are thus devoted to minimize the mismatch of impedance that waves suffer when they strike conductive materials.

The intrinsic surface impedance of a given medium is related to its complex permittivity and permeability as shown by:

$$Z_{in} = \frac{|E|}{|H|} = \sqrt{\frac{j2\pi f\mu}{\sigma + j2\pi f\epsilon}} \tag{1.9}$$

where j is the imaginary unit and denotes that μ and ϵ are complex numbers, e.g. $\mu = \mu' - j\mu''$ and $\epsilon = \epsilon' - j\epsilon''$. In composites both effective magnitudes are complexly ascribed to the individual properties (geometry, size, conductivity) and volume fractions of each constituent. Thus, in a very simplified view there are three possible alternatives to lower the impedance mismatch: Increasing the effective permeability, decreasing the conductivity or decreasing the effective permittivity. To increase the effective permeability and counteract the electric loss, as carbons are intrinsically non-magnetic, the only option is to combine them with magnetic particles. Decreasing the conductivity of composites with conductive inclusions is detrimental for their shielding performance, as SE_A is increased with conductivity. In regard to the effective permittivity as previously addressed, the imaginary part is related to ohmic and dielectric losses, thus it is directly related to the conductivity of the composite. Therefore, lowering its magnitude is also detrimental for EMI absorption. However, the effective permittivity has the contribution of the real part as well, which can be tuned to compensate the ohmic losses of the imaginary part. This can be done by reaching

adequate conductivities while limiting the fraction of nanocarbons and by compositing the conductive filler with low dielectric constant matrices ($\epsilon = 1 - j0$) such as air.

Therefore, foaming is a tentative approach to limit the weight of composite EMI shields and also to decrease the impedance mismatch with striking plane EM waves[32]. In this context, foams can show enhanced EM absorption (lower front-face reflection) and also better heat dissipation of the absorbed energy, owing to their high volume fraction of air. As reported for MWCNT/polycaprolactone systems[130], reflectivity of foams containing low CNT volume fractions could be efficiently decreased in comparison to solid composites having similar electrical conductivities. Foams presented lower dielectric constants and thus a lower reflection at the input interface (Figure 1.5). Furthermore, the proper dispersion of CNTs provided materials with conductivities high enough to attenuate the incident EM waves by conductive dissipation (SE>80 dB) even at low loadings (<1 vol%).In addition to limited reflectivity, the enhancement of SE_A in these structures has been frequently attributed to favored re-reflection and subsequent dissipation of the absorbed portion of the wave within the pores of the material[131]. These findings suggest that porous structures of CNTs and graphene could be promising candidates for the development of lightweight carbon-based EMI absorbers.

Foamed materials are commonly used in anechoic chambers[133–135], where an entire space is covered with EM absorbers to create a non-reflecting environment. For this application, foamed absorbers are produced with pyramidal patterns (and also other tapered geometries) in which reflection is limited further due to the graded surface impedance (Figure 1.6a). The latter is also a key concept for the design of panels with ranked impedance layers. In these shields, multiple layers with gradual increment of permittivity are stuck to form a broader interface that boosts the wave propagation within the structure. When the wave reaches the most active layer (the one with the higher permittivity /conductivity), the probability of reflections escaping out form the

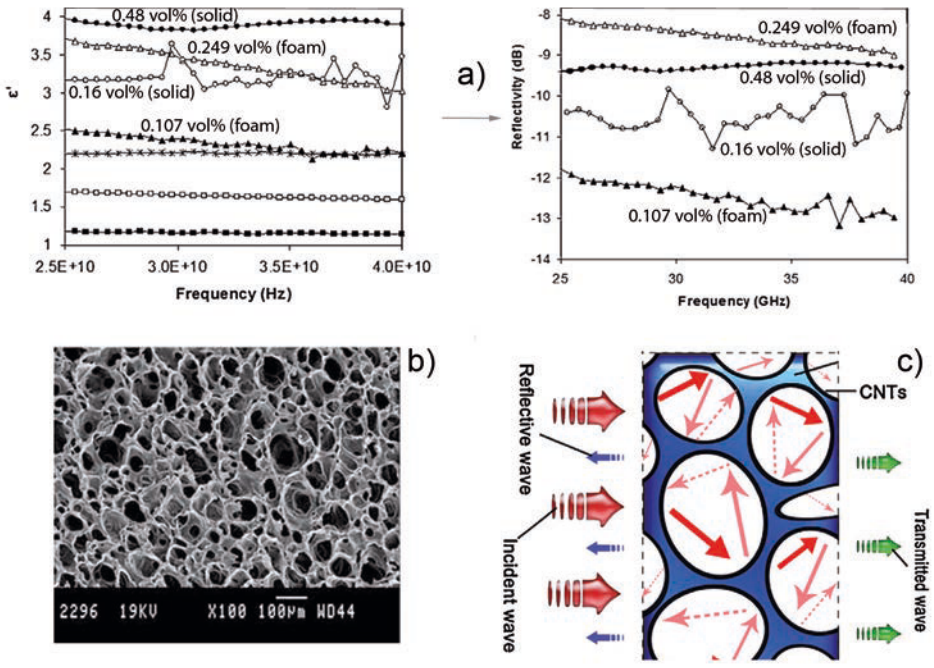

FIGURE 1.5: a) Dielectric constant (ϵ', left) of CNT foamed and solid composites, showing how the ϵ' magnitude decreases for foamed samples and how the reflectivity (right) can be limited, in consistency with ϵ', when highly conductive foamed samples are compared with solid ones having lower conductivities[130]; b) SEM image of these CNT-foams[130]. c) Proposed attenuation mechanism of the incident wave through multiple reflections within the pores of conductive foams[132]

multilayered structure is very low. Therefore, this configuration limits reflection and enhances absorption.

Other multilayered shields are those that follow the concept of Sallisbury and Jauman[137] screens (Figure 1.6b). Here the multilayer is formed with various layers of the same shield separated by a dielectric. The SE improvement is achieved by favoring multiple reflections between and within consecutive active shielding layers. Although multiple reflections positively contribute to net reflection, in this case the apparent absorption dominates and SE by absorption is enhanced.

Some approaches that exploit these concepts in composites of CNTs and graphene

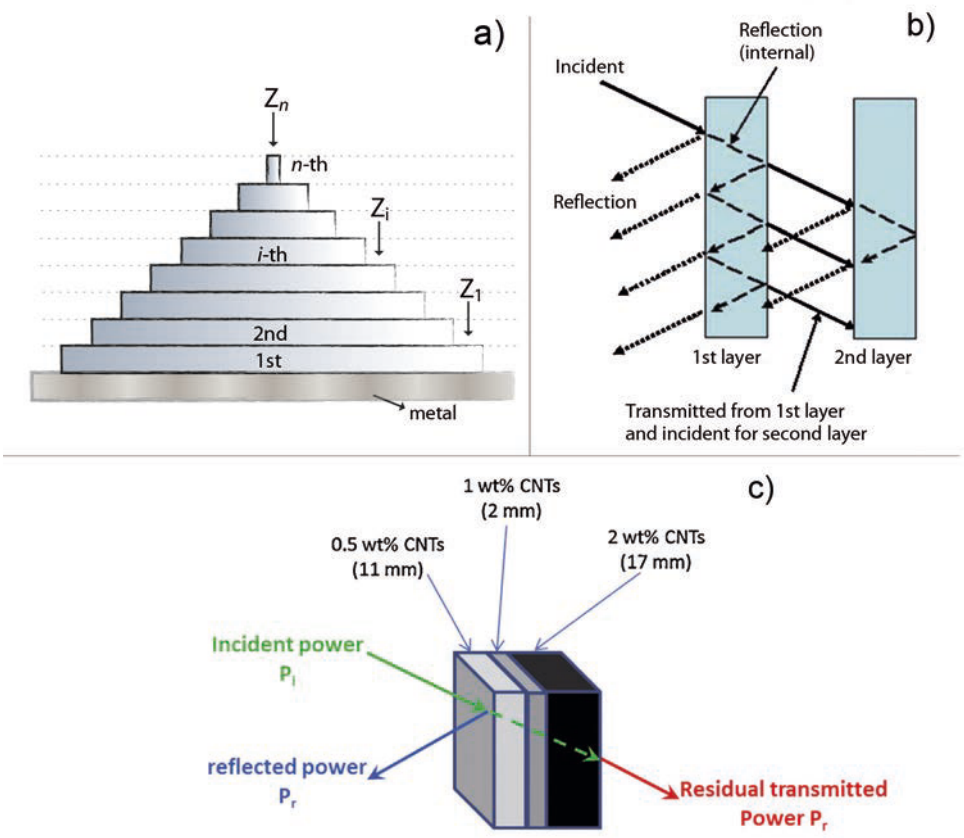

FIGURE 1.6: a) Schematic transmission line approximation of tapered-impedance pyramidal absorbers[136]. b) Resonant-like behavior of Jauman and Sallisbury screens[32] c) Panels with ranked impedance layers of foamed CNT-polymer composites designed to minimize the front-face reflection of the most conductive composite layer[32]

include: extremely broadband (8-40 GHz) CNT/polycarbonate flexible multilayered shields[138]; graphene/paraffin sandwich structures[99] with shielding efficiencies up to 27 dB; or ultrathin shields made from graphene paper/paraffin/ethylene-vinyl-acetate layers, showing shielding capabilities of up to 47.7 dB. Furthermore, Multilayered CNT composites have been also foamed to obtain more lightweight and efficient EMI absorbers. For example, the total reflection of polycaprolactone foams assembled into a three-layer structure with 0.5, 1 and 2 wt% of CNTs, was decreased to *ca.* 5 dB

in comparison to the reflection that the 1 wt% CNT monolayer presented by itself (Figure 1.6c).

Lastly, strategies that attribute a better impedance matching due to an added term of magnetic permeability to composites with nanocarbons include: CNTs filled with Fe-Ni [139], Fe-Co or Fe-Ni-Co nanowires [140]; CNTs filled with Ni [141] or Fe nanoparticles and composited with ferrite microrods [142]; decoration of CNFs, CNTs and chemically derived graphene with Magnetite [143–145], Co, Ni-Fe [146] and $CoFe_2O_4$ [147] ferrite nanoparticles; CNTs mixed with $Fe/Co/Ni$ nanopowders [148]; CNF fibers mixed with iron carbonyl particles, or the effect that is seen in unpurified CNTs with small contents of residual Fe left from the catalyzer [36]. Although there are reports that reflection values can be lowered by the presence of the small magnetic particles it is still debated whether this reduction in reflection can be truly attributed to the effect of the magnetic constituent [31].

Bibliography

[1] B. E. Keiser. *Principles of electromagnetic compatibility.* Artech House Microwave Library, 1979.

[2] C. R. Paul. *Introduction to electromagnetic compatibility.* John Wiley & Sons, Inc., 2006.

[3] D. D. L. Chung. Electromagnetic interference shielding effectiveness of carbon materials. *Carbon*, 39(2),279–285, 2001.

[4] A. Perrin and M. Souques. *Electromagnetic Fields, Environment and Health.* Springer, 2013.

[5] C. Tong. Advced materials and design for board level EMI shielding · Principle of board level shielding (BLS), 2012.

[6] A. N. Yusoff, M. H. Abdullah, S. H. Ahmad, S. F. Jusoh, A. A. Mansor, S. A. A. Hamid, and I. Introduction. Electromagnetic and absorption properties of some microwave absorbers. *J. Appl. Phys.*, 92(2),876, 2002.

[7] A. N. Lagarkov and K. N. Rozanov. High-frequency behavior of magnetic composites. *J. Magn. Magn. Mater.*, 321(14),2082–2092, 2009.

[8] K. Sakai, N. Asano, Y. Wada, and S. Yoshikado. Composite electromagnetic wave absorber made of soft magnetic material and polystyrene resin and control of permeability and permittivity. *J. Eur. Ceram. Soc.*, 30(2),347–353, 2010.

[9] T. Kasagi, T. Tsutaoka, and K. Hatakeyama. Particle size effect on the complex permeability for permalloy composite materials. *IEEE Trans. Magn.*, 35(5),3424–3426, 1999.

[10] V. B. Bregar. Advantages of Ferromagnetic Nanoparticle Composites in Microwave Absorbers. *IEEE Trans. Magn.*, 40(3),1679–1684, 2004.

[11] M. S. Kim, H. K. Kim, S. W. Byun, S. H. Jeong, Y. K. Hong, J. S. Joo, K. T. Song, J. K. Kim, C. J. Lee, and J. Y. Lee. PET fabric/polypyrrole composite with high electrical conductivity for EMI shielding. *Synth. Met.*, 126(2-3),233–239, 2002.

[12] N. F. Colaneri and L. W. Schacklette. EMI shielding measurements of conductive polymer blends. *IEEE Trans. Instrum. Meas.*, 41(2),291–297, 1992.

[13] K. Lakshmi, H. John, K. T. Mathew, R. Joseph, and K. E. George. Microwave absorption, reflection and EMI shielding of PU-PANI composite. *Acta Mater.*, 57(2),371–375, 2009.

[14] S. K. Dhawan, N. Singh, and D. Rodrigues. Electromagnetic shielding behaviour of conducting polyaniline composites. *Sci. Technol. Adv. Mater.*, 4(2),105–113, 2003.

[15] Y. Haba, E. Segal, M. Narkis, G. Titelman, and A. Siegmann. Polyaniline-DBSA/polymer blends prepared via aqueous dispersions. *Synth. Met.*, 110(3),189–193, 2000.

[16] L. Li and D. D. L. Chung. Effect of viscosity on the electrical properties of conducting thermoplastic composites made by compression molding of a powder mixture. *Polym. Compos.*, 14(6),467–472, 1993.

[17] L. Li and D. D. L. Chung. Electrically conducting powder filled polyimidesiloxane. *Compos.*, 22(3),211–218, 1991.

[18] L. Li and D. D. L. Chung. Electrical and mechanical properties of electrically conductive polyethersulfone composites. *Compos.*, 25(3),215–224, 1994.

[19] N. Morgan. Corrosion inhibiting EMI/RFI shielding coating and method of its use, EP Patent App. EP19,900,314,408, July 24 1991. EP Patent App. EP19,900,314,408.

[20] S. T. Tan, M.-q. Zhang, M. Z. Rong, and H. M. Zeng. Effect of interfacial modification on metal fiber filled polypropylene composites and property balance. *Polym. Compos.*, 20(3),406–412, 1999.

[21] L. Nan I and R. van der Meer. Synergistic effect of metal flake and metal or metal coated fiber on EMI shielding effectiveness of thermoplastics, 1986.

[22] S. Shinagawa, Y. Kumagai, and K. Urabe. Conductive Papers Containing Metallized Polyester Fibers for Electromagnetic Interference Shielding. *J. Porous Mater.*, 6(3),185–190, 1999.

[23] S.-S. Tzeng and F.-Y. Chang. EMI shielding effectiveness of metal-coated carbon fiber-reinforced ABS composites. *Mater. Sci. Eng., A*, 302(2),258–267, 2001.

[24] M. H. Al-Saleh, G. A. Gelves, and U. Sundararaj. Copper nanowire/polystyrene nanocomposites: Lower percolation threshold and higher EMI shielding. *Compos. Part A*, 42(1),92–97, 2011.

[25] G. A. Gelves, M. H. Al-Saleh, and U. Sundararaj. Highly electrically conductive and high performance EMI shielding nanowire/polymer nanocomposites by miscible mixing and precipitation. *J. Mater. Chem.*, 21(3),829, 2011.

[26] M. Hu, J. Gao, Y. Dong, K. Li, G. Shan, S. Yang, and R. K.-Y. Li. Flexible transparent PES/silver nanowires/PET sandwich-structured film for high-efficiency electromagnetic interference shielding. *Langmuir*, 28(18),7101–7106, 2012.

[27] J.-C. Huang. EMI shielding plastics: A review. *Adv. Polym. Technol.*, 14(2),137–150, 1995.

[28] N. Das, D. Khastgir, T. Chaki, and A. Chakraborty. Electromagnetic interference shielding effectiveness of carbon black and carbon fibre filled EVA and NR based composites. *Compos. Part A*, 31(10),1069–1081, 2000.

[29] L. Vovchenko, Y. Perets, I. Ovsienko, L. Matzui, V. Oliynyk, and V. Launetz. Shielding coatings based on carbon-polymer composites. *Surf. Coat. Technol.*, 211,196–199, 2012.

[30] F. Ren, H. Yu, L. Wang, M. Saleem, Z. Tian, and P. Ren. Current progress on the modification of carbon nanotubes and their application in electromagnetic wave absorption. *RSC Adv.*, 4(28),14419–14431, 2014.

[31] F. Qin and C. Brosseau. A review and analysis of microwave absorption in polymer composites filled with carbonaceous particles. *J. Appl. Phys.*, 111(6),061301, 2012.

[32] J.-M. Thomassin, C. Jérôme, T. Pardoen, C. Bailly, C. Je, I. Huynen, and C. Detrembleur. Polymer/carbon based composites as electromagnetic interference (EMI) shielding materials. *Mater. Sci. Eng., R*, 74(7),211–232, 2013.

[33] M. H. Al-Saleh and U. Sundararaj. A review of vapor grown carbon nanofiber/polymer conductive composites. *Carbon*, 47(1),2–22, 2009.

[34] Z. Wang, L. Wu, J. Zhou, W. Cai, B. Shen, and Z. Jiang. Magnetite Nanocrystals on Multiwalled Carbon Nanotubes as a Synergistic Microwave Absorber. *J. Phys. Chem. C*, 117(10),5446–5452, 2013.

[35] M. Crespo, M. González, A. L. Elías, L. Pulickal Rajukumar, J. Baselga, M. Terrones, and J. Pozuelo. Ultra-light carbon nanotube sponge as an efficient electromagnetic shielding material in the ghz range. *Phys. Status Solidi RRL*, 8(8),698–704, 2014.

[36] R. C. Che, L. M. Peng, X. F. Duan, Q. Chen, and X. L. Liang. Microwave Absorption Enhancement and Complex Permittivity and Permeability of Fe Encapsulated within Carbon Nanotubes. *Adv. Mater.*, 16(5),401–405, 2004.

[37] P. F. Guan, X. F. Zhang, and J. J. Guo. Assembled Fe_3O_4 nanoparticles on graphene for enhanced electromagnetic wave losses. *Appl. Phys. Lett.*, 101(15),153108, 2012.

[38] H. M. Kim, K. Kim, C. Y. Lee, J. Joo, S. J. Cho, H. S. Yoon, D. A. Pejaković, J. W. Yoo, and A. J. Epstein. Electrical conductivity and electromagnetic interference shielding of multiwalled carbon nanotube composites containing Fe catalyst. *Appl. Phys. Lett.*, 84(4),589–591, 2004.

[39] P. Penwisa, M. Rathanawan, and C. J. Sadhan. Electrically conductive compounds of polycarbonate, liquid crystalline polymer, and multiwalled carbon nanotubes. *J.Nano Mat.*, 2012,1–10, 2012.

[40] D.-X. Yan, H. Pang, L. Xu, Y. Bao, P.-G. Ren, J. Lei, and Z.-M. Li. Electromagnetic interference shielding of segregated polymer composite with an ultralow loading of in situ thermally reduced graphene oxide. *Nanotechnol.*, 25(14),145705, 2014.

[41] M. H. Al-Saleh and U. Sundararaj. Electromagnetic interference shielding mechanisms of CNT/polymer composites. *Carbon*, 47(7),1738–1746, 2009.

[42] K. L. Keiser. *Electromagnetic Shielding.* Taylor & Francis Group, 2006.

[43] M. H. Al-Saleh, W. H. Saadeh, and U. Sundararaj. EMI shielding effectiveness of carbon based nanostructured polymeric materials: A comparative study. *Carbon*, 60(2),146–156, 2013.

[44] M. H. Al-Saleh and U. Sundararaj. X-band EMI shielding mechanisms and shielding effectiveness of high structure carbon black/polypropylene composites. *J. Phys. D: Appl. Phys.*, 46(3),035304, 2013.

[45] M. Mahmoodi, M. Arjmand, U. Sundararaj, and S. Park. The electrical conductivity and electromagnetic interference shielding of injection molded multi-walled carbon nanotube/polystyrene composites. *Carbon*, 50(4),1455–1464, 2012.

[46] C. Bishop. The Relationship Between Loss, Conductivity, and Dielectric Constant , 2001.

[47] V. G. Harris, A. Geiler, Y. Chen, S. D. Yoon, M. Wu, A. Yang, Z. Chen, P. He, P. V. Parimi, X. Zuo, C. E. Patton, M. Abe, O. Acher, and C. Vittoria. Recent advances in processing and applications of microwave ferrites. *J. Magn. Magn. Mater.*, 321(14),2035–2047, 2009.

[48] L. Zhang and Z. Y. Cheng. Development of polymer based 0-3 composites with high dielectric constant. *J. Adv. Dielectr.*, 1(4),389–406, 2011.

[49] A. N. N. Lagarkov, A. K. Sarychev, Y. R. R. Smychkovich, and A. P. P. Vinogradov. Effective Medium Theory For Microwave Dielectric Constant and Magnetic Permeability of Conducting Stick Composites. *J. Electromagnet. Wave.*, 6(9),1159–1176, 1992.

[50] A. Pakhomov, S. Wong, X. Yan, and X. Zhang. Low-frequency divergence of the dielectric constant in metal-insulator nanocomposites with tunneling. *Phys. Rev. B: Condens. Matter Mater. Phys.*, 58(20),R13375–R13378, 1998.

[51] W. Liu, W. Zhong, H. Y. Jiang, N. J. Tang, X. L. Wu, and W. Y. Du. Synthesis and magnetic properties of $FeNi_3/Al_2O_3$ core-shell nanocomposites. *Eur. Phys. J. B*, 46(4),471–474, 2005.

[52] N. R. Center. Depth of Penetration & Current Density.

[53] C. University. The Skin Effect-Chapter 20 .

[54] X. F. Zhang, P. F. Guan, and X. L. Dong. Transform between the permeability and permittivity in the close-packed Ni nanoparticles. *Appl. Phys. Lett.*, 97(3),033107, 2010.

[55] D. L. Leslie-Pelecky and R. D. Rieke. Magnetic Properties of Nanostruct. Mater. *Chem. Mater.*, 8(8),1770–1783, 1996.

[56] R. H. Kodama. Magnetic nanoparticles. *J. Magn. Magn. Mater.*, 200(1–3),359–372, 1999.

[57] R. Dosoudil, M. Usakova, J. Franek, J. Slama, A. Gruskova, J. Sláma, and A. Grusková. Particle Size and Concentration Effect on Permeability and EM-Wave Absorption Properties of Hybrid Ferrite Polym. Compos. *IEEE Trans. Magn.*, 46(2),436–439, 2010.

[58] A. H. Habib, S. Xu, E. Walker, M. Ondeck, R. Swaminathan, and M. E. McHenry. The role of eddy currents and nanoparticle size on AC magnetic field-induced reflow in solder/magnetic nanocomposites. *J. Appl. Phys.*, 111(7),07B305, 2012.

[59] X. F. Zhang, X. L. Dong, H. Huang, Y. Y. Liu, W. N. Wang, X. G. Zhu, B. Lv, J. P. Lei, and C. G. Lee. Microwave absorption properties of the carbon-coated nickel nanocapsules. *Appl. Phys. Lett.*, 89(5),053115–053118, 2006.

[60] X. G. Liu, B. Li, D. Y. Geng, W. B. Cui, F. Yang, Z. G. Xie, D. J. Kang, and Z. D. Zhang. $(Fe, Ni)/C$ nanocapsules for electromagnetic-wave-absorber in the whole Ku-band. *Carbon*, 47(2),470–474, 2009.

[61] D. Hasegawa, H. Yang, T. Ogawa, and M. Takahashi. Challenge of ultra high frequency limit of permeability for magnetic nanoparticle assembly with organic polymer—Application of superparamagnetism. *J. Magn. Magn. Mater.*, 321(7),746–749, 2009.

[62] N.-N. Song, H.-T. Yang, H.-L. Liu, X. Ren, H.-F. Ding, X.-Q. Zhang, and Z.-H. Cheng. Exceeding natural resonance frequency limit of monodisperse F_3O_4 nanoparticles via superparamagnetic relaxation. *Sci. Rep.*, 3,3161, 2013.

[63] H. Kura, K. Hata, T. Oikawa, M. Takahashi, and T. Ogawa. Effect of induced uniaxial magnetic anisotropy on ferromagnetic resonance frequency of $Fe--Co$ alloy nanoparticle/polystyrene nanocomposite. *Scr. Mater.*, 76,65–68, 2014.

[64] N.-N. Song, Y.-J. Ke, H.-T. Yang, H. Zhang, X.-Q. Zhang, B.-G. Shen, and Z.-H. Cheng. Integrating giant microwave absorption with magnetic refrigeration in one multifunctional intermetallic compound of LaFe(11.6)Si(1.4)C(0.2)H(1.7). *Sci. Rep.*, 3,2291, 2013.

[65] A.-H. Lu, E. L. Salabas, and F. Schüth. Magnetic nanoparticles: synthesis, protection, functionalization, and application. *Angew. Chem. Int. Ed.*, 46(8),1222–1244, 2007.

[66] Q. He, T. Yuan, X. Zhang, Z. Luo, N. Haldolaarachchige, L. Sun, D. P. Young, S. Wei, and Z. Guo. Magnetically Soft and Hard Polypropylene/Cobalt Nanocomposites: Role of Maleic Anhydride Grafted Polypropylene. *Macromol.*, 46(6),2357–2368, 2013.

[67] Q. He, T. Yuan, Z. Luo, N. Haldolaarachchige, D. P. Young, S. Wei, and Z. Guo. Morphology and phase controlled cobalt nanostructures in magnetic polypropylene nanocomposites: the role of alkyl chain-length in maleic anhydride grafted polypropylene. *Chem. Commun.*, 49(26),2679–2681, 2013.

[68] M. P. Pileni. Reverse micelles as microreactors. *J. Phys. Chem.*, 97(27),6961–6973, 1993.

[69] Z. Yue, J. Zhou, L. Li, H. Zhang, and Z. Gui. Synthesis of nanocrystalline $NiCuZn$ ferrite powders by sol-gel auto-combustion method. *J. Magn. Magn. Mater.*, 208(1–2),55–60, 2000.

[70] A. H. Lu and F. Schüth. Nanocasting: A Versatile Strategy for Creating Nanostructured Porous Materials. *Adv. Mater.*, 18(14),1793–1805, 2006.

[71] L. L. Hench and J. K. West. The sol-gel process. *Chem. Rev.*, 90(1),33–72, 1990.

[72] L. García-Cerda. Magnetic nanocomposites: preparation and characterization of Co-ferrite nanoparticles in a silica matrix. *J. Alloy. Compd.*, 369(1-2),148–151, 2004.

[73] A. B. Fuertes. A general and low-cost synthetic route to high-surface area metal oxides through a silica xerogel template. *J. Phys. Chem. Solids*, 66(5),741–747, 2005.

[74] M. Stoia, C. Caizer, M. Ştefănescu, P. Barvinschi, and L. Barbu-Tudoran. Characterisation of nickel-zinc ferrite/silica nanocomposites with low ferrite concentration obtained by an improved modified sol-gel method. *J. Sol-Gel Sci. Technol.*, 58(1),126–134, 2010.

[75] T. Valdés-Solís, P. Tartaj, G. Marbán, and A. B. Fuertes. Facile synthetic route to nanosized ferrites by using mesoporous silica as a hard template. *Nanotechnol.*, 18(14),145603, 2007.

[76] Z. Guo, K. Lei, Y. Li, H. W. Ng, S. Prikhodko, and H. T. Hahn. Fabrication and characterization of iron oxide nanoparticles reinforced vinyl-ester resin nanocomposites. *Compos. Sci. Technol.*, 68(6),1513–1520, 2008.

[77] X. Zhang, O. Alloul, J. Zhu, Q. He, Z. Luo, H. A. Colorado, N. Haldolaarachchige, D. P. Young, T. D. Shen, S. Wei, and Z. Guo. Iron-core carbon-shell nanoparticles reinforced electrically conductive magnetic epoxy resin nanocomposites with reduced flammability. *RSC Adv.*, 3(24),9453–9464, 2013.

[78] H. Gu, S. Tadakamalla, Y. Huang, H. A. Colorado, Z. Luo, N. Haldolaarachchige, D. P. Young, S. Wei, and Z. Guo. Polyaniline stabilized magnetite nanoparticle reinforced epoxy nanocomposites. *ACS Appl. Mater. Interfaces*, 4(10),5613–5624, 2012.

[79] J. Zhu, S. Wei, J. Ryu, L. Sun, Z. Luo, and Z. Guo. Magnetic Epoxy Resin Nanocomposites Reinforced with Core-Shell Structured Fe@FeO Nanoparticles: Fabrication and Property Analysis. *ACS Appl. Mater. Interfaces*, 2(7),2100–2107, 2010.

[80] L. A. Ramajo, A. A. Cristóbal, P. M. Botta, J. M. Porto López, M. M. Reboredo, and M. S. Castro. Dielectric and magnetic response of Fe_3O_4/epoxy composites. *Compos. Part A*, 40(4),388–393, 2009.

[81] B. Hallouet, B. Wetzel, and R. Pelster. On the Dielectric and Magnetic Properties of Nanocomposites. *J. Nano Mat.*, 2007(1),1–11, 2007.

[82] G. Kortaberria, P. Arruti, A. Jimeno, I. Mondragon, and M. Sangermano. Local dynamics in epoxy coatings containing iron oxide nanoparticles by dielectric relaxation spectroscopy. *J. Appl. Polym. Sci.*, 109(5),3224–3229, 2008.

[83] M. González, I. Martín-Fabiani, J. Baselga, and J. Pozuelo. Magnetic nanocomposites based on hydrogenated epoxy resin. *Mater. Chem. Phys.*, 132(2-3),618–624, 2012.

[84] J. Zhu, S. Wei, I. Y. Lee, S. Park, J. Willis, N. Haldolaarachchige, D. P. Young, Z. Luo, and Z. Guo. Silica stabilized iron particles toward anti-corrosion magnetic polyurethane nanocomposites. *RSC Adv.*, 2(3),1136–1143, 2012.

[85] M. Chen, H. Qu, J. Zhu, Z. Luo, A. Khasanov, A. S. Kucknoor, N. Haldolaarachchige, D. P. Young, S. Wei, and Z. Guo. Magnetic electrospun fluorescent polyvinylpyrrolidone nanocomposite fibers. *Polym.*, 53(20),4501–4511, 2012.

[86] X. Guo, Y. Deng, D. Gu, R. Che, and D. Zhao. Synthesis and microwave absorption of uniform hematite nanoparticles and their core-shell mesoporous silica nanocomposites. *J. Mater. Chem.*, 19(37),6706–6712, 2009.

[87] J. Zhu, S. Wei, N. Haldolaarachchige, D. P. Young, and Z. Guo. Electromagnetic Field Shielding Polyurethane Nanocomposites Reinforced with Core-Shell Fe-Silica Nanoparticles. *J. Phys. Chem. C*, 115(31),15304–15310, 2011.

[88] J. Liu, R. Che, H. Chen, F. Zhang, F. Xia, Q. Wu, and M. Wang. Microwave absorption enhancement of multifunctional composite microspheres with spinel Fe_3O_4 Cores and Anatase TiO_2 shells. *Small*, 8(8),1214–1221, 2012.

[89] L. Yan, J. Wang, X. Han, Y. Ren, Q. Liu, and F. Li. Enhanced microwave absorption of Fe nanoflakes after coating with SiO_2 nanoshell. *Nanotechnol.*, 21(9),095708, 2010.

[90] X. G. Liu, D. Y. Geng, H. Meng, P. J. Shang, and Z. D. Zhang. Microwave-absorption properties of ZnO-coated iron nanocapsules. *Appl. Phys. Lett.*, 92(17),173117, 2008.

[91] X. F. Zhang, P. F. Guan, and X. L. Dong. Multidielectric polarizations in the core/shell Co/graphite nanoparticles. *Appl. Phys. Lett.*, 96(22),223111–223114, 2010.

[92] M. Crespo, M. González, and J. Pozuelo. Magnetic silica:epoxy composites with a nano- and micro-scale control. *Mater. Chem. Phys.*, 144(3),335–342, 2014.

[93] I. Park, H.-g. Peng, D. W. Gidley, S. Xue, and T. J. Pinnavaia. Epoxy-Silica Mesocomposites with Enhanced Tensile Properties and Oxygen Permeability. *Chem. Mater.*, 18(3),650–656, 2006.

[94] M. A. B. Meador, E. F. Fabrizio, F. Ilhan, A. Dass, G. Zhang, P. Vassilaras, J. C. Johnston, and N. Leventis. Cross-linking Amine-Modified Silica Aerogels with Epoxies: Mechanically Strong Lightweight Porous Materials. *Chem. Mater.*, 17(5),1085–1098, 2005.

[95] B. J.-P. Adohi, A. Mdarhri, C. Prunier, B. Haidar, and C. Brosseau. A comparison between physical properties of carbon black-polymer and carbon nanotubes-polymer composites. *J. Appl. Phys.*, 108(7),074108, 2010.

[96] C. Brosseau, W. NDong, and A. Mdarhri. Influence of uniaxial tension on the microwave absorption properties of filled polymers. *J. Appl. Phys.*, 104(7),074907, 2008.

[97] Y. Huang, N. Li, Y. Ma, F. Du, F. Li, X. He, X. Lin, H. Gao, and Y. Chen. The influence of single-walled carbon nanotube structure on the electromagnetic interference shielding efficiency of its epoxy composites. *Carbon*, 45(8),1614–1621, 2007.

[98] X. Bai, Y. Zhai, and Y. Zhang. Green Approach To Prepare Graphene-Based Composites with High Microwave Absorption Capacity. *J. Phys. Chem. C*, 115(23),11673–11677, 2011.

[99] W.-L. Song, M.-S. Cao, M.-M. Lu, S. Bi, C.-Y. Wang, J. Liu, J. Yuan, and L.-Z. Fan. Flexible graphene/polymer composite films in sandwich structures for effective electromagnetic interference shielding. *Carbon*, 66,67–76, 2014.

[100] J. Liang, Y. Wang, Y. Huang, Y. Ma, Z. Liu, J. Cai, C. Zhang, H. Gao, and Y. Chen. Electromagnetic interference shielding of graphene/epoxy composites. *Carbon*, 47(3),922–925, 2009.

[101] C. Wang, X. Han, P. Xu, X. Zhang, Y. Du, S. Hu, J. Wang, and X. Wang. The electromagnetic property of chemically reduced graphene oxide and its application as microwave absorbing material. *Appl. Phys. Lett.*, 98(7),072906, 2011.

[102] S. K. Hong, K. Y. Kim, T. Y. Kim, J. H. Kim, S. W. Park, J. H. Kim, and B. J. Cho. Electromagnetic interference shielding effectiveness of monolayer graphene. *Nanotechnol.*, 23(45),455704, 2012.

[103] N. C. Das, Y. Liu, K. Yang, W. Peng, S. Maiti, and H. Wang. Single-walled carbon nanotube/poly(methyl methacrylate) composites for electromagnetic interference shielding. *Polym. Eng. Sci.*, 49(8),1627–1634, 2009.

[104] Z. Liu, G. Bai, Y. Huang, Y. Ma, F. Du, F. Li, T. Guo, and Y. Chen. Reflection and absorption contributions to the electromagnetic interference shielding of single-walled carbon nanotube/polyurethane composites. *Carbon*, 45(4),821–827, 2007.

[105] N. Li, Y. Huang, F. Du, X. He, X. Lin, H. Gao, Y. Ma, F. Li, Y. Chen, and P. C. Eklund. Electromagnetic interference (EMI) shielding of single-walled carbon nanotube epoxy composites. *Nano Lett.*, 6(6),1141–1145, 2006.

[106] M. Arjmand, T. Apperley, M. Okoniewski, and U. Sundararaj. Comparative study of electromagnetic interference shielding properties of injection molded versus compression molded multi-walled carbon nanotube/polystyrene composites. *Carbon*, 50(14),5126–5134, 2012.

[107] X. Xie, Y. Mai, and X. Zhou. Dispersion and alignment of carbon nanotubes in polymer matrix: A review. *Mater. Sci. Eng., R*, 49(4),89–112, 2005.

[108] L. Liu, S. Matitsine, Y. B. Gan, L. F. Chen, L. B. Kong, and K. N. Rozanov. Frequency dependence of effective permittivity of carbon nanotube composites. *J. Appl. Phys.*, 101(9),094106, 2007.

[109] Z. Xu and C. Gao. In situ Polymerization Approach to Graphene-Reinforced Nylon-6 Composites. *Macromol.*, 43(16),6716–6723, 2010.

[110] K. Balasubramanian and M. Burghard. Chemically functionalized carbon nanotubes. *Small*, 1(2),180–192, 2005.

[111] L. Vaisman, H. D. Wagner, and G. Marom. The role of surfactants in dispersion of carbon nanotubes. *Adv. Colloid Interface Sci.*, 128-130,37–46, 2006.

[112] S. Maiti, S. Suin, N. K. Shrivastava, and B. B. Khatua. A strategy to achieve high electromagnetic interference shielding and ultra low percolation in multi-wall carbon nanotube-polycarbonate composites through selective localization of carbon nanotubes. *RSC Adv.*, 4(16),7979–7990, 2014.

[113] M. Sumita, K. Sakata, Y. Hayakawa, S. Asai, K. Miyasaka, and M. Tanemura. Double percolation effect on the electrical conductivity of conductive particles filled polymer blends. *Colloid Polym. Sci.*, 270(2),134–139, 1992.

[114] J.-M. Thomassin, I. Molenberg, I. Huynen, A. Debuigne, M. Alexandre, C. Jérôme, and C. Detrembleur. Locating carbon nanotubes (CNTs) at the surface of polymer microspheres using poly(vinyl alcohol) grafted CNTs as dispersion co-stabilizers. *Chem. Comm.*, 46(19),3330–3332, 2010.

[115] Y. Yang, M. C. Gupta, K. L. Dudley, and R. W. Lawrence. Novel carbon nanotube-polystyrene foam composites for electromagnetic interference shielding. *Nano Lett.*, 5(11),2131–2134, 2005.

[116] A. Abarrategi, M. C. Gutiérrez, C. Moreno-Vicente, M. J. Hortigüela, V. Ramos, J. L. López-Lacomba, M. L. Ferrer, and F. del Monte. Multiwall carbon nanotube scaffolds for tissue engineering purposes. *Biomater.*, 29(1),94–102, 2008.

[117] J. Zou, J. Liu, A. S. Karakoti, A. Kumar, D. Joung, Q. Li, S. I. Khondaker, S. Seal, and L. Zhai. Ultralight multiwalled carbon nanotube aerogel. *ACS Nano*, 4(12),7293–302, 2010.

[118] F. Irin, S. Das, F. O. Atore, and M. J. Green. Ultralow percolation threshold in aerogel and cryogel templated composites. *Langmuir*, 29(36),11449–11456, 2013.

[119] S. Nardecchia, D. Carriazo, M. L. Ferrer, M. C. Gutiérrez, and F. del Monte. Three dimensional macroporous architectures and aerogels built of carbon nanotubes and/or graphene: synthesis and applications. *Chem. Soc. Rev.*, 42(2),794–830, 2013.

[120] H.-B. Zhang, Q. Yan, W.-G. Zheng, Z. He, and Z.-Z. Yu. Tough graphene-polymer microcellular foams for electromagnetic interference shielding. *ACS Appl. Mater. Interfaces*, 3(3),918–924, 2011.

[121] Y. Li, Y. A. Samad, K. Polychronopoulou, S. M. Alhassan, and K. Liao. Highly Electrically Conductive Nanocomposites Based on PolymerInfused Graphene Sponges. *Sci. Rep.*, 4,1–6, 2014.

[122] K. Koziol, J. Vilatela, A. Moisala, M. Motta, P. Cunniff, M. Sennett, and A. Windle. High-performance carbon nanotube fiber. *Sci.*, 318(5858),1892–1895, 2007.

[123] X. Gui, J. Wei, K. Wang, A. Cao, H. Zhu, Y. Jia, Q. Shu, and D. Wu. Carbon nanotube sponges. *Adv. Mater.*, 22(5),617–621, 2010.

[124] C. Shan, W. Zhao, X. L. Lu, D. J. O'Brien, Y. Li, Z. Cao, A. L. Elias, R. Cruz-Silva, M. Terrones, B. Wei, and J. Suhr. Three-dimensional nitrogen-doped multiwall carbon nanotube sponges with tunable properties. *Nano Lett.*, 13(11),5514–5520, 2013.

[125] Z. Chen, C. Xu, C. Ma, W. Ren, and H.-M. Cheng. Lightweight and flexible graphene foam composites for high-performance electromagnetic interference shielding. *Adv. Mater.*, 25(9),1296–300, 2013.

[126] X. Gui, H. Li, L. Zhang, Y. Jia, L. Liu, Z. Li, J. Wei, K. Wang, H. Zhu, Z. Tang, D. Wu, and A. Cao. A facile route to isotropic conductive nanocomposites by direct polymer infiltration of carbon nanotube sponges. *ACS Nano*, 5(6),4276–4283, 2011.

[127] D. P. Hashim, N. T. Narayanan, J. M. Romo-Herrera, D. A. Cullen, M. G. Hahm, P. Lezzi, J. R. Suttle, D. Kelkhoff, E. Muñoz-Sandoval, S. Ganguli, A. K. Roy, D. J. Smith, R. Vajtai, B. G. Sumpter, V. Meunier, H. Terrones, M. Terrones, and P. M. Ajayan. Covalently bonded three-dimensional carbon nanotube solids via boron induced nanojunctions. *Sci. Rep.*, 2(363),1–8, 2012.

[128] H. Qian, E. S. Greenhalgh, M. S. P. Shaffer, and A. Bismarck. Carbon nanotube-based hierarchical composites: a review. *J. Mater. Chem.*, 20(23),4751–4762, 2010.

[129] L. Liu, W. Ma, and Z. Zhang. Macroscopic carbon nanotube assemblies: preparation, properties, and potential applications. *Small*, 7(11),1504–1520, 2011.

[130] J.-M. Thomassin, C. Pagnoulle, L. Bednarz, I. Huynen, R. Jerome, and C. Detrembleur. Foams of polycaprolactone/MWNT nanocomposites for efficient EMI reduction. *J. Mater. Chem.*, 18(7),792–796, 2008.

[131] B. Shen, W. Zhai, M. Tao, J. Ling, and W. Zheng. Lightweight, multifunctional polyetherimide/graphene@Fe_3O_4 composite foams for shielding of electromagnetic pollution. *ACS Appl. Mater. Interfaces*, 5(21),11383–11391, 2013.

[132] K. Ji, H. Zhao, J. Zhang, J. Chen, and Z. Dai. Fabrication and electromagnetic interference shielding performance of open-cell foam of a $Cu-Ni$ alloy integrated with CNTs. *Appl. Surf. Sci.*, 311,351–356, 2014.

[133] EMC. Anechoic Materials — Absorbers and Shielding for Anechoic and EMC Chambers, http://www.mvg-emc.com/content/anechoic-materials.

[134] D. Weston. *Electromagnetic Compatibility: Principles and Applications, Second Edition, Revised and Expanded.* Marcel Dekker, Inc., 2001.

[135] HollandShielding. EMI Filters and RF Shielding Products, http://hollandshielding.com.

[136] M.-J. Park, J. Choi, and S.-S. Kim. Wide bandwidth pyramidal absorbers of granular ferrite and carbonyl iron powders. *IEEE T. Magn.*, 36(5),3272–3274, 2000.

[137] X. C. Tong. *Advanced materials and design for electromagnetic interference shielding.* CRC Press, 2009.

[138] Y. Danlée, I. Huynen, and C. Bailly. Thin smart multilayer microwave absorber based on hybrid structure of polymer and carbon nanotubes. *Appl. Phys. Lett.*, 100(21),213105, 2012.

[139] R. Lv, F. Kang, D. Cai, C. Wang, J. Gu, K. Wang, and D. Wu. Long continuous $FeNi$ nanowires inside carbon nanotubes: Synthesis, property and application. *J. Phys. Chem. Solids*, 69(5–6),1213–1217, 2008.

[140] R. Lv, F. Kang, J. Gu, X. Gui, J. Wei, K. Wang, and D. Wu. Carbon nanotubes filled with ferromagnetic alloy nanowires: Lightweight and wide-band microwave absorber. *Appl. Phys. Lett.*, 93(22),223105, 2008.

[141] R. Kumar Srivastava, T. N. Narayanan, A. P. Reena Mary, M. R. Anantharaman, A. Srivastava, R. Vajtai, and P. M. Ajayan. Ni filled flexible multi-walled carbon

nanotube-polystyrene composite films as efficient microwave absorbers. *Appl. Phys. Lett.*, 99(11),113116, 2011.

[142] X. Gui, W. Ye, J. Wei, K. Wang, R. Lv, H. Zhu, F. Kang, J. Gu, and D. Wu. Optimization of electromagnetic matching of Fe-filled carbon nanotubes/ferrite composites for microwave absorption. *J. Phys. D: Appl. Phys.*, 42(7),75002, 2009.

[143] M. Crespo, N. Méndez, M. González, J. Baselga, and J. Pozuelo. Synergistic effect of magnetite nanoparticles and carbon nanofibres in electromagnetic absorbing composites. *Carbon*, 74,63–72, 2014.

[144] A. P. Singh, P. Garg, F. Alam, K. Singh, R. Mathur, R. Tandon, A. Chandra, and S. Dhawan. Phenolic resin-based composite sheets filled with mixtures of reduced graphene oxide, γ-Fe2O3 and carbon fibers for excellent electromagnetic interference shielding in the X-band. *Carbon*, 50(10),3868–3875, 2012.

[145] T. Wang, Z. Liu, M. Lu, B. Wen, Q. Ouyang, Y. Chen, C. Zhu, P. Gao, C. Li, M. Cao, and L. Qi. Graphene–Fe_3O_4 nanohybrids: Synthesis and excellent electromagnetic absorption properties. *J. Appl. Phys.*, 113(2),024314–024318, 2013.

[146] K.-Y. Park, J.-H. Han, S.-B. Lee, J.-B. Kim, J.-W. Yi, and S.-K. Lee. Fabrication and electromagnetic characteristics of microwave absorbers containing carbon nanofibers and NiFe particles. *Compos. Sci. Technol.*, 69(7-8),1271–1278, 2009.

[147] R. C. Che, C. Y. Zhi, C. Y. Liang, and X. G. Zhou. Fabrication and microwave absorption of carbon nanotubes/$CoFe_2O_4$ spinel nanocomposite. *Appl. Phys. Lett.*, 88(3),033105, 2006.

[148] F. Wen, F. Zhang, and Z. Liu. Investigation on Microwave Absorption Properties for Multiwalled Carbon Nanotubes/Fe/Co/Ni Nanopowders as Lightweight Absorbers. *J. Phys. Chem. C*, 115(29),14025–14030, 2011.

Objectives and motivation

This work has been principally focused on the preparation of efficient GHz-EMI shielding composites with magnetic nanoparticles and nanocarbons. In light of this commitment, we have explored the adjustment of the shielding performance of our composites by affecting such parameters as their conductivity, electric permittivity and magnetic permeability. Through this research project, we have therefore pursued to:

• Discern the individual role of magnetic and conductive nanoinclusions on the EMI shielding behavior of composites.

• Evaluate the outcome of combining both conductive and magnetic inclusions on the shielding properties of composites.

• Study the effects of increasing the conductivity of composites by means of increasing the aspect ratio of the nanoiclusions and by favoring their interconnection within the matrix.

• Control the macroscopic-scale distribution and the interconnectivity of the nanoinclusions in composites to limit the reflectivity while enhancing their absorption ability.

CHAPTER 2

METHODS & CHARACTERIZATION TECHNIQUES

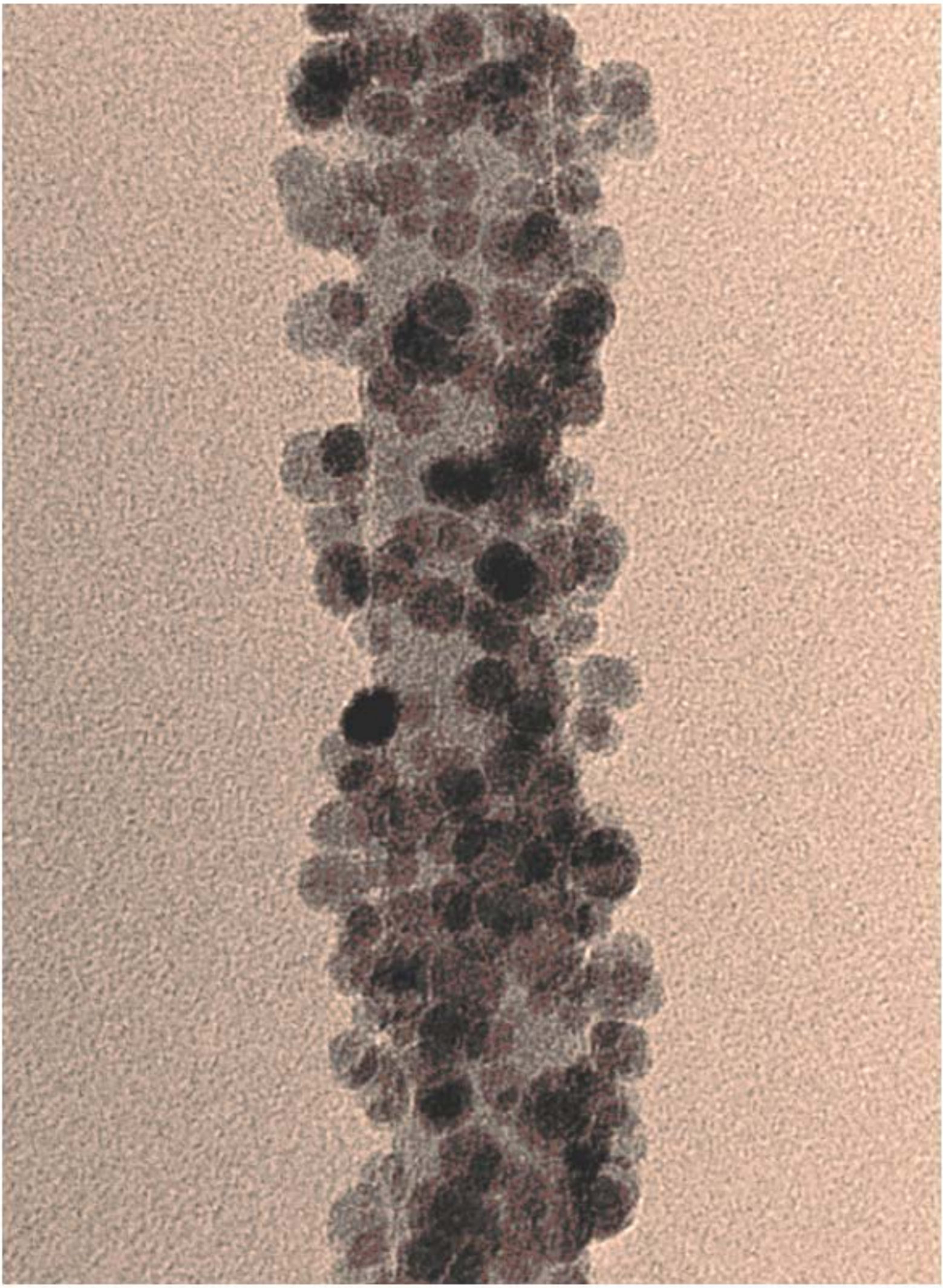

Methods and characterization techniques

2.1 Synthesis procedures

2.1.1 Nanoferrite-filled silica micro particles and epoxy composites

Copper-nickel ferrite nanoparticles ($Ni_{1-x}Cu_xFe_2O_4$) were synthesized *via* an impregnation-calcination procedure using mesoporous silica gel as hard template (Aldrich Ref. 288500, particle size: 2-25 μm and pore size: 60 Å) and the resulting silica-ferrite hybrid was dispersed in an epoxy resin (RTM-6). A general scheme of the method is depicted in Figure 2.1, where it is seen the double scale dispersion control of the process: the nanoscale dispersion of ferrite nanoparticles inside the silica microparticles and the microscale dispersion of the hybrid silica-ferrite particles in the epoxy resin.

Nanoparticles were synthesized through the general casting procedure developed by Fuertes et al.[1] Appropriate amounts of $Fe(NO_3)_3 \cdot 9H_2O$, $Ni(NO_3)_2 \cdot 6H_2O$ and $Cu(NO_3)_2 \cdot 2.5H_2O$ (from Sigma Aldrich) were mixed to prepare $Ni_{1-x}Cu_xFe_2O_4$ ferrites with the following stoichiometries: $x = 0$, 0.25, 0.5, 0.75 and 1.

The metallic nitrates were dissolved in 16 gr of ethanol and the resultant solution was used to impregnate the silica gel. The wet nitrate-silica was dried at 90 $°C$ overnight and the impregnation-drying process was repeated in order to increase the metal content inside the silica pores. The thermal decomposition of the nitrates was carried out in an electric furnace, using N_2 as inert atmosphere, for 4 h at 700 or 900 $°C$ using a 5 $°C \cdot min^{-1}$ heating ramp.

Detemplation of $Ni_{0.5}Cu_{0.5}Fe_2O_4$ ferrite nanoparticles was done by stirring the ferrite/silica powders in a 2M $NaOH$ solution for 24 h. The detemplated particles were then dispersed in an NH_4OH solution of pH=9-10, placed in an ultrasonic bath at 70-80 $°C$ and oleic acid was added until pH 7 was reached. The oleic acid coated

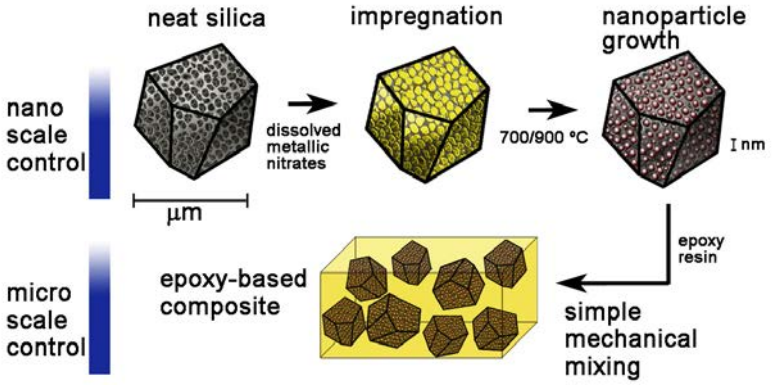

FIGURE 2.1: Synthesis of ferrite nanoparticles inside the pores of a mesoporous silica hard template (top) and preparation of composites with a double-scale dispersion control

nanoparticles were then rinsed several times with acetone and hot water to remove the excess of oleic acid and the non-reacted metallic nitrates.

Composites were prepared using HexFlow ® RTM-6 (supplied by Hexcel Corporation) as the epoxy matrix. The nanoferrite-filled silica particles were added to the resin, mechanically stirred for 15 min at 80-90 $°C$ and degassed in vacuum. The mixtures with different filler contents (10, 15, 20 and 25 $wt\%$) were poured into pre-heated silicone molds (120 $°C$) and cured 75 min at 160 $°C$ followed by a post-curing step of 120 min at 180 $°C$.

2.1.2 Epoxy composites of pristine and magnetite-decorated CNFs

CNFs were kindly supplied by Grupo Antolín S.A. (Spain). Magnetite nanoparticles were synthesized starting with $FeCl_2 \cdot 4H_2O$, $FeCl_3 \cdot 6H_2O$, NH_4OH (28 $vol\%$) and oleic acid, which were purchased from Sigma-Aldrich and used without any further purification. The hydrogenated derivative of diglycidyl ether of bisphenol-A (HDGEBA) epoxy resin was supplied by CVC Specialty Chemicals (USA); the epoxy equivalent mass was $210 g \cdot mol^{-1}$, as determined by acid titration. m-xylilenediamine (m-XDA,

Sigma-Aldrich) was used as curing agent and tetrahydrofuran (THF, Sigma Aldrich) was used to dilute the epoxy resin.

Oleic acid capped-magnetite nanoparticles (Mag), were prepared and characterized as in previous works done in our laboratories[2]. In a typical experiment, 14.5 g of $FeCl_3 \cdot 6H_2O$ and 5.37 g of $FeCl_2 \cdot 4H_2O$ were dissolved in 300 mL of deionized water with the aid of an ultrasonic bath and mechanical stirring at 70-80 $°C$. Subsequently, 25 mL of a 25% NH_4OH solution were rapidly injected. The mixture turned black instantly, as a consequence of the precipitation of magnetite. Then 10 mL of oleic acid was added to the suspension while stirring vigorously for 2 h. The black fine magnetite precipitate was separated from the solution using a magnet and washed several times with hot deionized water and acetone, to remove non reacted metallic salts and the excess of oleic acid respectively, and dried in vacuum.

The preformed oleic acid-capped magnetite nanoparticles and the CNFs were separately dispersed in heptane by sonication and mechanical stirring, then mixed (1:1 mass ratio) and further sonicated for 10 min to ensure the adsorption of magnetite over the CNFs. Modified nanofibres were removed from the dispersion using a magnet leaving a completely clear and transparent supernatant, which corroborates the complete adsorption of magnetite onto the CNFs. The precipitate was finally dried in vacuum.

Three different composites were prepared: epoxy-Mag, epoxy-CNF, and epoxy-CNF/Mag. The amount of CNFs or magnetite in the two former composites was: 1, 2.5, 5 and 10 $wt\%$. The amount of CNF/Mag was selected to give an equivalent total amount of Mag or CNFs with respect to the epoxy/magnetite and the epoxy/CNF composites: 2.5, 5, 10 and 20 $wt\%$; for example, the 10 $wt\%$ CNF/Mag composite contains 5 $wt\%$ of magnetite and $5wt\%$ of CNFs. From $wt\%$, volume fractions were calculated by the following expression:

$$\Phi = \left[1 + \frac{(1-\omega)\,\rho_i}{\omega_i \rho_e}\right]^{-1} \tag{2.1}$$

where ω_i and ρ_i refer to the mass fractions and density of either magnetite, CNF or CNF/Mag, and ρ_e is the density of epoxy (1.25 $g \cdot cm^{-3}$). The magnetite nanoparticle's density was calculated from the mass fractions determined through TGA [2] and the known densities of crystalline magnetite (5.15 $g \cdot cm^{-3}$) and oleic acid (0.895 $g \cdot cm^{-3}$). The extracted value was 2.6 $g \cdot cm^{-3}$. The CNFs density (1.97 $g \cdot cm^{-3}$, as given by the supplier) and the magnetite nanoparticle's density were used to determine the density of CNF/Mag through the following expression:

$$\rho_{CNF:Mag} = \frac{2}{\left[\rho_{CNF}^{-1} + \rho_{Mag}^{-1}\right]} \tag{2.2}$$

The correspondence between volume and weight percentages is summarized in Table 2.1.

TABLE 2.1: Weight percentages ($wt\%$) and equivalent volume percentages ($vol\%$) of CNFs and CNF/Mag in the epoxy composites

Nanofiller, wt%	**1**	**2.5**	**5**	**10**	**20**
CNF (***vol***%)	0.6	1.6	3.2	6.6	-
CNF/Mag (***vol***%)	-	1.2	2.9	5.8	12.2

For the preparation of nanocomposites, both the filler and HDGEBA were diluted in THF, mechanically stirred and sonicated at room temperature to give stable suspensions. After mixing, the solvent was eliminated at 80°C under vaccuum. Stoichiometric amounts of m-xylilenediamine were added to the mixtures and cured at 90 °C for 1 h and post-cured for 2 h at 130 °C to ensure full conversion.

Concerning the polymeric matrix, the main feature of HDGEBA is the lack of aromaticity in its cycles, or the absence of phenyl groups in its structure. Its low polarity and the presence of flexible cyclohexyl groups instead of rigid aromatic rings makes the viscosity of HDGEBA appreciably lower than that of standard DGEBA epoxy

based resins. Fluidity joined with moderate glass transition temperature, makes this selection adequate for coatings, manufacture of complexly shaped components and encapsulation [3] of electronic devices in applications where temperature requirements are not severely stringent.

2.1.3 3D CNT-scaffolds and epoxy composites prepared by their infiltration

Nitrogen doped multiwalled carbon nanotubes (CNxCNTs) were synthesized by Chemical Vapor Deposition (CVD) in a horizontal furnace at 850 $°C$ [4]. Ferrocene and benzylamine were used as catalyst and carbon source respectively. The benzylamine solution with a 2.5 $wt\%$ of catalyst was introduced into the furnace using an ultrasonic sprayer. The carrier gas flow (Ar/H_2, 1:0.15 mixture) was set at a constant feeding rate of 2.5 L/min and carbon nanotubes were allowed to grow for 30 min.

The prepared CNxNTs were functionalized by acid oxidation [5] ($H_2SO_4 : HNO_3/3 : 1$) and densely decorated with nearly monodisperse magnetite nanoparticles ($\sim$ 7 nm) *via* a polyol route, using triethylene glycol as the solvent and iron acetylacetonate ($Fe(acac)_3$, 99.99%) as the organometallic precursor [6]. Briefly, the oxidation was done by mixing pristine CNxNTs with the acid mixture (ratio: 1mg/ml) and letting it to react for 2 h in an ultrasonic bath. The carbon nanotubes were collected afterward by vacuum filtration and repeatedly rinsed with water until a neutral pH was reached. The product was then dried in vacuum. For the magnetite decoration, 500 mg of the oxidized CNxNTs were dispersed in 150 ml of triethylene glycol for 5 min in an ultrasonic bath. After this time 1 gr of $Fe(acac)_3$ was added while stirring vigorously. The mixture was reflux-heated at 3 $°C{\cdot}min^{-1}$ until 278 $°C$ and kept at this temperature for 30 min. The product (CNxMag) was collected by vacuum filtration, rinsed several times with ethanol and dried in vacuum for obtaining a highly magnetic black powder.

Oxidized and pristine nanotubes were titrated to quantify the acidic moieties on their surface. Small quantities (ca. 7-15 mg) were suspended in approximately 60 ml of distilled water and pH changes upon addition of consecutive volumes of the $NaOH$ solution were automatically monitored. Acidic sites quantification was done at the last equivalence point (pH=7.1-7.6).

Magnetite decorated and pristine CNxNT scaffolds were prepared as previously described[7], through *Ice segregation induced self-assembly* (ISISA). First chitosan (CHI) solutions (1 $wt\%$) were prepared by dissolving CHI (0.1 g) in 10 ml of an aqueous solution of acetic acid (0.15 M, pH 4.5). Subsequently, 3.4 and 6.7 $wt\%$ of pristine CNxNTs or CNxMag nanotubes were dispersed in CHI solutions (1 wt%) and stirred at room temperature for 24 h. The dispersions were collected into syringes (1 ml or 5 ml) and dipped at a constant rate of 2.7 $mm \cdot min^{-1}$ into a cold bath maintained at a constant temperature of a -196 $°C$ (liquid nitrogen). The unidirectionally frozen samples were freeze-dried using a ThermoSavant Micromodulyo freeze-drier. The resulting monoliths kept the shape of the container.

During unidirectional freezing, steadiness between the cryogenic liquid level and the ice front is only established after reaching a certain immersion height. Thereby, the final aerogels present a heterogeneous porosity distribution along their longitudinal axis. Below this critical height, the morphology of the ice crystals is not well established and the porosity of the aerogel varies strongly, from a dense to a cellular-like structure. Above that point, since the temperature of the cryogenic liquid is constant, steady ice crystals with uniform size and structure start growing aligned with the freezing direction. Therefore, the first 2 cm of each scaffold were discarded to avoid extra effects from an unknown structure. For comparison purposes, an scaffold with 6.7 $wt\%$ of CNxMag in the primary aqueous solution was subjected to thermal treatment under N_2 atmosphere. The CNxMag 6.7 % scaffold was carefully placed in the middle of a tubular furnace, heated at 2 $°C/min$ until 250 $°C$ and kept at this temperature for

30 min. The sample was then subjected to the second temperature ramp, 3 $°C \cdot min^{-1}$, to reach 360 $°C$ and maintained at these conditions for 1 h.

Composites of all the prepared scaffolds were obtained after infiltration with HDGEBA mixed with the corresponding stoichiometric quantity of curing agent (m-xylilendiamine). The resin was selected due to its low viscosity, which allows for a better penetration of the epoxy within the scaffold's structure. Infiltration was done under vacuum conditions inside glass tubes. The prepared composites were cured using the usual protocol (1 h at 80 $°C$ and 1 h at 120 $°C$). The scheme of the complete process is depicted in Figure 2.2.

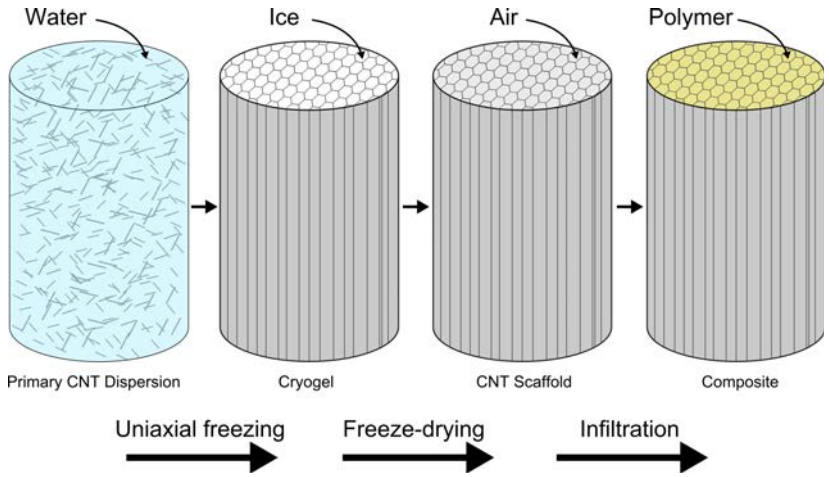

FIGURE 2.2: Illustration of the process used to obtain CNT-scaffolds and scaffold composites. Anisotropic CNT-scaffolds are obtained upon uniaxial freeze-drying aqueous dispersions of CNTs and the polymeric binder. Epoxy composites are obtained after infiltrating these hollow CNT structures

2.1.4 3D CNT-sponges directly synthesized by chemical vapor deposition

As shown in Figure 2.3, 3D/CNT-sponges were synthesized through chemical vapor deposition (CVD) in a horizontal furnace at 860 $°C$ (Thermo Scientific Lindberg M

Mini-Mite, 120V) equipped with a 1-inch diameter quartz tube. Ferrocene and 1,2-dichlorobenzene (DCB) were used as catalyst and carbon source respectively. The DCB solution with a catalyst concentration of 0.06 g/ml was injected into a preheated zone (240 $°C$) with a syringe pump at constant rates of 0.23, 0.18 and 0.13 $ml \cdot min^{-1}$. The vaporized mixture is conducted into the 860 $°C$ furnace zone (center) by the carrier gas (Ar/H_2, ratio 1:0.15) which was set at a constant feeding rate of 2.6 L/min. The sponge material was then allowed to grow for 1, 2, 3 or 4 h. As CNTs grow, they get randomly deposited on the quartz tube walls, or over quartz substrates, forming the sponge. The system was subsequently cooled to room temperature while maintaining the carrier gas flow at 0.5 L/min. Sponge thicknesses, when the growth was done for 2 h, was typically ∼2-3.5 mm.

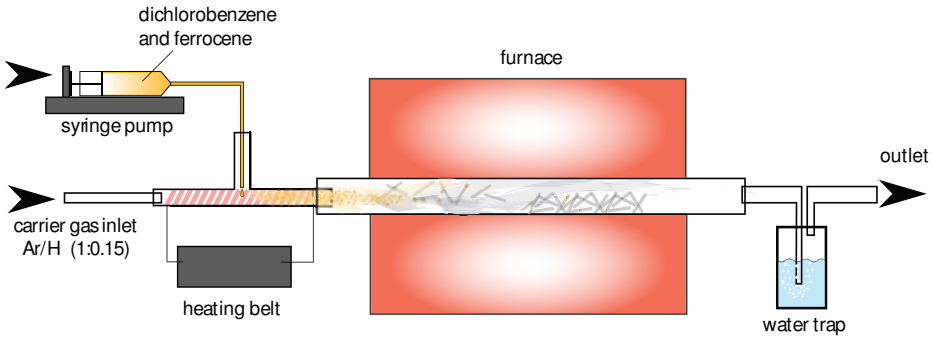

FIGURE 2.3: Setup for the synthesis of CNT-sponges. The CNT precursor solution is injected with a syringe pump into a preheated zone, where it is vaporized and carried inside the furnace by the Ar/H_2 mixture. Inside the furnace, at 860 $°C$, small particles of ferrocene catalyze the growth of CNTs from the carbon source

2.2 General characterization techniques

• Powder X-ray diffraction (XRD)

The interaction of X-rays (monochromic and collimated) and atoms of crystalline matter produces constructive diffraction interferences when Bragg's law is satisfied. Thereby, for structures having n crystalline planes, the radiated wavelength (λ) is related to the crystalline lattice spacing (d) and the diffraction angle (θ) by:

$$n\lambda = 2d\sin\theta \tag{2.3}$$

As θ is characteristic for each periodic array of atoms, XRD enables to determine the composition of samples through the discrimination of its crystalline structure. Additionally, the crystallite size (D) of polycrystalline samples can be calculated from XRD patterns by using Scherrer's equation:

$$D = \frac{K\lambda}{\beta\cos\theta} \tag{2.4}$$

where K is the shape factor and β is the diffraction peak broadening (width at half-height) in radians. For spherical crystalline grains, the shape factor is 0.9 and D corresponds to the grain size, while for nanoparticles, it can reflect the size of the particle.

The crystalline structure of materials was studied with a Panalytical X'pert Pro X-ray diffractometer (Cu K_α radiation, $\lambda = 0.15406\ nm$).

• Brunauer-Emmet-Teller (BET) surface area

This technique enables the determination of the material's specific surface, the porosity at the nanoscale level and its distribution. It is based on the adsorption of monolayers of N_2 molecules over the surface of the material. The thickness of this layer increases progressively as the equilibrium pressure reaches the saturation pressure. During this process, it is possible to assess the type of adsorption that the surface of the sample undergoes. The application of mathematical models to the raw pressure data enables obtaining the nanoporosity of samples: geometry, size and distribution of the pores.

Nitrogen adsorption measurements were used to characterize the nanoferrite-silica hybrids. Both the pores of the silica template and the ferrite filled silica were characterized at -196 $°C$ on a Micrometrics Instrument Corp. Gemini VII 2390. The samples (*ca.* 200 mg) were previously degassed for 1 h at 90 $°C$ and 2 h at 150 $°C$. The surface area was determined using the Brunauer-Emmet-Teller (BET) method from 0.05 to 0.25 relative pressures. The pore size distribution was determined using the desorption branch and the Barret-Joyner-Haelender (BJH) method. The total pore volume was measured at $P/P_0 = 0.99$.

• Vibrating sample magnetometry (VSM)

In VSM, a uniform magnetic field is applied to the sample and its dipole field is measured as it oscillates perpendicularly to the magnetic field [8]. The principle of this technique is the Faraday's law of induction, which states that any alternating magnetic field will produce a measurable electric field. While the sample gets magnetized the generated magnetic field generates an electric field that can be sensed. This current is proportional to the magnetization of the sample.

The magnetic properties of magnetic particles were investigated by Vibrating Sample Magnetometry (VSM) at room temperature with a 10 T magnetic field (CFMS Cryogenic Ltd). The coercitivity (H_C) and remanence values (M_r) were obtained from the

hysteresis loops. The saturation magnetization (M_s) was obtained by extrapolating the magnetization in the linear portion, observed at high fields, of the hysteresis loops.

• Raman spectroscopy

Raman spectroscopy is a fast, nondestructive and high-resolution technique that enables the discernment of carbon allotropes, the evaluation of their chemical modifications during processing (structure preservation, defects, functional groups) and the determination of unwanted synthesis byproducts. Raman scattering of phonons is determined by the electronic behavior of the material and any change in its structure will lead to a change in shape, position and intensity of the Raman bands. The main signals in the Raman spectra (Vis excitation) of carbonaceous materials are the G and D bands, observed around 1560 and 1360 cm^{-1} respectively. G peak occurs due to bond stretching of sp^2 C-C bonds and is observable both in chains and rings. The D peak is due to breathing of sp^2 C-C bonds in six-atoms rings and requires defects for its activation. Among these bands, in non-defective graphitic structures only G band is observable, together with the 2D band at 2635 cm^{-1} (D overtone), which does not require defects for being active either. In this context, the ratio between D and G bands is usually assessed to evaluate how defective or graphitic the structure is.

Nanocarbons and their derivatives were subjected to Raman spectroscopy with a Renishaw inVia confocal micro-Raman spectrometer equipped with a 100× objective and a 514 nm laser as excitation source. Measurements were done with two acquisitions of 30 s in 5 different points of each sample.

• Thermogravimetric Analysis (TGA)

All measurements involving thermogravimetric analysis (TGA) were carried out in air if not otherwise specified. TGA was used to determine the different oxidation/degradation processes of polymer composites and also to estimate the quantity of thermally

stable inclusions by considering the wt% of residue at 900 $^{\circ}C$. Typical experiments were done with 3-12 mg of sample and the weight loss was monitored between 40 and 900 $^{\circ}C$ using a heating ramp of 10 $^{\circ}C \cdot min^{-1}$. The peaks of the derivatives of the TGA curves were assessed as maximal degradation rates. Although the same conditions were maintained for all measurements and within each group of materials all TGA's were carried out with the same equipment, a Perkin Elmer STA 6000 and a TA Instruments Q500 TGA were used indistinctly.

• Differential scanning calorimetry (DSC)

Thermal transitions were studied by Differential Scanning Calorimetry (DSC) on a Mettler Toledo 822 equipment, from 40 to 240 $^{\circ}C$ at 10 $^{\circ}C \cdot min^{-1}$. The glass transition temperature in all cases was determined at the inflexion point of the recorded thermograms.

• Electron microscopy

The morphology of composites was characterized by Scanning Electron Microscopy (SEM) on a Philips XL30 microscope operating at 15 kV and equipped with detector of secondary electrons. Samples were sputtered with gold during 30 s to avoid charge accumulation during SEM inspection.

Transmission electron microscopy (TEM) and high-resolution TEM (HRTEM) images, as well as selected area electron diffraction (SAED) patterns, were obtained on a Philips Tecnai microscope at 200 kV. Powder samples were sonicated in small amounts of acetone or ethanol and then dropped over TEM Cu-grids coated with amorphous carbon. In the cases when TEM images of composites were needed, specimens were cut into $\sim$70 nm sections with a Leica UltraMicrotome EM UC7 and deposited over the carbon coated Cu-grids.

• Direct current (DC) electrical measurements

Electrical properties of materials were evaluated using a HP 34401A digital multimeter with 100 $\mu m \cdot \Omega^{-1}$ resolution and 10 $G \cdot \Omega^{-1}$ upper limit. In a 2-wire DC configuration, I-V curves were recorded from 1 to -1 Volts and the mean resistance was obtained from the slope. Conductivity (σ) was calculated accounting the dimensions of samples by:

$$\sigma = \frac{1}{R\frac{A}{L}} \tag{2.5}$$

where σ is given in $(S \cdot m^{-1})$, R is the measured resistance in (Ω), L is the length of the sample or the distance between electrodes in m, and A is the area of the sample's surface (width $\times$ thickness, m^2) in contact with the electrode.

The electrical properties of CNF-epoxy and CNF/Mag-epoxy composites were evaluated with samples prepared by placing a drop of the uncured blends between two steel plates (diameters: 2.4 and 3 cm) and then curing through the usual protocol. The thickness of these samples was controlled using 100 μm Teflon® spacers placed between the steel disks.

In the case of CNT-sponges, the specimens were cut into rectangular (5 $\times$ 7 mm) or square (5 $\times$ 5 mm) sections with thickness of about 3 mm. The top and bottom surfaces were carefully stuck to aluminum plates, serving as electrodes (10 $\times$ 10 mm^2), by applying a thin layer of silver paint.

In the case of composites prepared by the infiltration of 3D-CNT scaffolds, electrical properties were measured in toroidal specimens having inner and outer diameters of 3 and 7 mm, respectively, and thicknesses of about 2 mm. The top and bottom surfaces were carefully polished and coated with a thin layer of silver paint, where a silver wire was adhered.

2.3 EMI shielding measurements

The shielding efficiency was measured according to the transmission/reflection method though a two-port vector network analyzer (VNA, Agilent, ENA, E5071) in the range of 1 to 18 GHz. This apparatus allows for the characterization of microwave devices, circuits and the properties of materials at the specified frequencies. Samples were characterized with a 7 mm outer and 3.04 mm inner diameter coaxial transmission line adapter. Samples were precisely machined into toroidal shapes and inserted within the coaxial sample holder as depicted in Figure 2.4. Using the built-in software, a geometry correction was applied for correcting small deviations from nominal geometry.

The coaxial transmission line is connected to the two ports of the VNA, namely port-1 and port-2, one to each side of the line. The VNA generates an input signal of certain frequency in port-1, which is conducted through the line until it reaches the material under test. The material will partly reflect this signal and the non-reflected signal will be transmitted to port-2. The reflected portion will be recollected in port-1 and separated from the input one. The VNA then sweeps along the established frequency range and collects both reflected and transmitted waves. This is done in both directions, e.g. input signal from port-2 to port-1, thereby four sets of data are generated. These can be mathematically represented by four complex scattering parameters: S_{11}, S_{21}, S_{22} and S_{12}, in which the numbers denote the receiver port and the source port, respectively.

The S-parameters are related to the voltage of the reflected (R) and incident (I) waves and can be correlated with the respective powers (P) by:

$$P_R = |S_{11}|^2 = |S_{22}|^2 \tag{2.6}$$

$$P_T = |S_{12}|^2 = |S_{21}|^2 \tag{2.7}$$

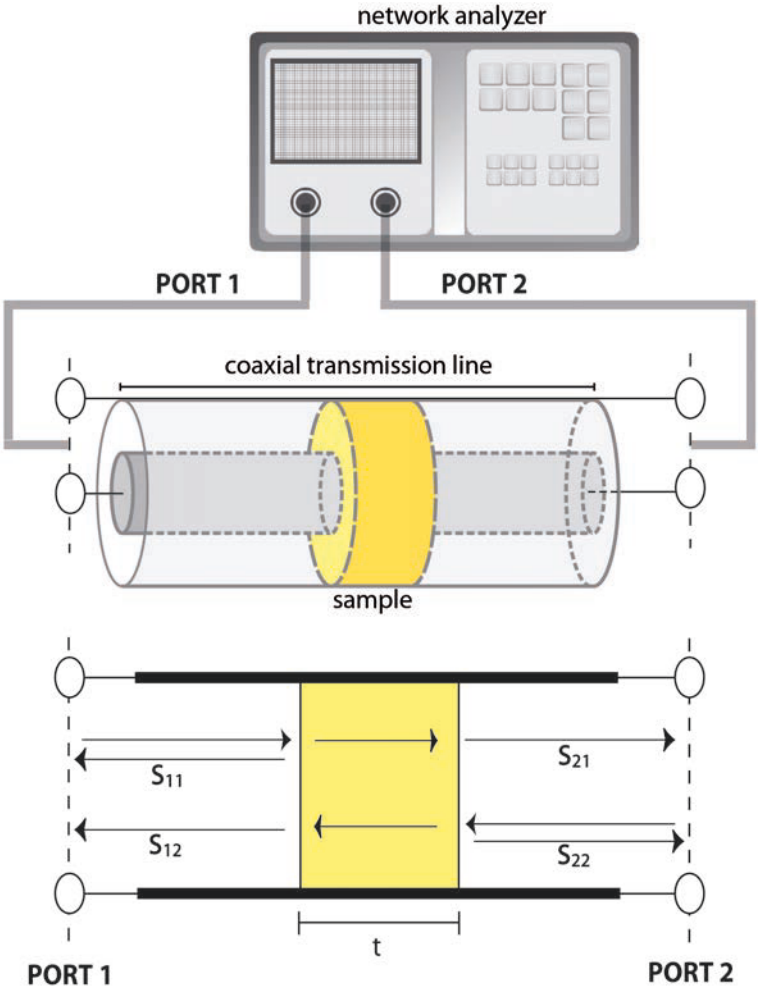

FIGURE 2.4: Illustration of the network analyzer on top, connected to the coaxial transmission line, which is loaded with the toroidal sample within the outer and inner conductors. The illustration at the bottom shows the plane representation of the S-parameters, e.g. when the input signal is generated at port 1, the reflected signal collected back at port 1 is represented by S_{11}, while the transmitted portion of the input signal is collected at port 2 and is represented by S_{21}

Thus, the absorbed power (P_A) can be calculated taking into account that the incident power (P_I) is 1 mW as:

$$P_A = 1 - P_R - P_T = 1 - |S_{11}|^2 = |S_{12}|^2 \tag{2.8}$$

To reflect the loss of incident power, as the wave strikes the material and passes trough it, the S-parameters can be conveniently assessed to obtain the global shielding efficiency and to separate the absorption and reflection loss contributions as:

$$SE_T = 10 \log \frac{P_I}{P_T} = SE_R + SE_A = 10 \log \frac{1}{|S_{21}|^2} \tag{2.9}$$

$$SE_R = 10 \log \frac{P_I}{P_I - P_R} = 10 \log \frac{1}{1 - |S_{11}|^2} \tag{2.10}$$

$$SE_A = 10 \log \frac{P_I - P_R}{P_T} = 10 \log \frac{1 - |S_{11}|^2}{|S_{21}|^2} \tag{2.11}$$

To find the complex permittivity and permeability of samples, an algorithm based on the Nicholson-Ross-Weir method[9] was applied to the S-parameters with the built-in software.

Briefly, given that $S_{12} = S_{21}$, the S-parameters can be expressed as a function of the reflection (Γ) and transmission (T) coefficients by[10]:

$$S_{11} = R_1^2 \left[\frac{\Gamma \left(1 - \mathrm{T}^2\right)}{\left(1 - \Gamma^2 \mathrm{T}^2\right)} \right] \tag{2.12}$$

$$S_{22} = R_2^2 \left[\frac{\Gamma \left(1 - \mathrm{T}^2\right)}{\left(1 - \Gamma^2 \mathrm{T}^2\right)} \right] \tag{2.13}$$

$$S_{21} = R_1 R_2 \left[\frac{\mathrm{T} \left(1 - \mathrm{T}^2\right)}{\left(1 - \Gamma^2 \mathrm{T}^2\right)} \right] \tag{2.14}$$

where R_1 and R_2 are related to the reference planes and their distance to the sample ends from each side of the coaxial line. Γ and T are defined by the complex propagation constant (γ) within the material, the thickness of the slab (t) and its complex magnetic permeability respectively (μ)by[10]:

$$\mathrm{T} = e^{-\gamma t} \tag{2.15}$$

$$\Gamma = \frac{\left(\frac{\gamma_0}{\mu_0} - \frac{\gamma}{\mu}\right)}{\left(\frac{\gamma_0}{\mu_0} + \frac{\gamma}{\mu}\right)} \tag{2.16}$$

where γ_0 is the propagation constant in vacuum. At the same time the complex propagation constant is related to the complex permittivity (ϵ) and permeability (μ) of the sample by[11]:

$$\gamma = j\sqrt{\epsilon_r \mu_r}\frac{2\pi f}{c_0} \tag{2.17}$$

Therefore, solving this complex matrix through the Nicholson-Ross-Weir algorithm enables the VNA to retrieve the four unknowns: ϵ', ϵ", μ' and μ".

In order to obtain the reflection and transmission parameters of the material under test with accuracy, the system must be calibrated prior to measurement. For understanding the calibration sequence, the coaxial line connected to the VNA through port 1, can be simplified to the equivalent circuit illustrated in Figure 2.5. Calibration is done for each port with three standards: an open connector, a short connector and a matched impedance load connector, all of which are plugged to the opposite end of the line to which calibration is being done (Figure 2.5). This procedure allows removing systematic errors that affect the reflection terms, such as the directivity of the signal, the impedance match of the source and the reflection tracking[12].

Once both ports have been calibrated, transmission through the empty line is measured for setting the maximum transference between ports.

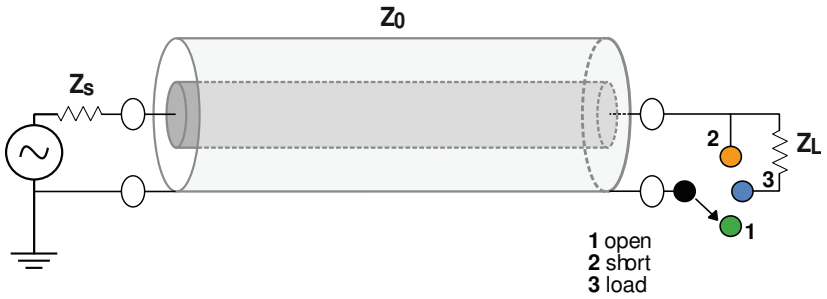

FIGURE 2.5: Equivalent circuit of the coaxial line connected to the source from port 1, where Z_s is the source impedance, Z_0 is the characteristic impedance of the coaxial line and Z_L is the impedance of the load standard that is used for calibration, which is equal to the impedance of the test system (50 Ω). Before the load standard is used, calibration is done with an open and a short standard. These three manipulations complete the one-port calibration

Bibliography

[1] T. Valdés-Solís, P. Tartaj, G. Marbán, and A. B. Fuertes. Facile synthetic route to nanosized ferrites by using mesoporous silica as a hard template. *Nanotechnol.*, 18(14),145603, 2007.

[2] M. González, I. Martín-Fabiani, J. Baselga, and J. Pozuelo. Magnetic nanocomposites based on hydrogenated epoxy resin. *Mater. Chem. Phys.*, 132(2-3),618–624, 2012.

[3] C. May. *Epoxy resins: chemistry and technology.* Marcel Dekker, Inc., 1987.

[4] M. Terrones, P. M. Ajayan, F. Banhart, X. Blase, D. L. Carroll, J. C. Charlier, R. Czerw, B. Foley, N. Grobert, R. Kamalakaran, P. Kohler-Redlich, M. Rühle, T. Seeger, and H. Terrones. N-doping and coalescence of carbon nanotubes: synthesis and electronic properties. *Appl. Phys. A*, 74(3),355–361, 2002.

[5] K. Jiang, A. Eitan, L. L. S. Schadler, P. M. Ajayan, R. W. Siegel, N. Grobert, M. Mayne, M. Reyes-Reyes, H. Terrones, and M. Terrones. Selective attachment of gold nanoparticles to nitrogen-doped carbon nanotubes. *Nano Lett.*, 3(3),275–277, 2003.

[6] J. Wan, W. Cai, J. Feng, X. Meng, and E. Liu. In situ decoration of carbon nanotubes with nearly monodisperse magnetite nanoparticles in liquid polyols. *J. Mater. Chem.*, 17(12),1188–1192, 2007.

[7] M. C. Gutierrez, Z. Y. Garcia-Carvajal, M. J. Hortiguela, L. Yuste, F. Rojo, M. L. Ferrer, and F. del Monte. Biocompatible MWCNT scaffolds for immobilization and proliferation of E. coli. *J. Mater. Chem.*, 17(29),2992–2995, 2007.

[8] S. Foner. Vibrating Sample Magnetometer. *Rev. Sci. Instrum.*, 27(7),548, 1956.

[9] J. Baker-Jarvis, E. J. Vanzura, and W. A. Kissick. Improved technique for determining complex permittivity with the transmission/reflection method. *IEEE Trans. Microw. Theory Techn.*, 38(8),1096–1103, 1990.

[10] J. Baker-Jarvis. Transmission/reflection and short-circuit line permittivity measurements. *Theory Tech.*, 1990.

[11] J.-M. Thomassin, C. Jérôme, T. Pardoen, C. Bailly, C. Je, I. Huynen, and C. Detrembleur. Polymer/carbon based composites as electromagnetic interference (EMI) shielding materials. *Mater. Sci. Eng., R*, 74(7),211–232, 2013.

[12] Network Analysis Basics - Applying Error Correction To Network Analyzer Measurements, 2002.

CHAPTER 3

RESULTS & DISCUSSION

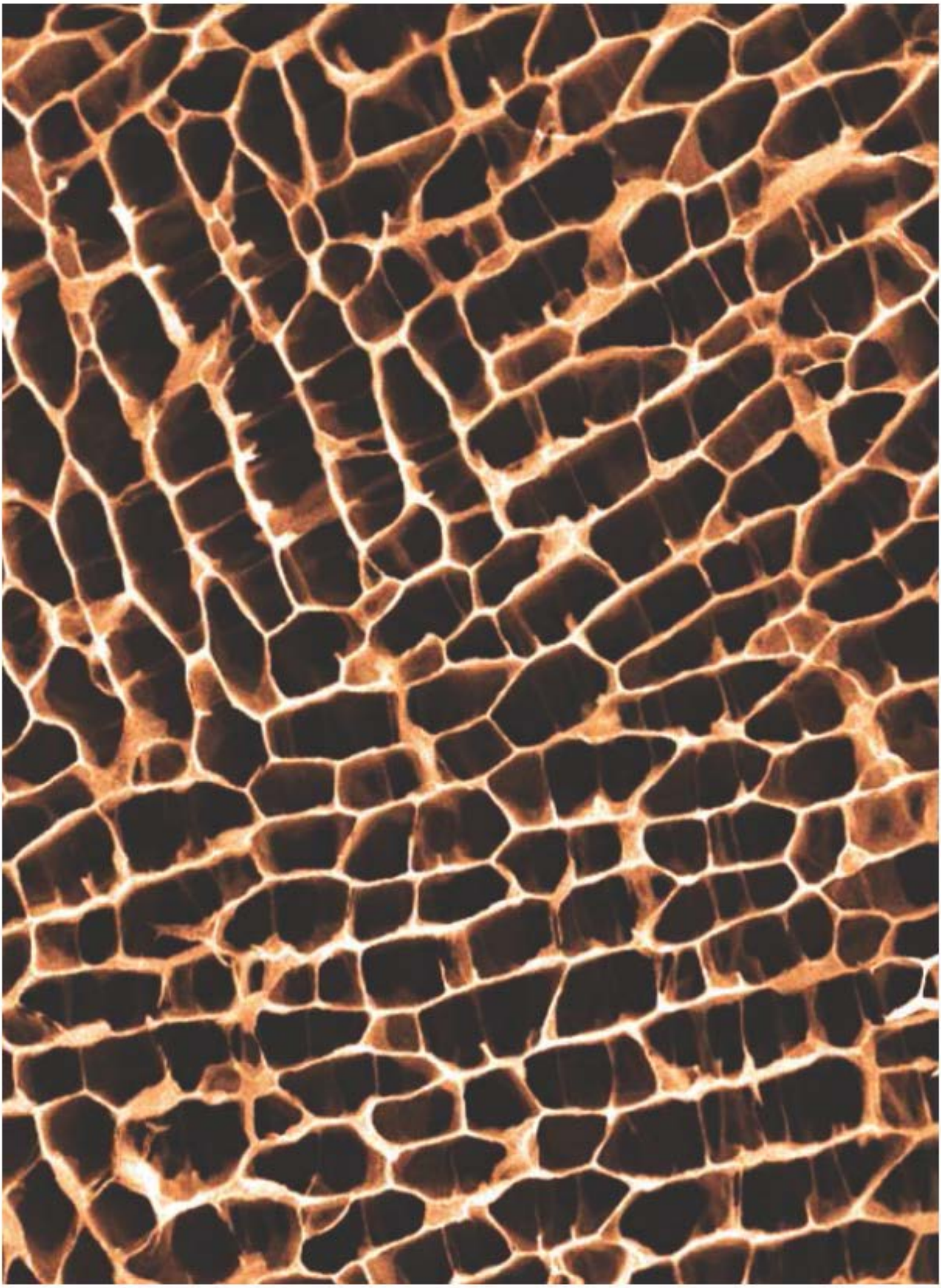

Results and discussion: Preface

In this work we have studied the shielding performance of a variety of materials with different values of conductivity, electric permittivity and magnetic permeability. We have prepared composites with precisely designed nanometric reinforcements, controlled dispersions and specific interconnectivities between them.

Since all the composite systems were prepared for the same final application, this chapter will be divided in two parts: Part I, in which the characteristics of the nanofillers will be discussed and linked to their preparation method, and Part II, where the general properties of composites will be analyzed and related to their EMI shielding ability. For sake of clarity, both parts (I and II) will be divided into four sections, in correspondence to the nanoreinforcements that were prepared and employed for the preparation of composites:

- Nanoferrite-filled silica micro particles[1]
- CNFs and magnetite-adsorbed onto CNFs[2]
- 3D CNT-scaffolds of pristine and magnetite-decorated CNTs[3]
- 3-Dimensional CNT-sponges[4]

[1]Related contents have been partially published in *Mater. Chem. Phys.* [1]
[2]Related contents have been partially published in *Carbon* [2]
[3]Related contents are now in progress for submission
[4]Related contents have been partially published in *Phys. Status Solidi Rapid Res. Lett.* [3]

PART I

DESIGNING THE NANOFILLERS:

Magnetic nanoparticles decoration of nanocarbons and 3D architectures of CNTs

Results & Discussion

PART I

I.1 NANOFERRITE-SILICA HYBRIDS: MAGNETISM, SIZE AND CRYSTALLINITY

The magnetic response of $Cu-Ni$ mixed ferrites can be modulated through their stoichiometry[4]: pure Cu-ferrites present a hard magnetic behavior while Ni-ferrites are soft magnets.

Silica-$(Cu-Ni)$/ferrite hybrids have been synthesized by a simple and cheap nanocasting procedure (Figure 2.1, section 2.1.1). Through this method it is possible to obtain homogeneous and individually distributed magnetic nanocores within the silica pores. The magnetic properties of these hybrids as a function of their $Cu-Ni$ stoichiometry and annealing temperature are discussed below.

I.1.1 $Cu-Ni$ ferrite stoichiometry optimization

Mesoporous silica was selected as the hard template to synthesize $Cu-Ni$ ferrite nanoparticles ($Ni_{1-x}Cu_xFe_2O_4$). Different $Cu-Ni$ stoichiometries were prepared by varying the ratio of the initial Cu/Ni precursors used to impregnate the silica template and then annealed at 700 $°C$ to obtain each Silica-$Ni_{1-x}Cu_xFe_2O_4$ hybrid. The materials were labeled according to their content of Cu: $x = 0$, 0.25, 0.5, 0.75 and 1.

The crystallographic analysis of each stoichiometry was done by X-ray diffraction (Figure 3.1). In all diffractograms, the peaks at $2\theta° = 30.2$, 35.6, 43.5, 53.8, 57.4 and 63.0 can be respectively attributed to the (220), (311), (400), (422), (511) and (440) crystalline planes of a single-phase cubic inverse spinel. Nevertheless, small impurities of hematite were distinguished in most compositions and CuO was also observed in the

case of the sample $x = 0.25$. This feature might indicate that 700 $°C$ is still a low temperature for the complete mixture of Ni and Cu oxides that react to form each ferrite stoichiometry.

For the ferrite containing only Cu ($x = 1$), two phases corresponding to CuO and hematite are clearly seen. Since the structure of the resulting ferrite is not equivalent to the rest of spinel nanocrystals, their evaluation was not further pursued. The broad band at $2\theta \approx 20°$ corresponds to the amorphous silica, which also shows minor crystalline contributions, probably related to small amounts of diatoms (cristoballite syn, trydimite syn, quartz), occurring in natural silica [5].

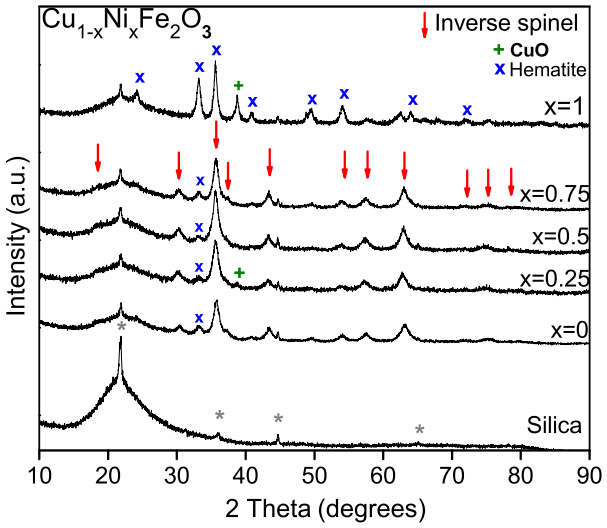

FIGURE 3.1: X-Ray diffraction patterns of the ferrite-silica materials annealed at 700$°C$

The crystallite size (D) of all ferrites (Table 3.1) was determined using Scherrer's equation applied to the most intense diffraction peak (311). Crystallite sizes did not show any clear tendency when the Cu content was varied, suggesting that the size is restricted due to the silica hard template and it is less dependent on the Cu/Ni ratio.

TABLE 3.1: Crystallite size obtained from the XRD patterns of the ferrite-silica materials

$Ni_{1-x}Cu_xFe_2O_4$					
x	0	0.25	0.5	0.75	1
$D\ (nm)$	9.8	9.4	8.6	9.9	-

The magnetic characteristics of the samples were evaluated by registering their magnetic moment while an external magnetic field was applied (vibrating sample magnetometry, VSM). Results for all $Cu-Ni$ ferrite stoichiometries are shown in Figure 3.2. The magnitude of the coercitive (H_C) and remanent (M_R) fields can be observed in the inset. None of the samples show appreciable hysteresis losses (low coecitivity values), suggesting that they are nearly superparamagnetic. The highest value of *ca.* 50 Oe corresponds to the $Ni-ferrite$ ($x = 0$). The coercivity decreases as the content of Cu (x) increases, while the saturation magnetization (Ms) increases with the Cu content, only up to $x = 0.5$.

For single magnetic domain particles, the coercitivity (H_C) increases with the size of the particle (D)[6], as described by[7]:

$$H_C = a_s - \frac{b_s}{D^2} \tag{3.1}$$

where a and b are constants and the subscript s is referred to the single-domain behavior of particles. In the case of particles with more than one magnetic domain (multidomain), the increasing tendency of coercivity with the particle size is inverted, and the relationship is shown by[7]:

$$H_C = a_m - \frac{b_m}{D^2} \tag{3.2}$$

This inversion of trend is observed at a characteristic critical diameter (D_C). For Cu-ferrite, the reported D_C lays around 60 nm[8], meanwhile for the Ni-ferrite it is

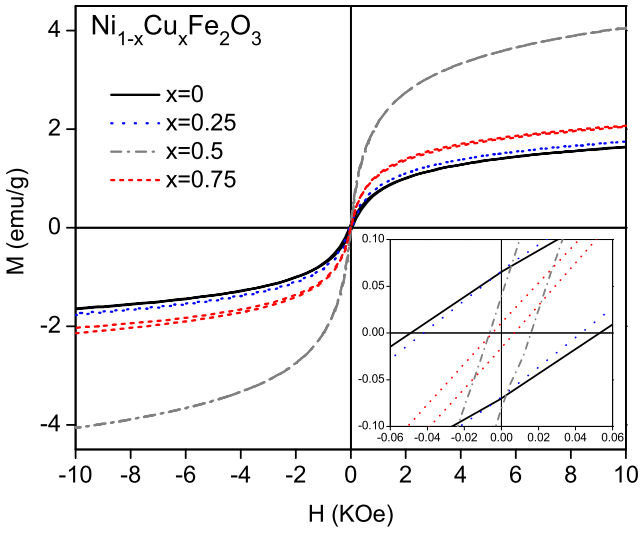

FIGURE 3.2: Hysteresis loops obtained by VSM of the ferrite-silica hybrids with different $Cu-Ni$ stoichiometries. All samples were annealed at 700 $°C$. Inset: Near-zero zoom view of both hysteresis loops showing the variation of coercitivity (x-axis intersection, H_C) and remanence (y-axis intersection, M_R) when the stoichiometry changes.

$\sim$ 11 nm[9]. For $Cu-Ni$ mixed ferrites therefore, it is expected that the diameters will be between these two ranges. The crystallite sizes ($\sim$ 9 nm) tell us that the prepared ferrites might be below or very near the lowest D_C bound (11 nm), thus approaching the superparamagnetic behavior from the monodomain region. Nonetheless, the decreasing trend of coercivity might be justified due to the varying Cu content. Particles of all stoichiometries are small enough to behave as magnetic monodomains, but as the Cu content increases, the intrinsic D_C is also increasing[10]. Thereby, ferrites containing a higher amount of copper, e.g. $x = 0.75$, but having sizes comparable to those of ferrites containing higher amounts of Ni, e.g. $x = 0.25$, have lower coercitivities since they are closer in size to their critical diameter limit. The decrease in coercitivity when Cu^{2+} ions are introduced into the pure Ni-ferrite lattice has been reported previously for particles having sizes of about 10-12 nm[7].

The trend of saturation magnetization (M_S) as a function of the Ni/Cu content can be attributed to the competition for occupying the octahedral sites between ferrimagnetic Fe^{3+} ions (high magnetic moment) and non-magnetic Cu^{2+} ions (lower magnetic moment). Neel's ferrimagnetic theory states that in spinel structures, cations occupying the different positions (octahedral or tetrahedral sublattices) have magnetic moments that are aligned up oppositely. Accordingly, the magnetic moment (η_B) for spinel structures is given by: $\eta_B = \eta_{OCT} - \eta_{TET}$, where OCT and TET respectively correspond to the magnetic moment of the octahedral and tetrahedral sublattices.

Ni-ferrite is generally represented by the formula: $\left[Fe^{3+}\right]_{TET}\left[Ni^{2+}, Fe^{3+}\right]_{OCT} O_4^{2-}$, which implies that the tetrahedral sites are preferentially occupied by the Fe^{3+} ions. When Cu^{2+} are introduced in the Ni-ferrite lattice, for compositions comprised between $0 < x < 0.5$, Cu^{2+} ions will occupy the tetrahedral positions and displace those $[Fe^{3+}]_{TET}$ ions to octahedral positions[11]. Therefore, the occupancy of the octahedral sites will be reserved for ferrimagnetic Ni^{2+} and Fe^{3+} ions (higher magnetic moment than Cu^{2+}) and the M_S value of the ferrite will be enhanced in accordance to the magnetic moment of the octahedral sublattice ($\eta_B = \eta_{OCT} - \eta_{TET}$). When the concentration of Cu^{2+} is increased further, e.g. $x > 0.5$, a change in the type of substitution occurs: Cu^{2+} ions now tend to occupy octahedral sites, displacing the $[Fe^{3+}]_{OCT}$ ions to tetrahedral sites, hence the decrease observed in the M_S value[4].

I.1.2 $Ni_{0.5}Cu_{0.5}Fe_2O_4$: Effects of the annealing temperature

The $Ni_{0.5}Cu_{0.5}Fe_2O_4$ ferrite showed the highest saturation magnetization, e.g. higher Snoek's limit[12], therefore, it was selected for further analysis regarding the role of the silica hard template. For this purpose, an additional $Ni_{0.5}Cu_{0.5}Fe_2O_4$ sample was analogously prepared and annealed at 900 $°C$. The XRD patterns of both silica-$Ni_{0.5}Cu_{0.5}Fe_2O_4$ hybrids (annealed at 700 and 900 $°C$) are shown in Figure 3.3. In both cases, the peaks corresponding to the ferrite and the silica phases are observed.

Diffraction peaks became sharper with temperature, suggesting a higher crystallization degree without structural changes in the spinel.

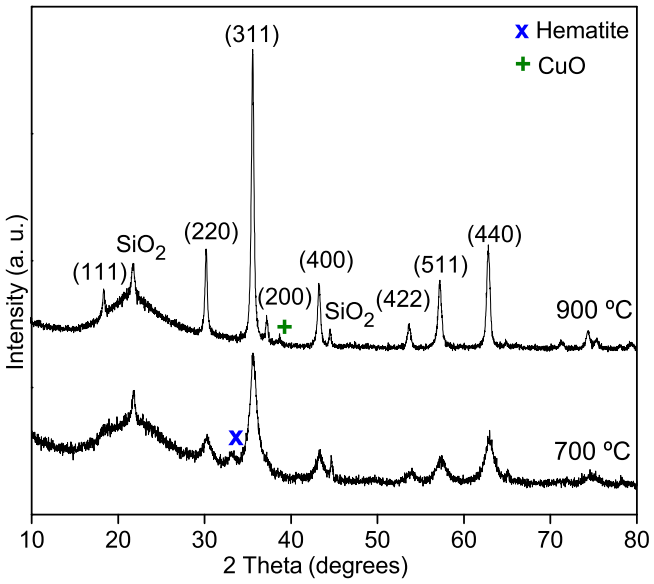

FIGURE 3.3: X-Ray diffraction patterns of the ferrite-silica hybrids annealed at 700 (bottom) and 900 $°C$ (top)

The crystallite size of samples annealed at 700 and 900 $°C$ was 8.6 and 23.8 nm, respectively. The increase of crystal size with temperature could be a consequence of the enhanced diffusion at high temperatures and due to slight changes in the pore structure of the template when treated at 900 $°C$[13,14]. Indeed, the small hematite impurity that was observed in the 700 $°C$ annealed $Ni_{0.5}Cu_{0.5}Fe_2O_4$ sample, is not longer seen when annealed at 900 $°C$, which corroborates that diffusion is promoted with temperature. Instead, a very weak peak that corresponds to CuO is observed. This indicates that the stoichiometry of ferrites is slightly altered with the thermal treatment: segregation of small quantities of hematite or CuO occurs for lower (700 $°C$) or higher temperatures (900 $°C$), respectively.

For transmission electron microscopy images (TEM, Figure 3.4, a and b) both samples

were subjected to detemplation with NaOH to check their morphology with a better contrast. Size distributions in TEM images (Figure 3.4 c and d) were determined in both cases by measuring the diameter of more than 190 particles. As expected from the previous XDR observations, when annealing is done at 700 $°C$, a narrow particle size distribution with an average diameter of 8.3±1.6 nm is obtained; at 900 $°C$, the particles show a broader and less symmetric particle size distribution, with diameters ranging from 15 to 80 nm.

To ensure the preservation of nanoparticles after the basic treatment, selected area electron diffraction patterns (SAED, Figure 3.4 e and f) were recorded and contrasted to the XRD patterns acquired before detemplation. The SAED of both samples is well in accordance with the XRD results: rings 1, 2, 3 and 4 correspond to the (111), (220), (311) and (400) diffraction planes, respectively, and can be correlated with the typical diffraction rings observed for spinel structures. This corroborates that no structural or morphological changes occurred in the samples upon the treatment with NaOH.

The distribution of the ferrite nanoparticles inside the silica template was evaluated by contrasting the nitrogen adsorption-desorption isotherms of the pristine silica and the ferrite-silica hybrids (Figure 3.5). All the curves showed the typical hysteresis loop of mesoporous materials (type IV isotherm) where the closure at $P/P_0 \sim 0.4$ indicates the presence of small mesopores.

No steep changes in the adsorption behavior were observed at low relative pressures, indicating the absence of micropores. This observation was confirmed by using the t-plot method for the specific surface area of micropores. The surface area, total pore volume and diameter of all the prepared materials are shown in Table 3.2. For comparison purposes, the corresponding data of silica without any ferrite loading is also shown (annealed at 700 and 900 $°C$).

The surface area sharply decreases when the neat silica is loaded with ferrite nanoparticles, thus proving the filling of the pores. However a decrease of surface area occurs, solely upon the thermal treatment. Silica might undergo densification above 650 $°C$[15]

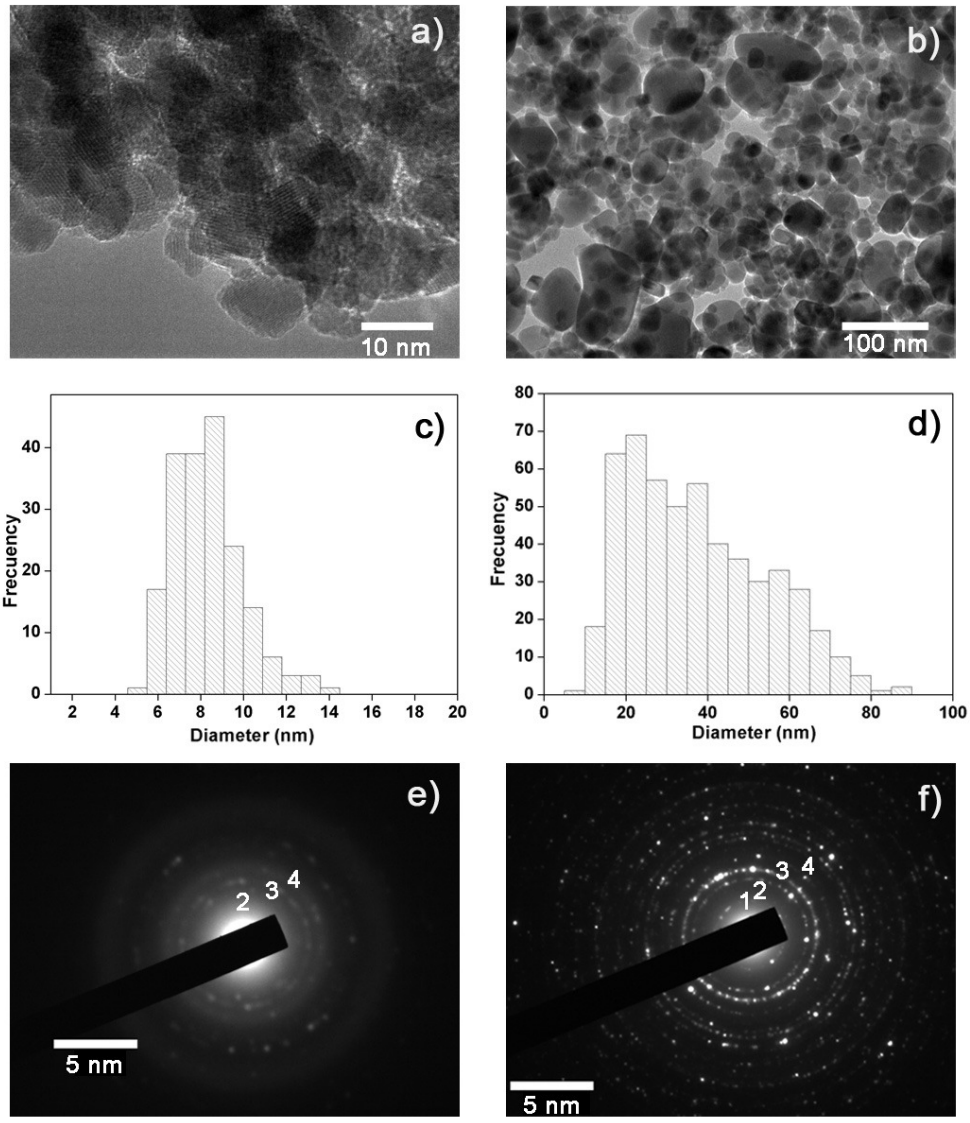

FIGURE 3.4: TEM images of the detemplated ferrite nanoparticles: (a) annealed at 700 $°C$ and (c) corresponding size distribution and (b) annealed at 900 $°C$ and (d) corresponding size distribution. Selected area electron diffraction patterns (SAED) for both ferrites: (e) annealed at 700 and (f) at 900 $°C$

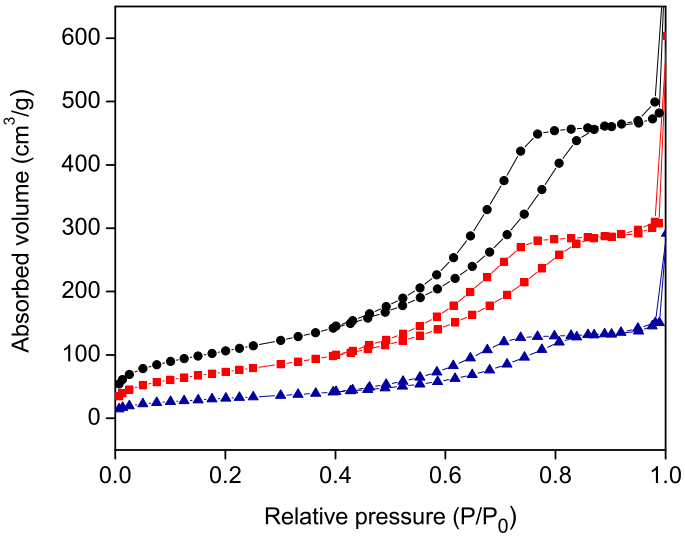

FIGURE 3.5: Nitrogen adsorption-desorption isotherms of: neat silica (●) and ferrite-silica hybrids annealed at 700 (■) and 900 $°C$ (▲)

TABLE 3.2: Surface area, total pore volume and pore diameters (Φ_{pore}) obtained from the adsorption isotherms of the silica control samples (neat silica, and silica annealed at 700 and 900 $°C$) and of the ferrite-silica hybrids (annealed at 700 and 900 $°C$)

Sample	**Surface area,** $\boldsymbol{m^2 \cdot g^{-1}}$	**Total pore volume,** $\boldsymbol{cm^3 \cdot g^{-1}}$ [a]	$\boldsymbol{\Phi_{pore}}$, nm [b]
Neat Silica	385.12	0.722	6.2
Silica 700 $°C$	367.68	0.648	6.1
Silica 900 $°C$	240.63	0.411	5.8
Ferrite-Silica (700 $°C$)	269.34	0.451	5.9
Ferrite-Silica (900 $°C$)	114.77	0.222	5.8

[a] Calculated according BET theory
[b] Calculated using the BJH approach

due to condensation of silanol groups from different particles or by the rearrangement of primary particles in a denser array [16]. This effect is more significant when annealing is done at the highest temperature (900 $°C$), where a reduction of a 38% in the surface area is observed.

Regarding the total pore volume and the pore diameter, the synthesis of non-porous

inclusions within silica, reduces its porosity and also the pore size slightly. This indicates that the ferrite particles are bulky and block (at least partially) some of the pores of the silica, as observed for other guest particles grown within porous templates [17]. However, the small reduction of the pore diameter when compared to the surface area or total pore volume may indicate a non-homogenous filling of the pores [18].

As shown in Figure 3.6, the recorded values of coercitivity, remanence and saturation magnetization are 10 Oe, 0.06 $emu \cdot g^{-1}$ and 4.06 $emu \cdot g^{-1}$, respectively, for the sample annealed at 700 $^{\circ}C$, and 86 Oe, 1.27 $emu \cdot g^{-1}$ and 7.47 $emu \cdot g^{-1}$, respectively, for the sample annealed at 900 $^{\circ}C$. These values suggest that the treatment at 700 $^{\circ}C$ induces the growth of the ferrite nanoparticles inside the silica pores as individual monodomains, since the material shows a nealy superparamagnetic behavior.

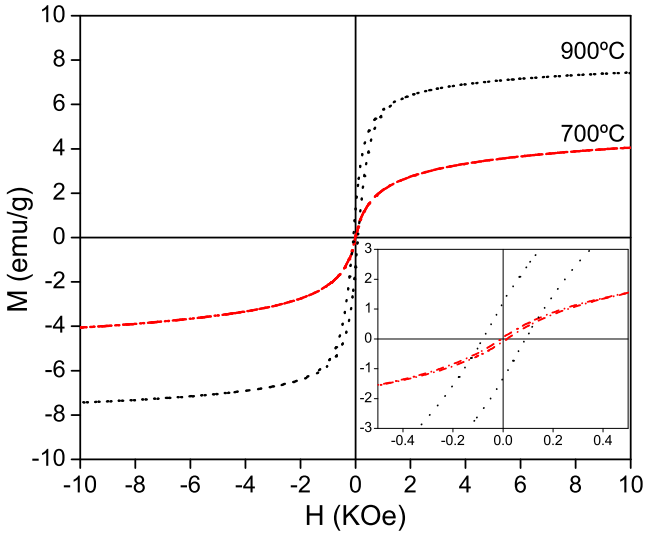

FIGURE 3.6: Hysteresis loops of the ferrite-silica hybrids annealed at 700 and 900 $^{\circ}C$. Inset: near-zero zoom view for both hysteresis loops showing the increase of coercitivity (x-axis intersection, H_C) and remanence (y-axis intersection,M_R) when the annealing temperature increases

In contrast, annealing at 900 $^{\circ}C$ seems to provoke higher hysteresis losses than when annealed at 700 $^{\circ}C$, and this can be attributed to the particle size growth [19]. With

regard to the saturation magnetization, particles annealed at 700 $^{\circ}C$ present a lower value. This is likely due to their smaller size, as the surface-to-volume ratio is higher for small particles than for larger ones. Atoms at the surface of the particles show a different local order than those of the core, resulting in lower magnetic moments for smaller particles (surface spin canting effect) [20], which have a higher fraction of surface atoms that do not contribute to the net magnetization value [21].

It is worthy to note that both types of particles (prepared at 700 and 900 $^{\circ}C$) were clearly attracted by a magnet, even though the calculated concentration of ferrite nanoparticles in the template is $\sim$ 23 $wt\%$. Taking into account the proportion of magnetic constituent in the non-magnetic silica material, the saturation magnetizations herein reported are in well agreement with reported values for bulk $Ni_{0.5}Cu_{0.5}Fe_2O_4$ [4].

I.2 MAGNETITE ADSORBED ONTO CARBON NANOFIBERS

The high surface area of carbon nanofibers (CNFs) enabled them to adsorb preformed oleic acid capped-magnetite nanoparticles and become remarkably responsive to an external magnet. The resulting material shows a combination of electric and magnetic properties that is highly relevant for many applications [22]. The basic characteristics and morphology of these hybrids are discussed throughout this section.

I.2.1 Magnetite nanoparticle synthesis and adsorption on CNFs

Magnetite nanoparticles were synthesized by a coprecipitation protocol in the presence of oleic acid to avoid agglomeration [23]. TEM imaging (Figure 3.7) showed individual particles with a narrow size distribution centered at 9.4 nm.

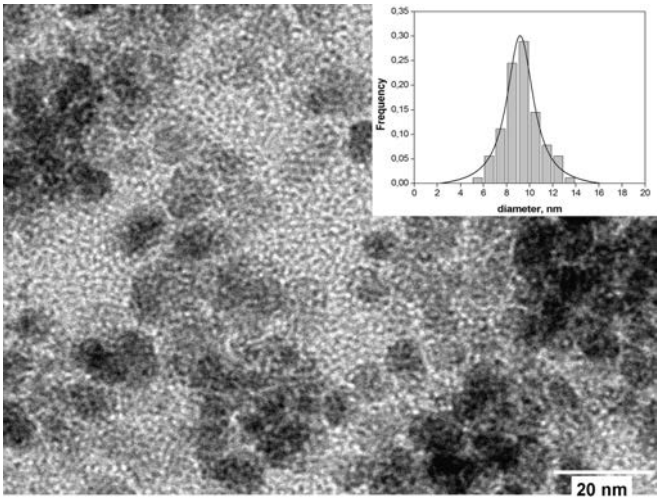

FIGURE 3.7: TEM image of the oleic acid capped magnetite nanoparticles showing in the inset the particle diameter distribution (courtesy of M.G. González *et al.*) [23]

The oleic acid-capped magnetite nanoparticles were adsorbed onto the surface of CNFs by simply placing both materials under sonication in heptane. The morphology of CNFs, before and after decoration with magnetite, is shown in Figure 3.8. Pristine CNFs show a wide size distribution and a large variety of shapes, while CNFs/Mag show a non-uniform coverage of magnetite.

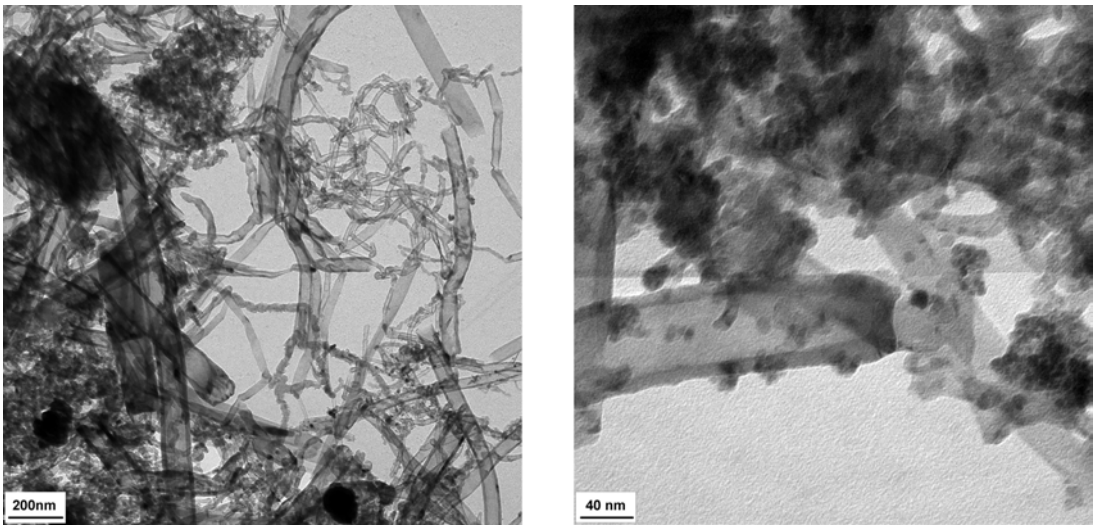

FIGURE 3.8: TEM of Pristine CNF (left) and CNF/Mag (right)

Powder XRD of the CNF/Mag sample (Figure 3.9) was recorded to confirm the preservation of the original crystalline structure from both the as-prepared magnetite nanoparticles and the pristine CNFs. The XRD pattern of CNFs shows two intense peaks at scattering angles of 26.1 and 44.25, which can be indexed as the (002) and (101) planes of the hexagonal graphite lattice, respectively. These peaks remain unmodified in the CNF/Mag material. Nanoparticles show a typical spinel-like structure, which is evidenced by the signals at 30.2, 35.6, 43.5, 53.8, 57.4 and 63.0 that can be attributed to the (220), (311), (400), (422), (511) and (440) crystalline planes of magnetite, respectively. In addition, the size of the particles (9.4 nm, through equation Equation 2.4) was consistent with that obtained by TEM (Figure 3.7). Neither other phases (such as hematite) nor changes in the diffraction pattern were observed. This indicates that after the incorporation of the nanoparticles onto the fibers, the crystalline structure of both constituents remains unaltered. VSM results for the magnetite nanoparticles and for CNF/Mag are shown in Figure 3.10. The lack of hysteresis in both cases can be attributed to the superparamagnetic nature of the fine magnetite particles. The saturation magnetization for CNF/Mag decreases slightly in comparison to that of the magnetite nanoparticles due to the non-magnetic nature of CNFs.

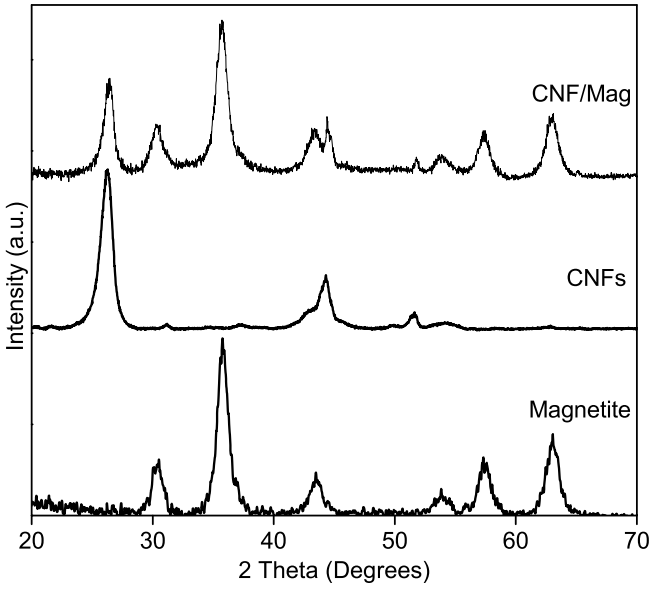

FIGURE 3.9: XRD patterns of magnetite nanoparticles, pristine CNFs and CNF/Mag

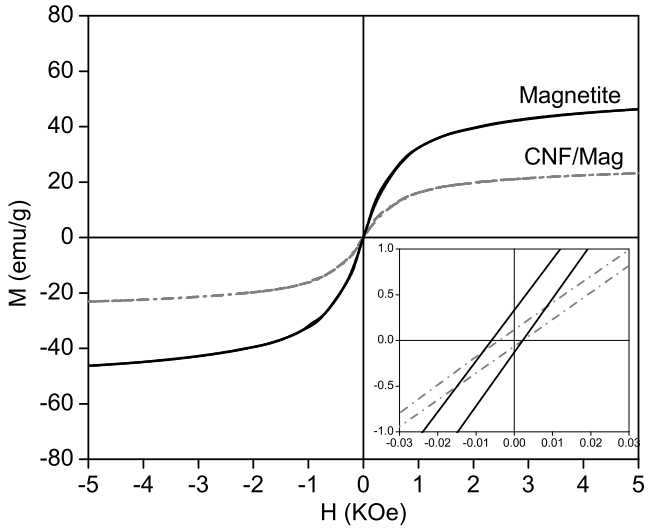

FIGURE 3.10: Hysteresis loops for the magnetite nanoparticles (solid) and for the CNF/Mag (dash-dot). Inset: Near-zero zoom view

I.3 CARBON NANOTUBE AND MAGNETITE-DECORATED CARBON NANOTUBE SCAFFOLDS

Aerogels of well interconnected carbon nanotubes (CNTs) are highly desirable, since these materials can show enhanced bulk electrical conductivities at limited weight fractions. In this context, freeze-drying is a suitable technique for their preparation. When aqueous dispersions of CNTs (and a polymer binder) are unidirectionally frozen at controlled rates of immersion in a cryogenic liquid, the watery fraction is transformed into solid ice columns. The CNTs that were initially dispersed in liquid water, are expelled to the ice-crystal grain boundaries and accumulate around them forming the solid cryogel. If subjected to freeze-drying, ice sublimates, leaving behind large empty areas between the regions of solute buildup. This process allows for the preparation of porous CNT monoliths (scaffolds), with a highly percolated and well-defined microstructure (Figure 3.11 a and b).

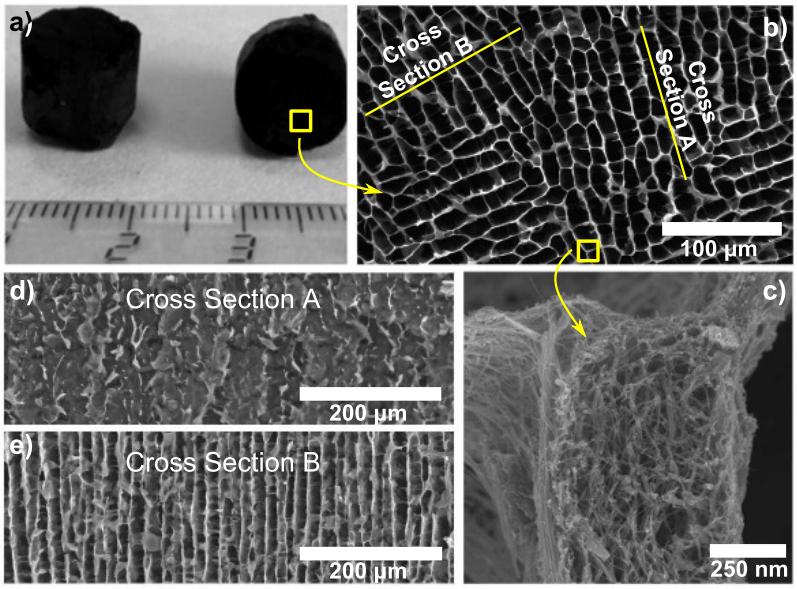

FIGURE 3.11: General morphology of CNT scaffolds: (a) *cm*-scale scaffold. (b) Transversal-section of the scaffold showing the micro-channels of its structure. (d) and (e) Longitudinal-sections of the scaffold (taken from the marked cross-sections in b). (c) Walls of the scaffold formed by closely packed and randomly arranged CNTs

As ice columns grow, they squeeze CNTs, which are then forced to occupy only certain small volumes along the whole longitude of the scaffold (Figure 3.11 c and d). Therefore, these macrostructures can present high longitudinal interconnectivity at low CNT loads. This section will discuss how morphology and properties of these assemblies vary as a function of their building block CNTs.

I.3.1 Building blocks: CNTs and magnetite decorated CNTs

CNTs used for the preparation of 3D-scaffolds are nitrogen doped MWCNTs (CNxNTs). Although the surface of CNxNTs resembles the one observed for CVD-grown MWCNTs without any doping, their morphological peculiarity resides on the bamboo-like inner structure that they present (Figure 3.12).

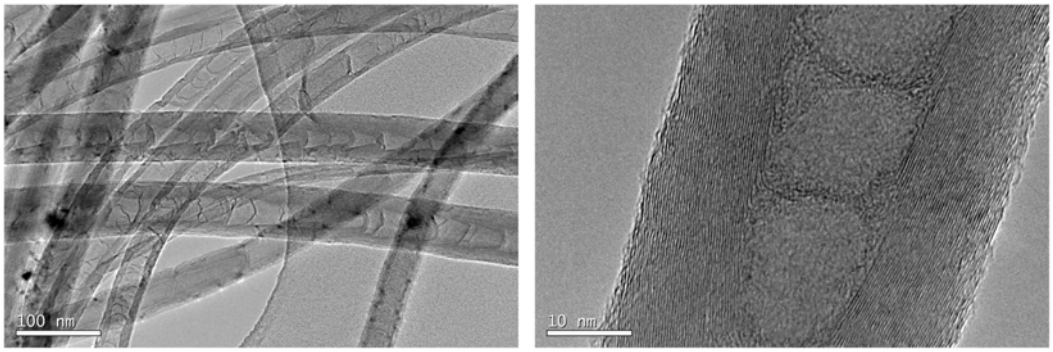

FIGURE 3.12: TEM images of the multiwalled pristine CNxNTs ($\sim 50\ nm$ diameter), exhibiting the typical bamboo-like inner structure

Introduction of heteroatoms in the nanotube's lattice increases their surface reactivity, and this might enable the selective CNxNT decoration with a variety of nanoparticles[24]. In our case however, decoration of pristine CNxNTs with magnetite nanoparticles[5] was uneven (Figure 3.13 a). Particles were agglomerated at certain regions, probably where there is a higher concentration of N-defects in the graphitic lattice[25].

[5]Non-oxidized CNxNTs were decorated by V. Gehová ,who also produced complementary amounts of CNxNTs for characterization, as a part of a collaborative work.

To improve the decoration with magnetite, CNxNTs were oxidized through a standard sulpho-nitric acid treatment prior to decoration.

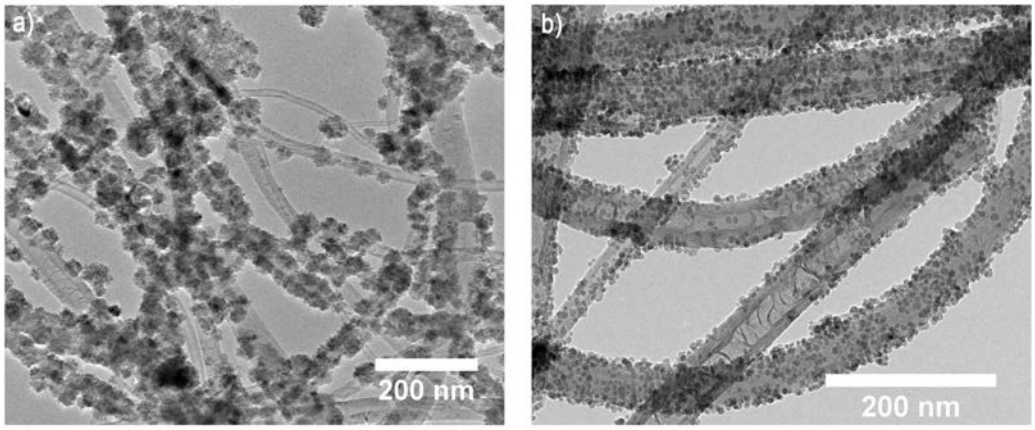

FIGURE 3.13: TEM images of the magnetite-decorated CNTs: a) pristine CNxNTs and b) oxidized CNxNTs

As seen in Figure 3.13 b, magnetite nanoparticles are more homogeneous (shape and size $\sim 7.8\ nm$) and densely arranged over oxidized CNxNTs. Acidic sites are normally considered useful as anchoring points of chemical precursors, therefore, an increased number of acidic moieties in the surface of oxidized CNxNTs could be responsible of the better magnetite decoration. Titration confirmed concentrations of acidic groups of 8.6×10^{-5} and 4.7×10^{-4} (in $mmol\cdot mg^{-1}$ of nanotubes) for the pristine and oxidized CNxNTs, respectively.

Another cause for the denser nanoparticle decoration on oxidized CNTs could be an increased number of lattice defects on their surface, since these can contribute to stabilize and anchor the chemical precursors of the nanoparticles [26]. Raman spectroscopy of both pristine and oxidized CNxNTs (Figure 3.14) revealed the typical D- and G-bands located at 1345-1350 and 1579 cm^{-1}, respectively, which are associated to the disorder degree within sp^2 hybridized carbon structures (D-band), and the tangential mode of the sp^2 carbon hexagonal lattice (G-band). Oxidized CNxNTs present a higher intensity ratio between D- and G-bands, confirming an increased number of defects in their lattice [27].

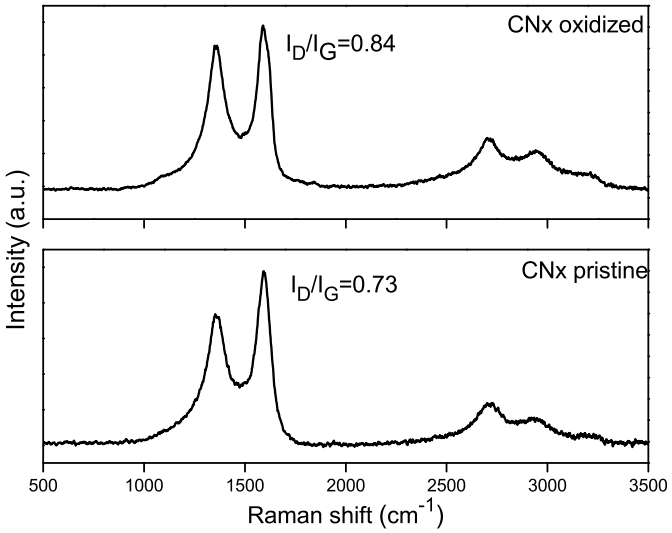

FIGURE 3.14: Raman spectra of oxidized and pristine CNxNTs confirming that the oxidation treatment leads to a higher proportion of defects (higher I_D/I_G ratio) in the graphitic lattice

With regard to the oxidized and decorated CNxNTs (CNxMag), the XRD pattern (Figure 3.15 a) shows the diffraction signals of both the spinel and graphite phases. The average particle size of the magnetite nanoparticles (7.8 nm, through equation Equation 2.4) is consistent with that determined through TEM (Figure 3.13 b) and in addition, the Raman spectrum (Figure 3.15 b) allows for the unambiguous discernment of the magnetite's nature, since the characteristic lines of maghemite (between 200 and 800 cm^{-1}) are not observable.

To determine the content of magnetite in the CNxMag nanotubes, the material was subjected to TGA (Figure 3.16) and the residual mass at 900 $°C$ (M_R) was analyzed (Table 3.4). Results showed a residue of 30 $wt\%$ for the CNxMag sample, while for the non-decorated CNxNTs, the M_R corresponds to only a 5 and 4 $wt\%$ for the pristine and oxidized CNTxNTs, respectively. This observation corroborates the high degree of magnetite decoration attained in the CNxMag nanotubes.

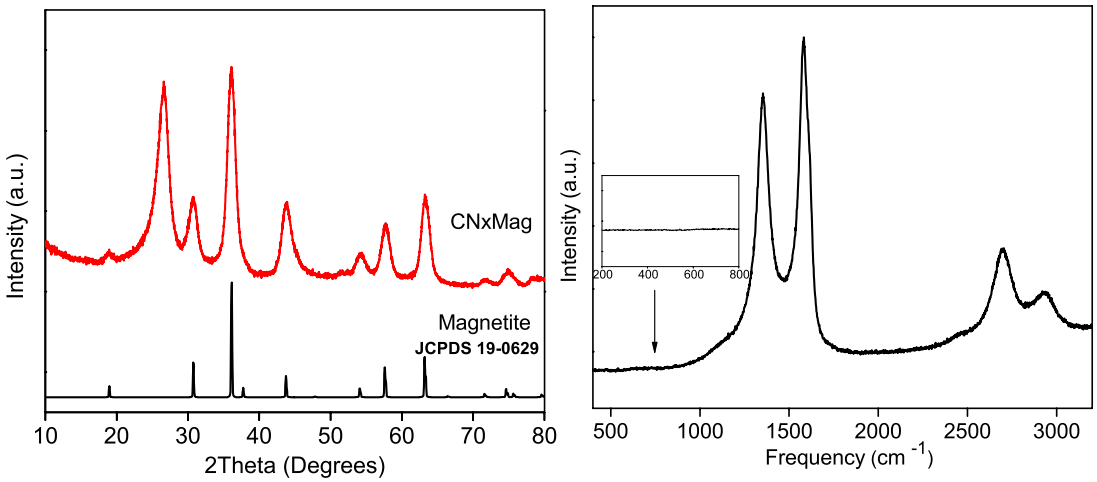

FIGURE 3.15: a)Comparison of the magnetite-decorated CNxNTs (CNxMag) XRD with that of a JCPDS pattern of magnetite. b) Raman spectrum of CNxMag (Inset: zoom-view of the 200-800 cm^{-1} zone)

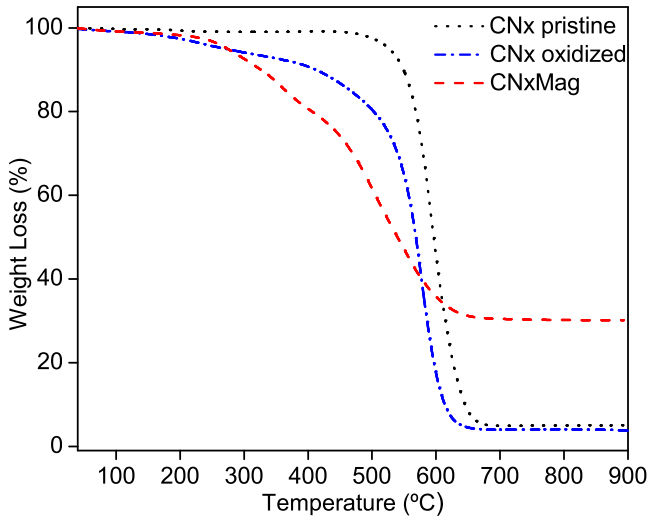

FIGURE 3.16: TGA comparison between prisine CNxNTs, oxidized CNxNTs and magnetite decorated CNxNTs (CNxMag) showing the evident higher residual mass and lower thermal stability of the CNxMag nanotubes

CNxMag nanotubes present two broad and overlapped weight losses. The first loss, between 200 and 350 $°C$, is attributed to residual triethyleneglycol (TREG, capping agent used during the growth of magnetite nanoparticles) and the second, between 400 and 650 $°C$, to the degradation of CNTs. The maximal degradation rate (T_m), corresponding to this ultimate step, is lower than that of oxidized and pristine CNxNTs (results are summarized in Table 3.3). CNxMag nanotubes might show a lower T_m as a consequence of the overlapped degradation of TREG and CNTs, however, since magnetite has a low resistance to changes in temperature, nanoparticles attached over the nanotube's surface could also contribute to accelerate the thermal degradation of CNxNTs at some extent.

TABLE 3.3: Residual mass ($M_{R\%}$) and maximal degradation rate (derivative,T_M) of pristine CNxNTs , oxidized CNxNTs and magnetite-decorated CNxNTs

	pristine	**oxidized**	**CNxMag**
$\boldsymbol{M_{R\%}}$	5	4	30
$\boldsymbol{T_M,°C}$	591	577	543

In the case of oxidized tubes, their lower thermal stability in comparison to pristine tubes can be attributed to the higher number of defects in their structure, since these can favor the nanotube's reactivity towards O_2, causing a downshift in their T_m.

In accordance to the size of the magnetite nanoparticles determined through TEM and XRD, and their proportion over the nanotube's surface, VSM (Figure 3.17) confirmed that CNxMag nanotubes are superparamagnetic at room temperature and thereby, they show nearly no coercive or remanent losses.

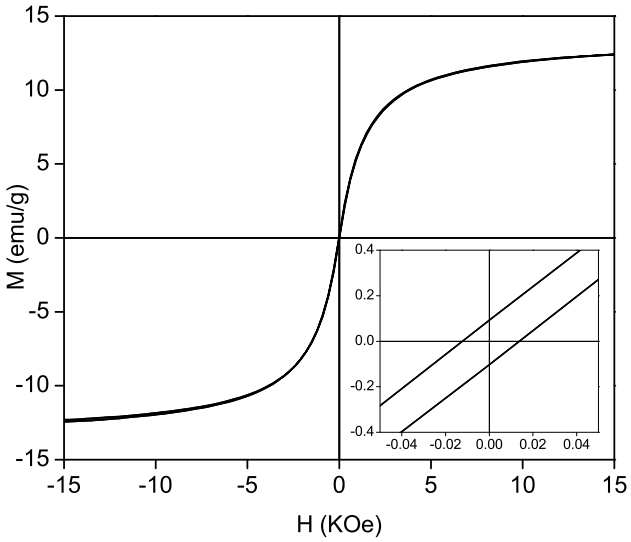

FIGURE 3.17: Hysteresis loop of the CNxMag nanotubes obtained from VSM. Inset: near-zero zoom view of the loop, showing the negligible values of coercitivity and remanence

I.3.2 Morphology of scaffolds

All scaffolds were prepared from primary aqueous solutions of chitosan (CHI, 1 $wt\%$) and different concentrations of magnetite-decorated CNxNTs or non-decorated, but oxidized, CNxNTs[6]. Scaffolds of oxidized CNxCNTs were prepared in concentrations of 3.4 and 6.7 $wt\%$ and were labeled as C3 and C6, respectively. Scaffolds of magnetite-decorated CNxNTs (CNxMag), were prepared using the same concentrations mentioned above and were named accordingly as CM3 and CM6.

SEM images of the transversal sections of both types of scaffolds are presented in Figure 3.19 and Figure 3.18. All samples show an open cellular-like structure of elongated pores (void fraction, in black) with dimensions between 20 and 30 μm. CNxNTs are distributed and closely packed within the lamellar channels' walls (bright regions).

[6]Scaffolds were produced by S. Nardecchia as a part of a collaborative research project.

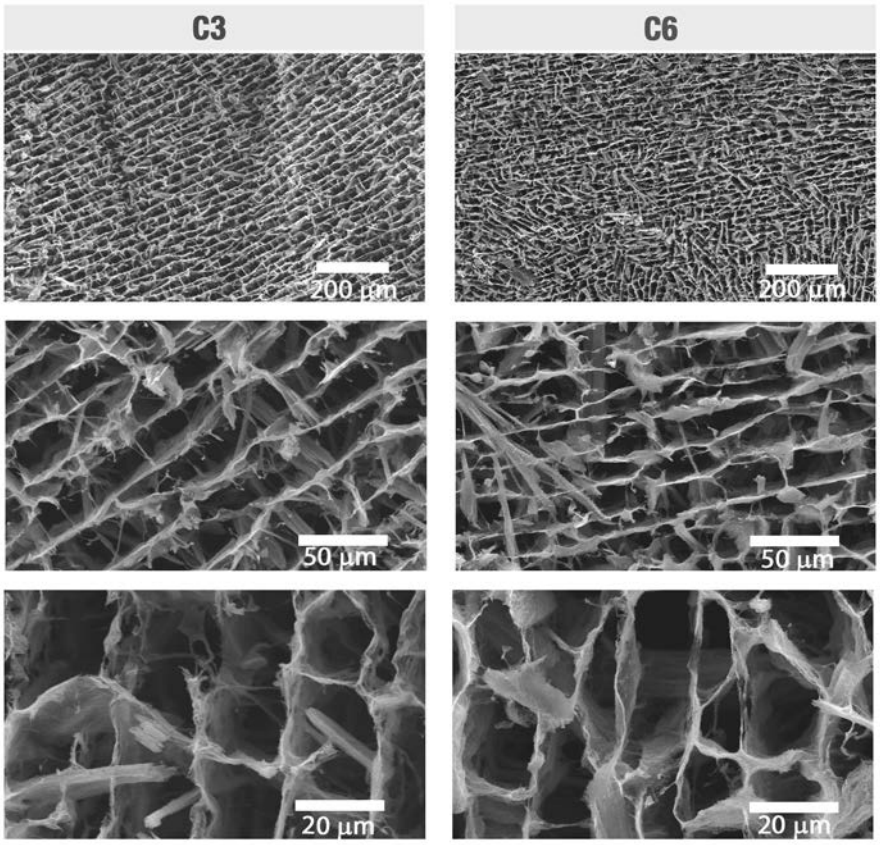

FIGURE 3.18: SEM images of C3 (left col.) and C6 (right col.) scaffolds at different magnifications

Since all the samples were frozen with the same immersion rate, morphological differences are expected solely from the specific characteristics of the CNxNTs used in each case, e.g. concentration and dispersion degree attained in the primary water-based dispersions.

Concerning to the concentration, in both types of scaffolds (with decorated and non-decorated CNxNTs) walls are somehow thickened with the $wt\%$ of nanotubes ($C6 > C3$ and $CM6 > CM3$) and the lamellar distance is decreased. At first glance, the void fraction seems to decrease in the same extent however, for C3 and C6 the thickness

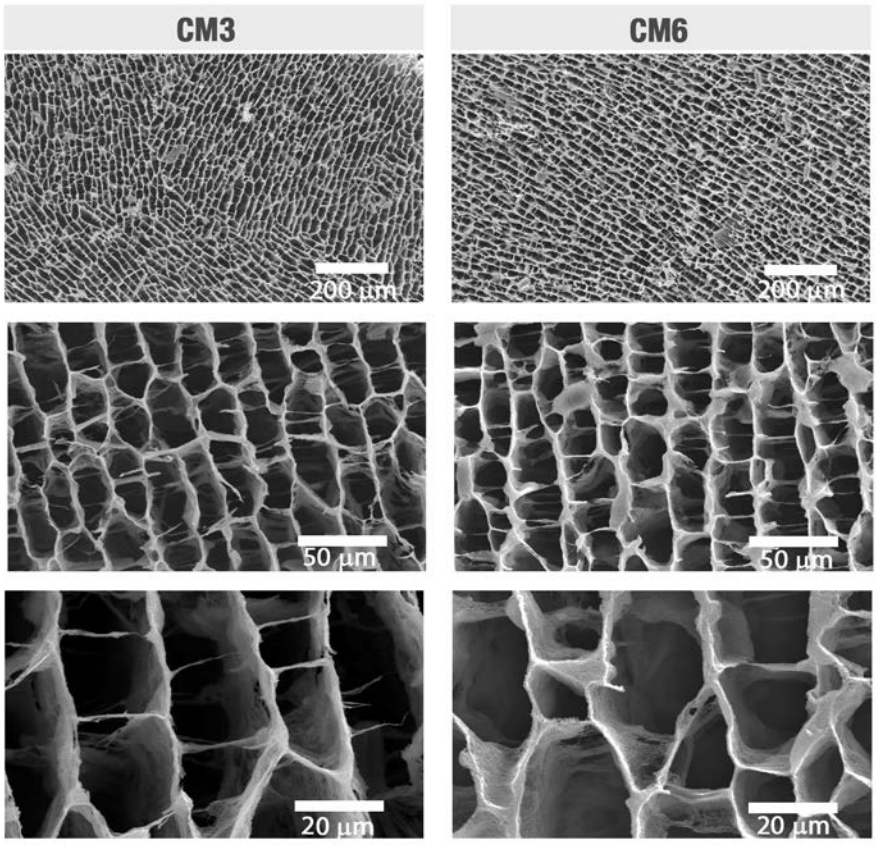

FIGURE 3.19: SEM images of CM3 (left col.) and CM6 (right col.) scaffolds at different magnifications

swell is not so evident, since both scaffolds present CNxNT chunks. These are not forming part of the walls of scaffolds and do not contribute to their thickness.

With regard to the dispersion degree, its effect can be clearly seen in the geometry and order of the walls. Both C3 and C6 present a less ordered structure than CM3 and CM6, respectively. The ice's crystal morphology depends upon the equilibrium of adsorption/desorption of water at the solute interface when frozen. Therefore, the different morphology might be attributed to the greater net amount of high-surface-area nanotubes in C3 and C6, in comparison to their magnetite-decorated analogues. Indeed, above certain concentration, the primary aqueous dispersions of C3 and C6

were extremely viscous, which may have impede the proper dispersion of CNTs. This insufficient CNT disaggregation can be traduced in a more defective scaffold's structure for C3 and C6, since the CNT bundles would hinder the assembly of the structure. In addition, the slightly acidic pHs of the CHI solutions and the presence of adsorbed TREG on the magnetite nanoparticles, as a consequence of the synthesis procedure, could have also contributed to favor the dispersion of the decorated-CNxNTs. TREG can act as a surfactant, while surface groups on the magnetite nanoparticles are more prone to interparticle repulsion at acidic pHs.

In order to compare the macroporosity differences, image analysis was done to estimate the percentage of void area in each scaffold (void area fraction/total area of the image in %). Void areas from at least 10 SEM images were measured and averaged to retrieve the void area percentages shown in Figure 3.20, where representative binary images are also included. The void area is represented by the black fraction, meanwhile, those areas occupied by nanotubes in the scaffold walls, appear in white.

Results corroborate that scaffolds with lower nanotube contents (C3 and C6) have higher void areas. Additionally, C3 and C6 consistently show lower void areas than CM3 and CM6, respectively, well in agreement with the poorer dispersion attained with non-decorated CNxNTs.

Although calculated void fractions can be used to estimate the porosity of scaffolds, micro and mesoporosity are being neglected, since they cannot be extracted from SEM images. The apparent density of scaffolds (weight/volume) was measured to verify the image analysis results (Figure 3.20). Density clearly increases as the concentration of decorated and non-decorated CNxNTs increases. The extreme low densities of all samples ($\sim$ 0.04 - 0.07 $g \cdot cm^{-3}$) disables us to determine if the density differences between scaffolds having equivalent nanotube concentrations are genuine, or if they arise due to the experimental uncertainty. Nonetheless, the measured values are in accordance with the trends extracted from the image analysis.

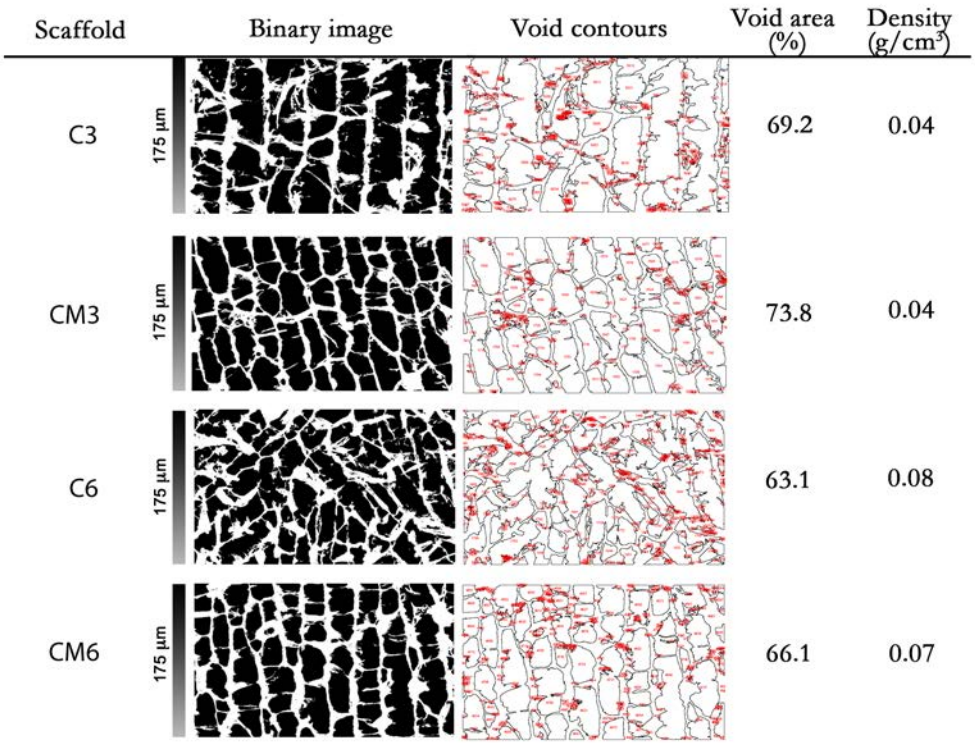

FIGURE 3.20: Representative binary SEM images and resultant void contours used for calculating the void area % of each scaffold through image analysis. The automatic numbering of void areas generated by the software appears in red. The apparent density of each scaffold (weight/volume) is also included

I.3.3 Composition of scaffolds

TGA curves (Figure 3.21) were recorded to determine the thermal stability and composition of scaffolds. Due to the presence of organic species (CHI and TREG, in the case of CNxMag) all curves show several overlapped weight losses within the swept temperature range. Degradation processes occurring between 200 and 400 $°C$ can be attributed to CHI and TREG, while those between 400 and 700 $°C$ correspond to the degradation of CNTs. As summarized in Table 3.4, within both temperature intervals, the maximal degradation rates (peaks of the TGA derivatives) of CM3 and CM6 are

lower than those of C3 and C6, respectively, tendency which was also observed when the original CNxMag nanotubes were compared to the non-decorated CNxNTs.

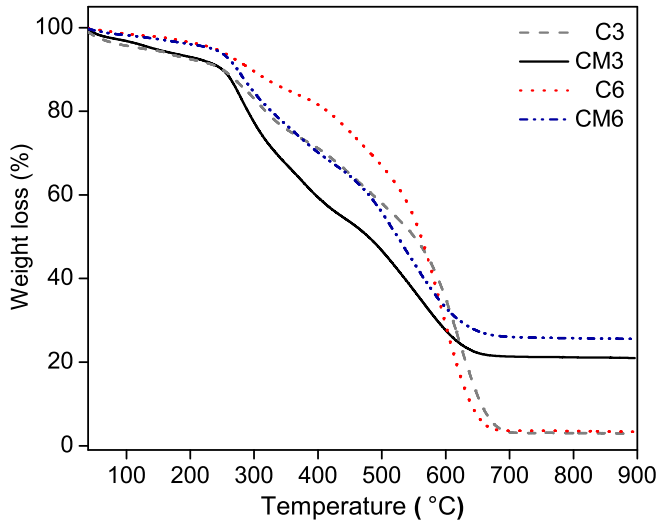

FIGURE 3.21: TGA curves of scaffolds with varying concentrations of magnetite-decorated CNxNTs (CM3 and CM6) and non-decorated CNxNTs (C3 and C6)

Regarding CNxNTs and CNxMag, the residual mass obtained from the thermograms was employed to determine their amount in each scaffold. Since the original magnetite-decorated nanotubes (CNxMag) contain a 30 $wt\%$ of iron species (as previously shown in Table 3.3), the content of CNxMag in scaffolds prepared with decorated CNTs (CM3 and CM6) was recalculated through the residual mass obtained from the thermograms. In the case of C3 and C6, the content of CNxNTs was assessed through the same consideration but accounting that non-decorated CNxNTs leave a residue (from the CVD catalyst) of 4 $wt\%$. For C6 and CM6, the theoretical content of nanotubes should be around 87 $wt\%$, as the final scaffold is composed only by nanotubes (decorated or non-decorated) and CHI, while for C3 and CM3 it should be 77 $wt\%$. As shown in Table 3.4, the calculated content of nanotubes in each scaffold (filler: CNxNTs or CNxMag), gives a systematic difference of 1-6 $wt\%$ from the theoretical value, which coincides with the weight loss of all samples below 200 $°C$. Therefore, this difference

can be attributed to acetic acid traces, as CHI is dissolved in slightly acidic water, and to the water uptake ability of the extreme hygroscopic CHI.

TABLE 3.4: Scaffold's TGA residual mass ($M_{R\%}$), calculated filler $wt\%$ accounting the obtained $M_{R\%}$, and maximal degradation rates (derivative peaks, T_m) observed within 200 − 400 $°C$ ($T_{m200-400}$) and 400−700 $°C$ ($T_{m200-400}$)

	$M_{R\%}$	filler, $wt\%$	$T_{m\ 200-400},\ °C$	$T_{m\ 400-700},\ °C$
C3	3	75.3	308	622
CM3	21.3	71	279	552
C6	3.4	85	296	592
CM6	25.6	85.3	279	535

I.3.4 Additional post-treatment

CM6 was subjected to a thermal treatment at 360 $°C$ under nitrogen and the resulting scaffold was labeled as CM6T. As will be discussed in part II, this step was done to convert the CHI binder into carbon, therefore, to improve the interconnection between adjacent nanotubes. The morphology of the material before and after the thermal treatment is shown in Figure 3.22. SEM images show that the channel structure was conserved upon the treatment. Although difficult to discriminate through TEM images (Figure 3.22 c and d), in the CM6T sample it is observed an amorphous halo only nearby the surface of the CNTs, meanwhile, in the CM6 sample, this coverage is seen within most intersections between adjacent CNTs.

To corroborate the partial carbonization of the polymeric fraction of the scaffold through the thermal treatment, samples CM6 and CM6T were compared through TGA (Figure 3.23). As can be seen, the maximal degradation temperature clearly increases for the CM6T sample. In addition, below 400 $°C$ the weight loss of CM6T is minimal in comparison to CM6, suggesting that the organic fraction (in CM6) has been transformed, at least at some extent, into amorphous carbon (in CM6T) upon the thermal treatment.

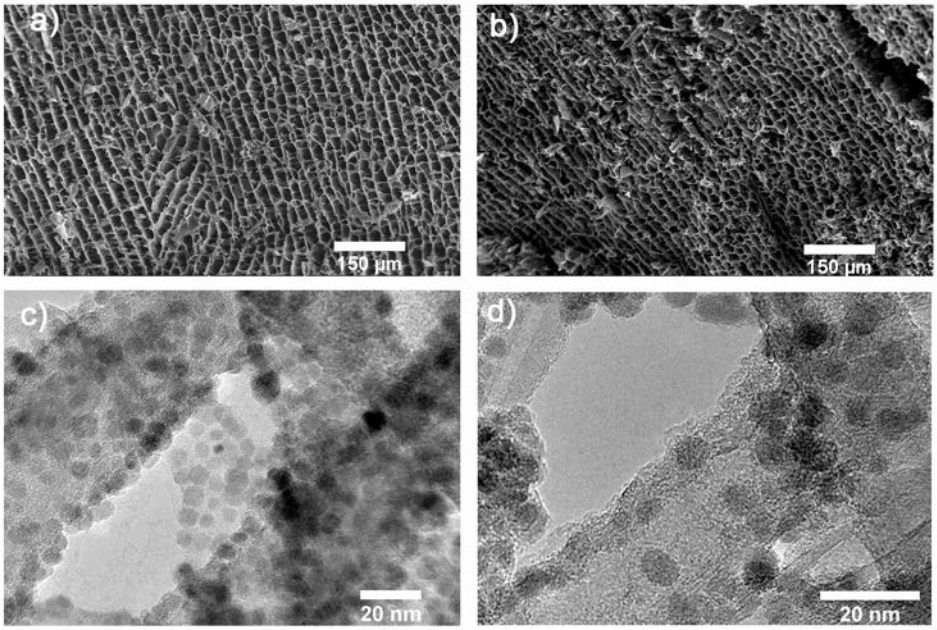

FIGURE 3.22: (a) and (c) CM6 scaffold before the thermal treatment (SEM and TEM images, respectively). (b) and (d) Resulting CM6T scaffold after the thermal treatment of CM6 (SEM and TEM images, respectively)

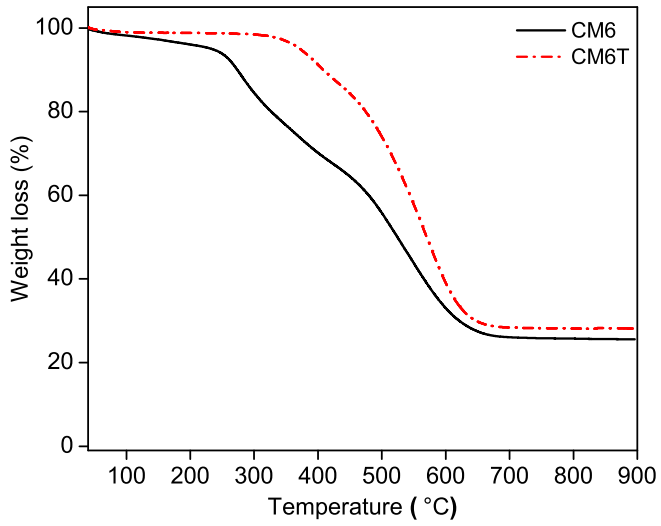

FIGURE 3.23: TGA comparison of samples CM6 (6.7 *wt*% CNxNTs scaffold before thermal treatment) and CM6T (6.7 *wt*% CNxNTs scaffold after thermal treatment)

I.4 CNT-SPONGES

CNT-sponges are highly porous, flexible, lightweight and conductive, as they are formed by entangled CNTs without insulating obstructions amongst them. CNT-interconnectivity should be better than in CNT-polymer composites and thereby, CNT-sponges could result very attractive for EMI shielding. The fabrication process of CNT-sponges is not limited by a low productivity, as it is for other CNT-assembled architectures, since these are synthesized by a one-pot chemical vapor deposition (CVD) method. Large-scale production could enable straightforward implementation of CNT-sponges in many technological fields[28,29].

The main properties and synthesis conditions for producing our CNT-sponges (first reported in 2010 by X. Gui *et al.*[30]) are analyzed below.

I.4.1 Synthesis and general characteristics

Carbon nanotube sponges were synthesized by liquid injection-CVD. Conditions are similar to those used for common nanotube synthesis but employing dichlorobenzene as carbon source. Unlike macrostructures of vertically aligned CNTs over substrates, CNT-sponges are macroscopic blocks of nanotubes that can be easily manipulated. Besides their lightweight, sponges are stretchable, bendable and mechanically tough, as shown in Figure 3.24.

As reported in the literature[31], the formation of CNT-sponges involves three growing stages (Figure 3.25), which can be modulated through the synthesis conditions. CNTs start growing from the fine catalyst seeds in the vapor phase (Figure 3.25 a). When the carrier gas sweeps them along the quartz tube, these CNTs (labeled as 1 and 2 in Figure 3.25) are deposited over the tube walls (or substrate). In the second stage (Figure 3.25 b), tubes 1 and 2 continue elongating, meanwhile newly formed CNTs deposit on top of them (labeled as 3 in Figure 3.25). Since these mechanisms occur repeatedly during the sponge growth, and as the catalyst particles inside open-ended

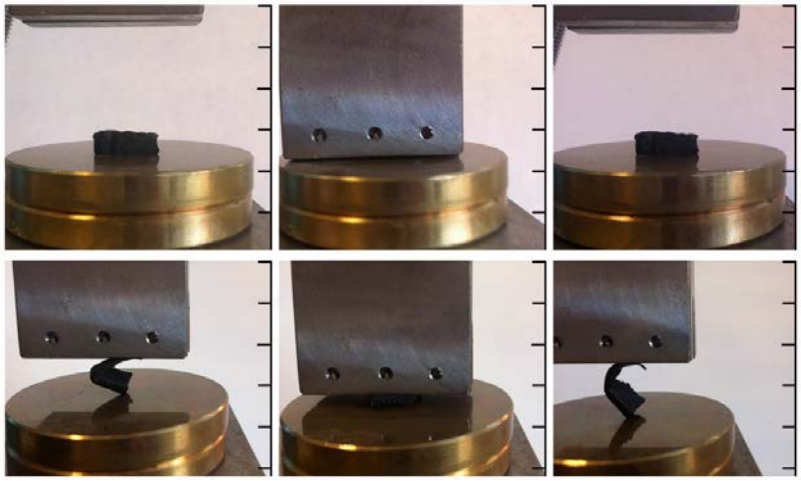

FIGURE 3.24: CNT-sponge subjected to compression (a) and bending (b), showing no structural damage after the process (scale bars: 1 cm)

tubes might be sucked to enable further CNT growth, the entanglement of CNTs becomes more probable (Figure 3.25 c). This entanglement is what Gui *et al.* point out to be the main difference for obtaining CNT-sponges rather than CNT powder.

Herein, the following synthesis parameters were optimized: first, at a constant carrier gas flow rate of 2.6 $L{\cdot}min^{-1}$ (Ar/H_2) and a 0.23 $ml{\cdot}min^{-1}$ precursor-solution injection rate (ferrocene + dichlorobenzene), the thickness of CNT-sponges was checked for times of 1, 2, 3 and 4 hours. Sponges synthesized during an hour were extremely thin (0.8 mm). For 2 hours, the reached thickness was ∼3.1 mm, while growth for 3 and 4 caused the partial obstruction of the quartz tube by the carbonaceous matter deposited around its walls. Lower injection rates of 0.13 and 0.18 $ml \cdot min^{-1}$ for growth times of 3 and 4 hours were also attempted, however, both injection rates yielded brittle sponges, and not thicker than 3 mm.

The grow rate of CNT-sponges should be around 0.8-1 mm per hour and furthermore, growth should not be interrupted or decreased up to 4 hours, according to previously published works[31]. It is suggested that the growth in this study is limited by the quartz tube diameter (1 inch), which is half the diameter of the one used in the work

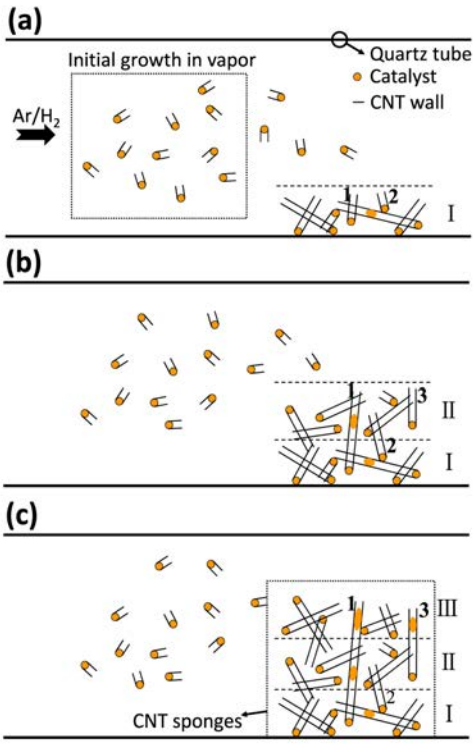

FIGURE 3.25: The growth mechanism of CNT-sponges involves three stages (a, b and c). I, II and III illustrate how the growing stages lead to the thickness swell of the sponge through the continuous elongation of first-grown tubes (1 and 2) and the deposition of new tubes (3) on top.[31]

by Gui *et al.* Due to this limitation, here the synthesis time was set at 2 hours: for injection rates of 0.13, 0.18 and 0.23 $ml \cdot min^{-1}$, thicknesses were typically around 1.9, 2.8 and 3.1 mm, respectively, although in the latter case sponges showed again some brittleness, hence 0.18 $ml \cdot min^{-1}$ was chosen as the optimal injection rate. CNT-sponges acquired by the optimum conditions were highly compressible and bendable, without any sign of brittleness (Figure 3.24).

SEM and TEM images (Figure 3.26) reveal that the material is formed by a network of highly interconnected and randomly distributed CNTs, with average diameters close to 23 nm and lengths ranging from tens to hundreds of micrometers. Inner residual particles were found in some CNTs and through TGA, it was seen that these particles constitute *ca.* 30 $wt\%$ of the weight of the sponge (Figure 3.27).

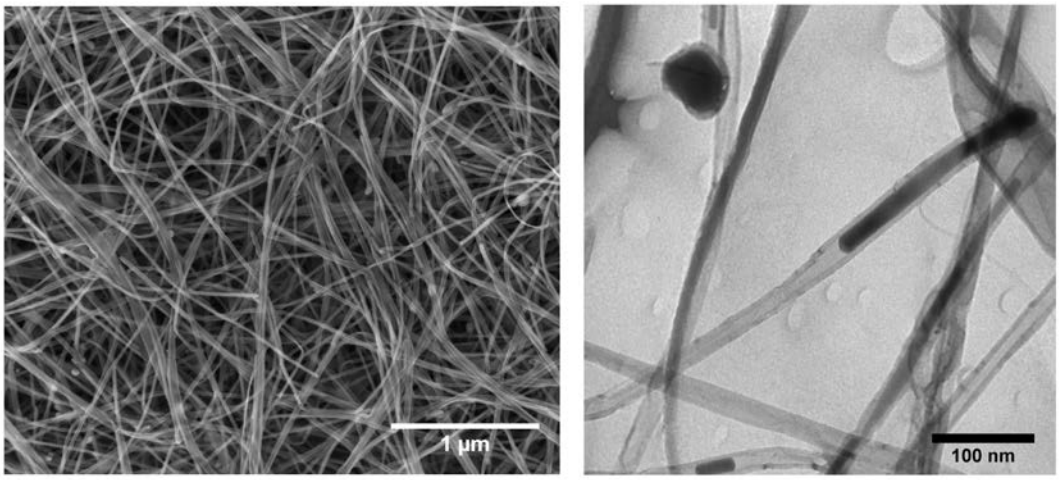

FIGURE 3.26: SEM image of the CNT-sponge microstructure (left) and TEM image of the CNT-sponge dispersed in ethanol using an ultrasonic tip (right) where it can be seen that CNTs are partially filled with residual particles from the iron catalyst

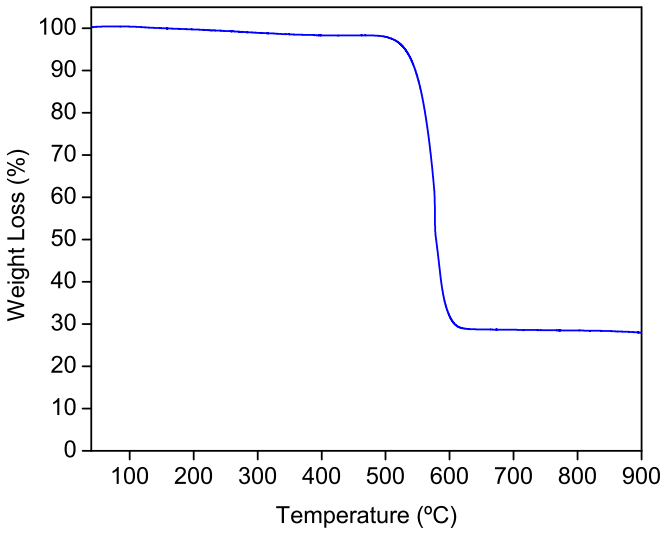

FIGURE 3.27: TGA of CNT-sponges:∼30 $wt\%$ of the sample is non-carbonaceous matter, which can be mainly attributed to residues from the catalyst

The XRD pattern in Figure 3.28 allowed to elucidate the main components of CNT-sponges. The peak at 26.1 degrees can undoubtedly be addressed to the diffraction contribution of the (002) planes of the hexagonal graphite lattice. The convoluted multi-peak centered on $2\theta^{\circ} \sim 45$ can be attributed to the most intense signals of Fe_3C at 45.01, 44.60, 45.92 and 49.16 angles corresponding respectively to the (031), (220), (112) and (221) planes.

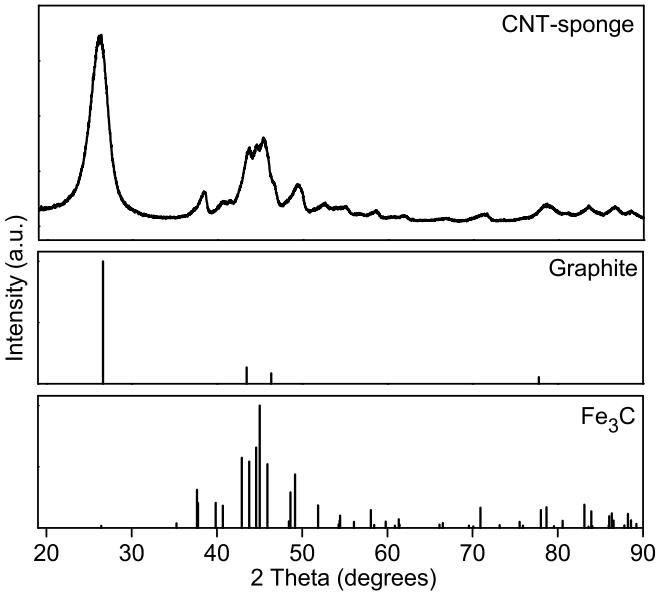

FIGURE 3.28: X-Ray diffraction pattern of the CNT-sponge (experimental data) and the MAUD fitting considering graphite (AMCSD code: 0018291) and iron carbide (AMCSD code: 0019097) as main phases

Raman spectroscopy was employed to evaluate the isotropy of CNT-sponges. Spectra from the cross-section of sponges, as well as from the top and root growth faces, are shown in Figure 3.29. Typical D- and G-bands located at 1345-1350 and 1579 cm^{-1}, respectively, are seen in all cases. Slight variations in the intensity ratio of these bands (I_D/I_G) were observed for the root growth ($I_D/I_G = 0.67$) and top faces ($I_D/I_G = 0.51$) of the samples. These differences were attributed to a higher proportion of defects in the root growth face, which is exposed for longer times than the top

face to chlorine radicals formed during the decomposition of dichlorobenzene (carbon precursor).

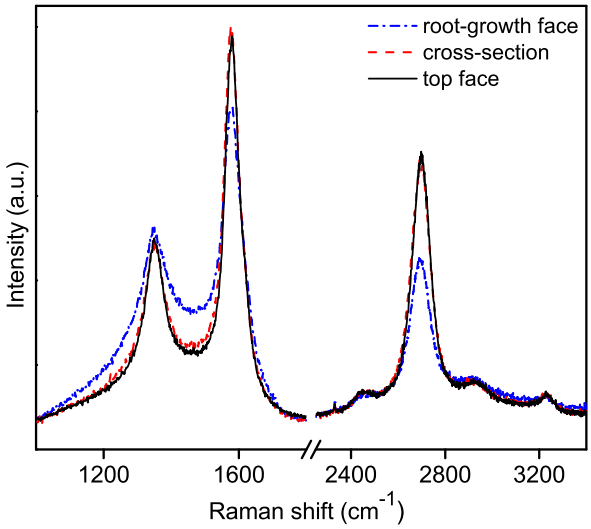

FIGURE 3.29: Raman spectra of the cross-section, and the top and root growth faces, of CNT-sponges

Despite the high entanglement degree, the material is ultra-light; the apparent density (weight/volume) obtained by average of at least 8 samples, consistently showed values lower than 0.02 $g \cdot cm^{-3}$. CNT-sponges are strongly hydrophobic (water contact angle $\sim 135°$), hence sponges are able to absorb oil quantities of about 52 times its own weight (Figure 3.30), even at low temperatures (0 $°C$). Oil absorption measurements in Figure 3.30, were done by recording the weight gain of sponges after immersing them in oil and checking afterward the weight loss upon burning the absorbed oil. A slight decreasing trend in the weight of the sample after each immersion-burning step is seen, probably due to the thermal degradation of CNTs.

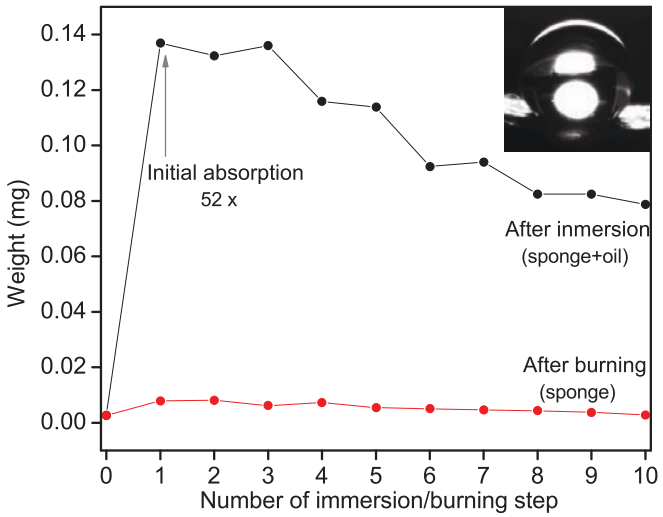

FIGURE 3.30: (a) Image: water drop on top of a CNT-sponge; after one minute the contact angle is $\sim 135°$. (b) Oil absorption capacity: samples were weighted before and after repeatedly immersing them in cold ($0\,°C$) mineral oil (sponge+oil). Samples were then burned, to eliminate the oil, and re-weighted (sponge)

I.5 SUMMARY

• Nanoferrites with different stoichiometries of $Cu - Ni$ were synthesized at 700 $°C$ within mesoporous silica micro-particles (template). The $Ni_{0.5}Cu_{0.5}Fe_2O_4$ ferrite-silica hybrid showed a superparamagnetic behavior and the highest saturation magnetization. TEM revealed $Ni_{0.5}Cu_{0.5}Fe_2O_4$ ferrite nanoparticles with diameters of ∼8.3 nm. Nevertheless, when annealing was done at 900 $°C$, $Ni_{0.5}Cu_{0.5}Fe_2O_4$ ferrite nanoparticles showed a broader and non-symmetric size distribution, with diameters between 15 and 80 nm. This size increment is likely responsible of the enhanced saturation magnetization and hysteresis losses of this sample. The surface area decreased sharply when the neat silica was loaded with ferrite nanoparticles, providing evidence for the filling of the pores. However, the small reduction of the pore diameter might indicate a non-homogenous filling. The surface area of the silica-ferrite hybrid annealed 900 $°C$ is lower than that of the hybrid annealed at 700 $°C$, which is consistent with the larger particle size determined through TEM and XRD. Thereby, both the temperature and the silica template, play an important role in the growth of the magnetic nanocores.

• The combination of CNFs and magnetite nanoparticles in a 50:50 weight ratio has been achieved through a very simple protocol. XRD has proved the preservation of the original crystallographic structure from both the magnetite nanoparticles and the pristine CNFs upon the procedure. Although the arrangement of nanoparticles over the surface of the CNFs is not uniform, the hybrids show a superparamagnetic behavior, which indicates that particles are single domains.

• CNxNTs have been synthesized, oxidized and densely decorated with nearly monodisperse magnetite nanoparticles (7.8 nm). Anisotropic scaffolds of CNxNTs and magnetite-decorated CNxNTs were prepared from aqueous-CHI primary dispersions *via* uniaxial freeze-drying. Morphological differences of scaffolds were attributed to the dispersion degree of nanotubes attained in the primary dispersions. Scaffolds of non-decorated

CNxNTs (C3 and C6) showed poorer dispersion and in turn, presented less ordered structures. Lower void areas and some big agglomerates were observed in these latter. In contrast, magnetite decorated CNxNTs showed good dispersion and scaffolds presented a well-defined porous structure of closely packed and randomly distributed CNxNTs in their walls (CM3 and CM6). In all cases, the density was lower than 0.07 $g \cdot cm^{-3}$, which indicates that the original amount of nanotubes is forming a percolating network through a large macroscopic volume. The thermal degradation was anticipated in samples containing magnetite, probably due to the presence of capping agent over the nanoparticles surface and due to the inherently high thermal conductivity of magnetite nanoparticles. CM6 was subjected to an additional thermal treatment at 360 $°C$, which did not alter the structure of the original scaffold. This treatment might enhance further the interconnectivity of adjacent CNTs in the scaffold.

• Flexible and mechanically though CNT-sponges were synthesized through CVD. Through the optimal conditions, sponges of at least 2.8 mm in thickness were obtained. Sponges are composed solely by CNTs, without any polymer binder. Nevertheless, residual particles from the CVD catalyst could be also observed within their cores. The microstructure of the sponges showed a random distribution of interconnected nanotubes with diameters of $\sim$ 23 nm. Sponges are ultra-light: their density is as low as 0.02 $g \cdot cm^{-3}$. In addition, CNT-sponges are able to absorb huge oil quantities, in consistency with a nearly superhydrophobic behavior.

PART II

COMPOSITES WITH MAGNETIC NANOPARTICLES AND NANOCARBONS:

Preparation and application to EMI shielding

Results & Discussion

PART II

II.1 NANOFERRITE-SILICA EPOXY COMPOSITES

Ferrites were chosen as magnetic fillers of composites due to their inherent magnetic loss, which can induce magnetic spin rotation and heat dissipation to the matrix [32]. This mechanism could be appropriate to protect the internal elements of electronic devices from undesired EM interferences. Ni-ferrites and their substituted counterparts, e.g. Zn, Co, Cu, Mn, have gained relevance due to their promising high-frequency application [33]. On the other hand, Cu-ferrites have shown enhanced thermal, magnetic and dielectric properties [8,34] and its combination with Ni, e.g. $Ni_{1-x}Cu_xFe_2O_4$, has led to materials with EMI shielding properties with maximum reflection loss (-25 dB) for the composition of $x = 0.5$ [12].

Magnetic multi-scale composites were prepared by the incorporation of $Cu_{0.5}Ni_{0.5}Fe_2O_4$ ferrite/silica hybrids in an epoxy matrix. The interaction of this silica-ferrite reinforcement as well as its distribution within the matrix is evaluated with respect to the enhancement of the thermal properties of composites. Their SE and related properties are explored between 1 and 18 GHz.

II.1.1 General characteristics

To overcome agglomeration of nanoparticles within the matrix, it is here proposed to keep the micron-sized silica template, employed in the first place for constraining the magnetic cores during its growth. The unique surface chemistry of silica can provide enhanced compatibility with polymers and might serve also to avoid the oxidation of nanoparticles [35,36].

Epoxy composites containing 10, 15, 20 and 25 $wt\%$ of the $Cu_{0.5}Ni_{0.5}Fe_2O_4$ ferrite-silica hybrids (annealed at 700 and 900 $°C$) were prepared. 25 $wt\%$ was the maximal loading that enabled processing, beyond this concentration the increased viscosity of the epoxy resin made degassing unmanageable.

Figure 3.31 shows as an example, representative SEM images of the composites prepared with particles annealed at 900 $°C$. The continuous dark phase corresponds to the epoxy matrix while polyhedral light grey regions correspond to the silica particles.

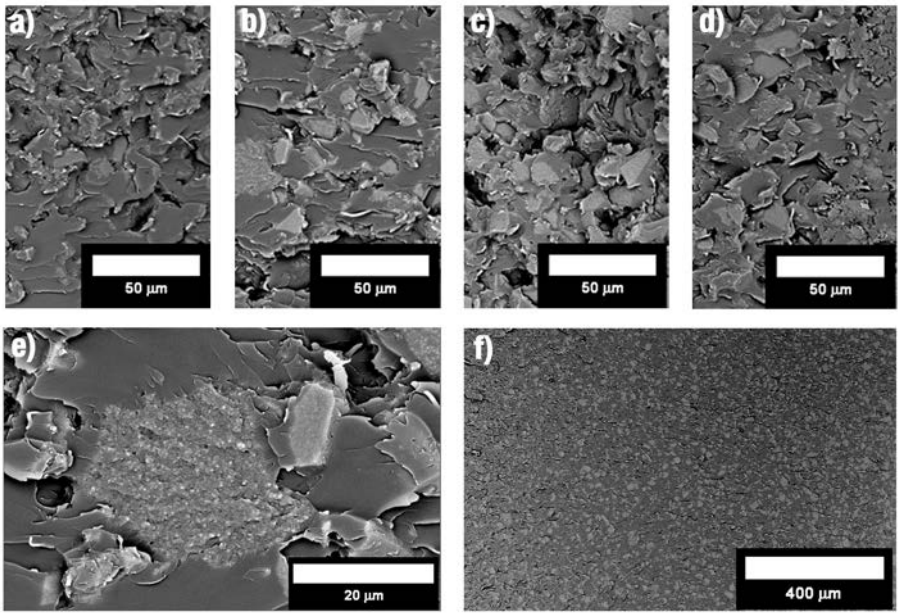

FIGURE 3.31: Fracture surface of the ferrite/silica (annealing temperature, 900 $°C$) epoxy composite with the different prepared compositions: (a) 10,(b) 15, (c) 20 and (d) 25 $wt\%$.(e) Detail of a ferrite-silica particle in the epoxy matrix and (f) representative overview of the dispersion degree

The resolution of images is not high enough to observe the ferrite nanoparticles, but very small spherical brighter features are intuited (Figure 3.31 e). No evident voids are seen at the silica/epoxy interface, which indicates a good interaction between the particles and the matrix. Additionally,homogeneous dispersions of the micro-particles within the whole composite cross-section were achieved (Figure 3.31 f). Since the

ferrite nanoparticles are constrained inside these micron-sized particles, the micro-homogeneity implies that the ferrite particles are dispersed at the same extent than the micron-sized silica particles. In turn, the nano-dispersion has also been achieved by means of simple low-energy mechanical mixing.

In order to evaluate further the interaction between the hybrid ferrite-silica particles and the matrix, the glass transition temperature (Tg) of the composites was determined by DSC (Table 3.5). An increase in the Tg of all samples is seen when compared to the neat epoxy. This effect has been previously reported for other polymer-based composite materials at comparable inorganic-filler loadings [37,38] and epoxy-based composite materials with rough surface inorganic particles [39,40]. The local reduction of the free volume of the polymer chains nearby the filler surface enhances the interaction between both phases. Therefore, increasing the polymer/filler contact surface (high specific surface area fillers) may also contribute to hinder the polymer motion [41].

TABLE 3.5: Glass transitions temperatures for ferrite-silica/epoxy composites for particles annealed at 700 $°C$ (Tg_{700}) and at 900 $°C$ (Tg_{900})

Filler, $wt\%$	**0**	**10**	**15**	**20**	**25**
$\boldsymbol{Tg_{700}}$, $\boldsymbol{°C}$	215	216	220	222	221
$\boldsymbol{Tg_{900}}$, $\boldsymbol{°C}$	215	216	217	220	218

This Tg increase is observed for both ferrite-silica composites up to 20 $wt\%$. Nevertheless, it is more relevant for the ferrite-silica particles prepared at 700 $°C$, which consistently showed a higher surface area.

The thermal stability of composites was evaluated by TGA in air atmosphere (Figure 3.32). None of the recorded thermograms showed hydration loses at low temperatures ($\leq$ 200 $°C$), which is a common problem observed for epoxy resins modified with hygroscopic fillers such as silica [42]. Furthermore, two weight loses were observed in all cases, as in many other epoxy-based materials [43,44].

As reported elsewhere, these weight loses are related to the commonly accepted three-step degradation mechanism of epoxy networks: First, at $\sim$ 240 $°C$, homolytic cleavage

without significant weight loss takes place and subsequently, a major weight loss is caused by the dehydration of the alcoxy groups, followed by the formation of double bonds. The final degradation step, occurring at about 530 $°C$, can be ascribed to the oxidation of the residual species formed after the thermal degradation in air through different reaction mechanisms involving radicals from the initial stages of degradation.

All composites were found to be stable, at least up to 340 $°C$. In all cases, the onset decomposition temperature ($T_{5\%}$, Table 3.6) shifted towards higher temperatures when compared to the neat epoxy.

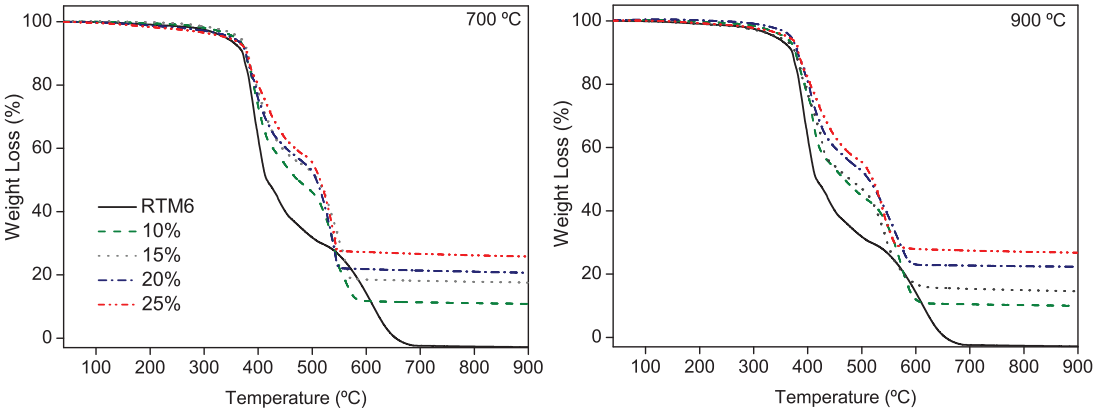

FIGURE 3.32: TGA curves for composites with ferrite-silica particles annealed at: 700 (a) and 900 $°C$ (b)

Since several overlapping degradation steps are observed, the integral procedure decomposition temperature (IPDT) seems to be a more appropriate parameter to investigate the global thermal stability of composites[45]. According to Doyle *et al.*[46] the IPDT can be defined as:

$$IPDT = A \cdot K(T_f - T_i) + T_i \tag{3.3}$$

Where T_i and T_f are the initial and final experimental temperatures respectively, A is the ratio between the area below the experimental TGA curve ($S_1 + S_2$) and the total area of the thermogram ($S_1 + S_2 + S_3$); and K represents the ratio between the area below the experimental TGA curve ($S_1 + S_2$) and the area of only the residual part of

the experimental curve (S_2), as given by:

$$A = \frac{S_1 + S_2}{S_1 + S_2 + S_3} \tag{3.4}$$

and

$$K = \frac{S_1 + S_2}{S_2} \tag{3.5}$$

The IPDT values are summarized in Table 3.6. Results show that the thermal stability of composites increases with the content of the inorganic filler, independently of its type (annealed at 700 or at 900 $°C$).

TABLE 3.6: Onset decomposition temperature ($T_{5\%}$) residual weight percentage and IPDT for the ferrite-silica/epoxy composites

	Particles synthesized at 700 °C			**Particles synthesized at 900 °C**		
Filler, wt%	**Residue, wt%**	**$T_{5\%}$, °C**	**IPDT, °C**	**Residue wt%**	**$T_{5\%}$, °C**	**IPDT, °C**
0%[a]	-	340	316.2	-	340	316.2
10%	10.8	258	410.9	10	357	404.9
15%	17.6	365	489.7	14.6	344	452.7
20%	20.7	351	529.4	22.4	369	554.3
25%	25.8	342	606.9	26.8	362	623.3

[a]The values obtained for the neat resin are included for comparison

An improvement in the thermal stability of the organic matrix may be expected solely by the fact that silica has an inherently high thermal stability[47]. Nevertheless, the inhibition of the matrix decomposition during the calcination process could be also attributed to a mass transfer barrier effect[48] and to improved adhesion at the filler/-matrix interface[49]. This improvement is consistent with the Tg increment observed by DSC.

II.1.2 EMI shielding and complex permittivity/permeability analysis

The total electromagnetic shielding efficiency (SE_T) of the ferrite-silica composites is presented in Figure 3.33, within 1 and 18 GHz. All samples, including the neat epoxy resin (RTM6), exhibit a sinusoidal profile with a modest increasing tendency with frequency. In a general way, maximum SE_T values do not exceed 2 dB (less than a 1.6 power change), which means that silica-ferrite composites render poor EMI shielding efficiency.

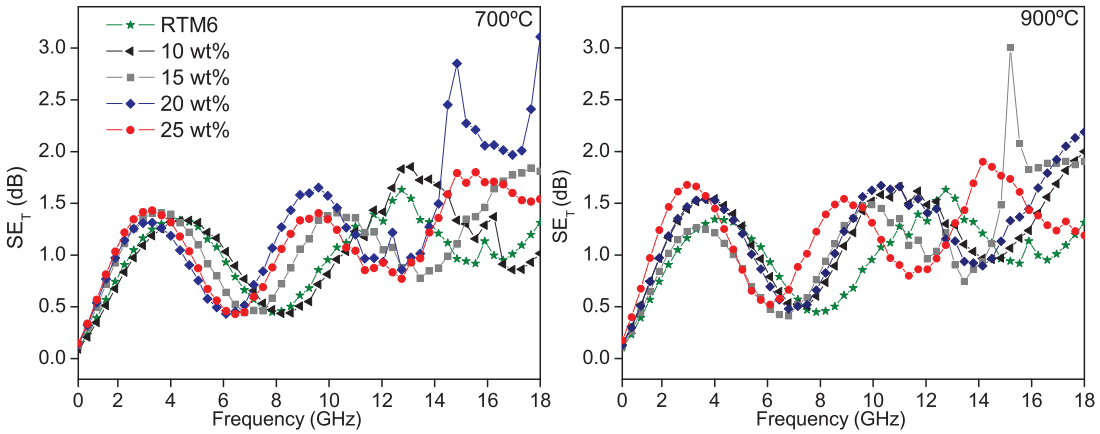

FIGURE 3.33: Total shielding efficiency (SE_T) of epoxy composite slabs (thickness: 11 mm) prepared with ferrite-silica particles annealed at 700 (left) and 900 $°C$ (right)

Although all composites showed a ferromagnetic behavior when placed near a magnet, they all have low loads of magnetic inclusions ($\sim$ 23 $wt\%$ from the net silica-ferrite loading). Therefore, their saturation magnetization should fall even to lower values than those observed for the silica-ferrite hybrid materials (4.06 and 7.47 $emu \cdot g^{-1}$ for annealing temperatures of 700 and 900 $°C$, respectively). The poor SE_T values could be attributed to this fact. The limitation of processing composites with higher ferrite-silica concentrations suggests that for EMI shielding applications, these materials are still far from the expected EM behavior. Indeed, in most magnetically active EMI shielding composites the loading at which the magnetic nanoinclusions start to be noticeable is steadily above 50-70 $wt\%$.

The sinusoidal shape of the curves can explained through the evaluation of the reflection component of the total shielding efficiency, while the ascendant trend can be ascribed to the absorption component. As observed in Figure 3.34 (bottom), SE by absorption (SE_A) increases with frequency for all composites and its magnitude slightly increases with the silica-ferrite loading.

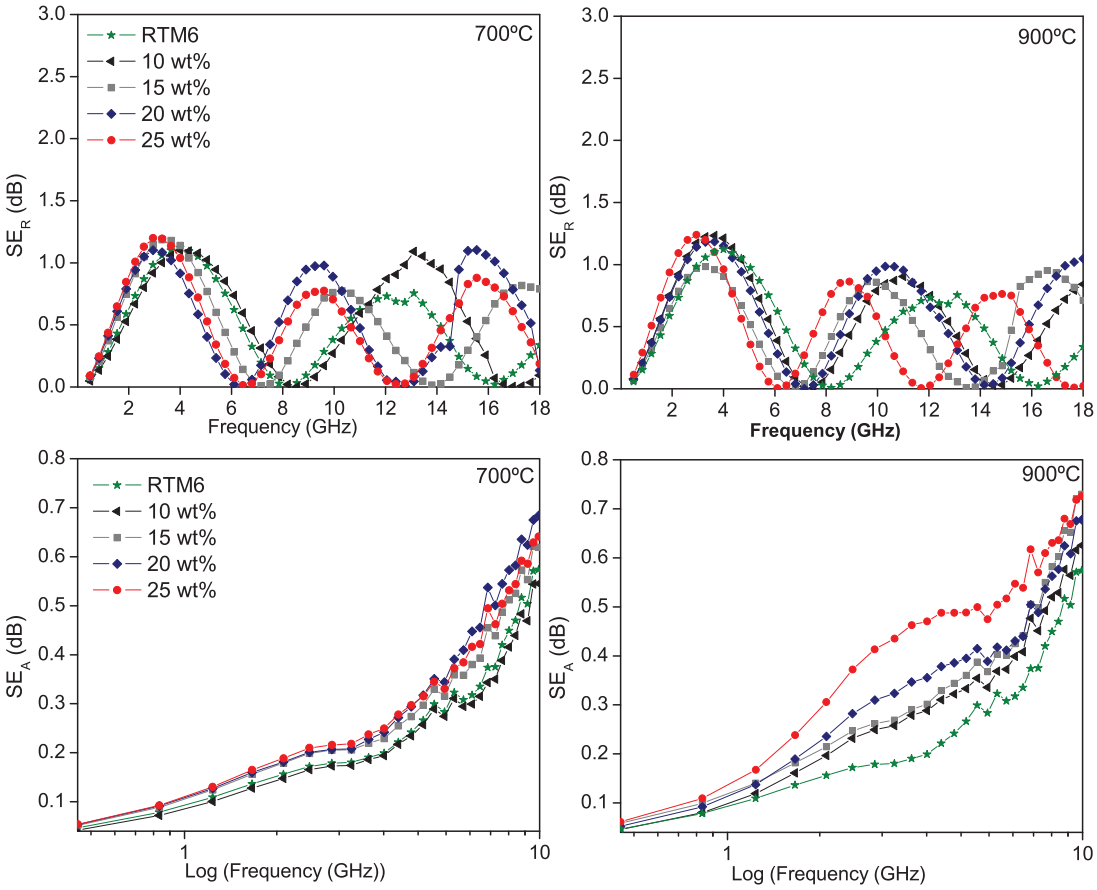

FIGURE 3.34: SE_A (bottom) and SE_R (top) of epoxy composites prepared with ferrite-silica particles annealed at 700 (left) and 900 $°C$ (right)

For each weight percentage, composites prepared with silica-ferrites annealed at 900 $°C$ systematically show slightly higher SE_A values than their 700 $°C$ counterparts. Figure 3.34 (top) also shows how the SE due to reflection (SE_R) presents the same equidistant dips than SE_T, which correspond to minimum reflection values. This observation

can be explained by considering the reflections that occur in electromagnetically thin slabs or slabs that are thinner than their skin depth.

The skin depth (δ) decreases for increasing frequency (f), conductivity (σ) and permeability (μ). In these composites, the electrical conductivity is negligible, since they are composed of two intrinsically insulating materials (polymer, silica $\sigma \sim 10^{-11}$-10^{-15} $S \cdot m^{-1}$) and non-interacting ferrite nanoparticles. For these 11 mm-thick slabs, the skin depth is always greater than the sample thickness therefore, EM waves will be able to fully penetrate the cross-section of materials. At the front-face of slabs (input surface) EM waves will be partially reflected, due to the impedance mismatch between air and the material, and the rest will penetrate until it reaches the second incident plane of slabs (output surface). At this point, the wave will be partly transmitted out from slabs and will also get reflected back to the source. Reflections occurring at both surfaces of slabs (input and output) will interfere destructively or constructively and therefore maximum and minimum reflections will be recorded at certain frequencies (Figure 3.35). Minimal reflection dips are observed when the thickness (t_m) and the wavelength of the propagating medium (λ_m) are "matched" or satisfy the condition of $t_m = n\lambda_m/4$ ($n = 1, 3, 5, 7, 9 \dots$), hence the number of dips increases with the sample thickness[50].

The magnitude and position of these dips are not exclusively determined by the sample thickness, as they depend also on the wavelength of propagation in a medium with certain complex permittivity and permeability. This propagating wavelength can be expressed by[51]:

$$\lambda_m = \frac{\lambda_0}{(|\mu_r||\epsilon_r|)^{\frac{1}{2}}} \tag{3.6}$$

where $|\mu_r|$ and $|\epsilon_r|$ correspond to the modulus of complex relative permeability and permittivity of the propagating medium respectively, and λ_0 is the wavelength of free space ($\lambda_0 = c/f$).

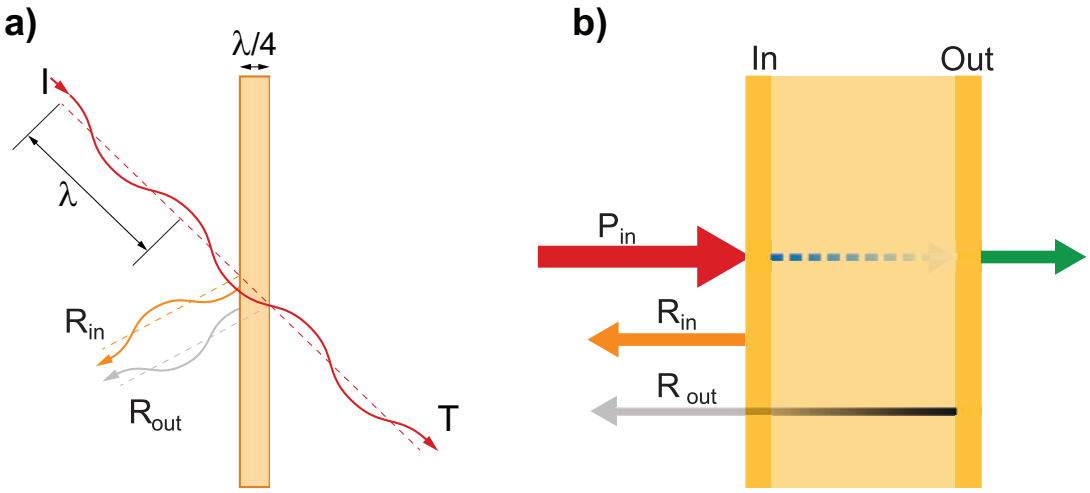

FIGURE 3.35: a) Schematic illustration of the destructive interference between the reflected waves impinging on a slab of thickness (t) that satisfies the condition of $t = \lambda/4$ [52]. b) Reflections that occur at the input and output interfaces of an electromagnetically thin slab

As seen in Figure 3.34, the dips in SE_R are shifted towards lower frequencies when the filler $wt\%$ is increased in both composite series. Similar observations have been reported for other ferrite-polymer composites [53,54] that were designed to serve as effective quarter-wave thick absorbing layers (Appendix A). This phenomenon implies a change in the complex relative permittivity and/or complex relative permeability with the filler loading. Recalling previous definitions, complex permittivity (ϵ) and permeability (μ) magnitudes are described by an imaginary component (ϵ'' or μ'') related to the loss of energy and a real component (ϵ' or μ'), which gives information about the stored EM energy.

The effect of the silica-ferrite loading on the permittivity of composites is shown in Figure 3.36. The real part increases with the filler loading while the imaginary part remains almost unaltered for both sets of composites.

In general, the dielectric loss (imaginary permittivity) of polycrystalline ferrites is commonly attributed to the electron diffusion between iron ions in different oxidation states (Fe^{3+} and Fe^{2+}) which in turn causes some conduction [10,55]. But this effect was

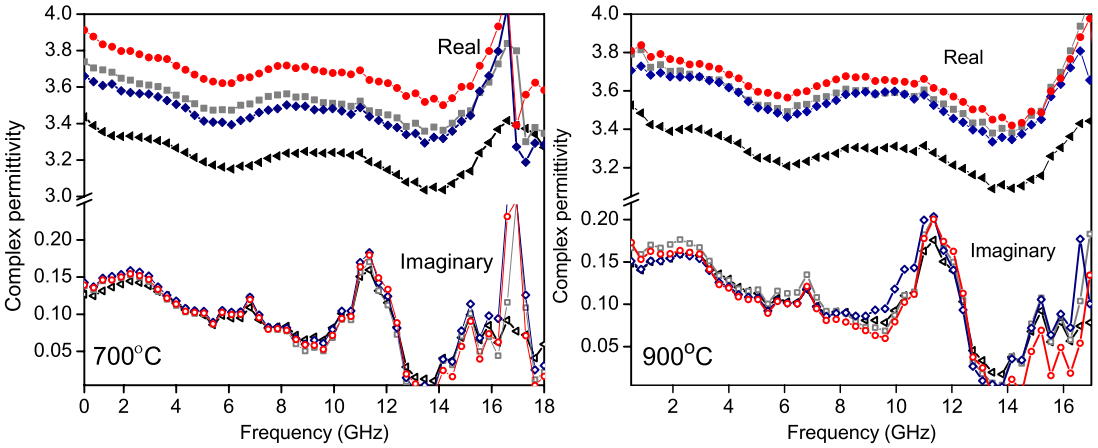

FIGURE 3.36: Complex permittivity of ferrite-silica composites: particles annealed at 700 $°C$ (left) and annealed at 900 $°C$ (right). For both sets of composites: full symbols correspond to the real permittivity and open symbols to the imaginary part. Symbols for each composition: 10 $wt\%$(◀), 15 $wt\%$(■), 20 $wt\%$(◆) and 25 $wt\%$(●)

inferred to be rather low in $Cu-Ni$ ferrites synthesized at similar temperatures as the herein reported, due to the low probability of promoting different valence states with low sintering temperatures [56]. In the ferrite-silica composites, this type of conduction can be neglected solely by the fact that the measured permittivity depends not only on the local conduction between the ferrite nanoparticles (which are constrained inside the silica microparticles), but also on their long range percolation throughout the polymer matrix. In addition, both the silica and the polymer matrix are characteristically low dielectric loss materials, which justifies the small magnitude of the imaginary permittivity of all samples.

Real permittivity is related to the degree of polarization and, in the GHz range, it arises mainly from dipolar and interfacial polarization processes [57]. The magnitude of ϵ' is rather low in all composites, since the main constituents (silica and epoxy) have low dielectric constants. The real permittivity of both sets of composites increases with the filler loading (increased number of interfaces), although a slight discrepancy is seen for the composition with 15 $wt\%$. Furthermore, a broad peak is seen at 8-9 GHz for

all compositions, which coincides with a sharp peak in the imaginary permittivity. Although the fundamental understanding of the origin of this peak cannot be established, we hypothesize that it might imply a dielectric relaxation in the system.

The variation in permeability with the silica-ferrite loading is shown in Figure 3.37. For both sets of composites, the real part decreases with the filler loading while the imaginary part does not show any clear tendency. A similar behavior (trend and magnitude) has been observed for other ferrite-polymer composites and even for very high magnetic-phase loadings[58,59].

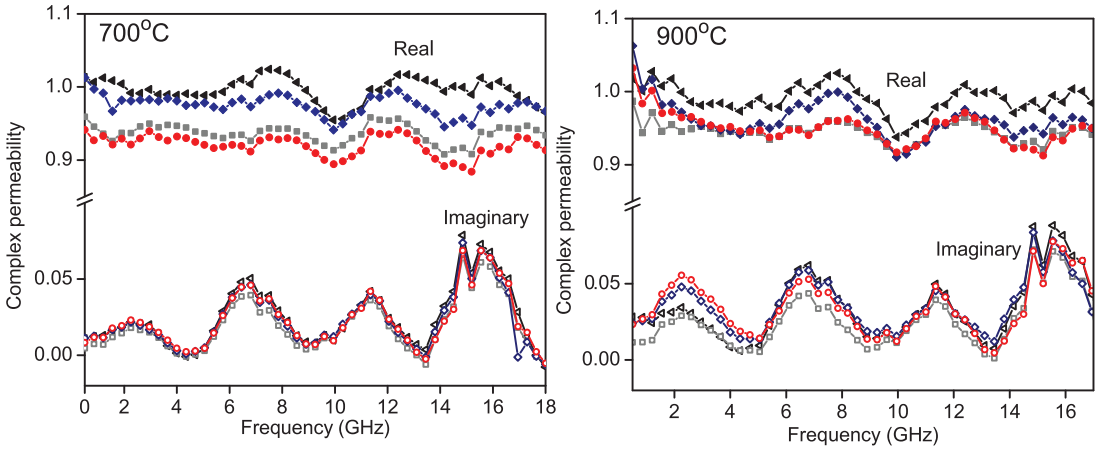

FIGURE 3.37: Complex permeability of ferrite-silica composites: particles annealed at 700 $°C$ (left) and annealed at 900 $°C$ (right). For both sets of composites: full symbols correspond to the real permittivity and open symbols to the imaginary part. Symbols for each composition: 10 $wt\%$(◀), 15 $wt\%$(■), 20 $wt\%$(◆) and 25 $wt\%$(●)

Magnetic loss (imaginary permeability) arises from hysteresis, motion of magnetic domain walls, eddy current losses and natural ferromagnetic resonance[60]. Hysteresis loss for both types of ferrite-silica particles (annealed at 700 and 900 $°C$) is almost negligible (see section I.1.2, Figure 3.6). Furthermore, magnetic domain wall resonance occurs normally in-between 1 and 100 MHz, and since ferrite nanoparticles are isolated from each other, at least at some extent, eddy current losses should be also negligible. Thus, in these ferrite-silica hybrids, the energy loss should be mainly associated to the natural resonance, which for nanometric magnetic particles, could occur in the GHz

range[61]. In such situation, a broad magnetic resonance peak should be observed in the imaginary permeability (loss), accompanied by a steep decrease in the real component (gain). In our composite systems, the imaginary permeability presents several peaks, although their magnitude is small enough to consider them fluctuations from the measuring system. We are therefore not able to discern any magnetic process that occurs in composites prepared with the specified ferrite-silica loads. This could be the underlying reason for the poor SE ability observed in all composites.

II.2 EPOXY COMPOSITES WITH MAGNETITE NANOPARTICLES AND CARBON NANOFIBERS

CNFs have been extensively incorporated in polymer matrices essentially due to their high electric conductivity and aspect ratio[62–67]. These characteristics enable preparation of affordable CNF composites with a remarkable efficiency towards EMI shielding[68,69]. Since the combination of nanocarbons with magnetic constituents can enhance the EM loss of such composites[70], it is yet possible to find some works in the literature where CNFs have been combined with magnetic particles; for example with $Fe-Ni$ particles[71], or with both graphene and $\gamma-Fe_2O_3$ particles to increase simultaneously the conductivity and the EM loss[72]. However, due to the small fraction of magnetically permeable particles found in most reported works, it is still unclear if enhanced EM absorption can be truly attributed to the effect of the magnetic constituent.

In this section, the EMI shielding behavior of thermosetting composites containing CNFs or magnetite nanoparticles is compared with that of composites containing magnetite-decorated CNFs in a 50:50 weight ratio[7].

II.2.1 General characteristics

Magnetite-decorated CNFs were mixed with the epoxy resin to obtain 2, 5 10 and 20 $wt\%$ composites. Representative SEM images of cured specimens are shown in Figure 3.38. For the composite with the lower $wt\%$, it can be seen a clean fracture surface, which is characteristic of brittle epoxy resins. As the $wt\%$ increases,rougher surfaces are observed, suggesting a reinforcing effect due to the presence of the CNFs. Low-magnification images show a uniform dispersion of decorated CNFs within the matrix. Moreover, no evident fiber pullout, phase segregation or interface voids are seen.

[7]CNF-based composites were fabricated and their experimental characterization was carried out by N. Méndez as part of a collaborative research project.

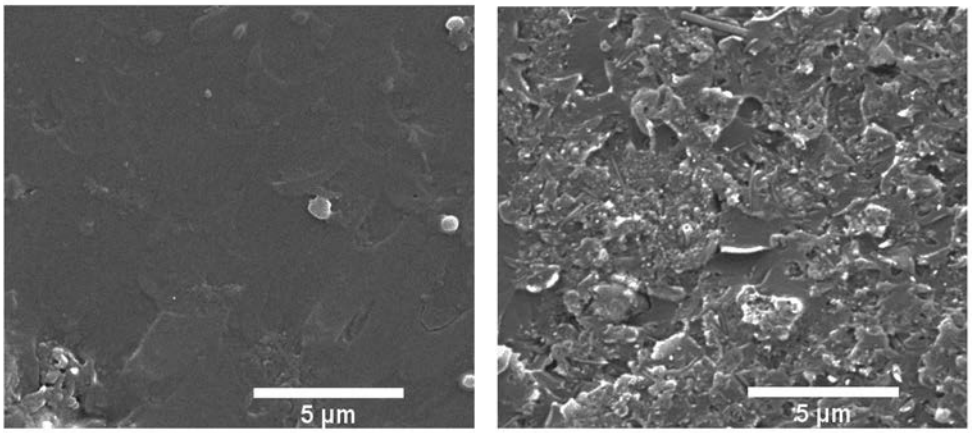

FIGURE 3.38: SEM images of nanocomposites with different CNF/Mag loads where it is seen the different fracture type when the content of reinforcement is increased. Left: composite with a 5wt% CNF/Mag loading showing a clean fracture surface; right: composite with a 20wt% CNF/Mag loading

The influence of CNT/Mag wt% on the glass transition temperature (Tg) of composites was evaluated through DSC. As can be seen in Table 3.7, the Tg decreases in all samples, except for the one containing a 5 wt% of filler, when compared to the neat epoxy. This effect has also been observed in other nanocarbon/epoxy composites [73]. Some theoretical works suggest that a slight decrease in the Tg might be expected in well-dispersed nanocomposites due to a more compressible interface [74]. In addition, since the magnetite particles are covered with oleic acid chains, these could as well induce some plasticity at the filler/matrix interface, hence the decrease in the Tg.

TABLE 3.7: Glass transitions temperatures (Tg) of the epoxy composites with varying loads of CNT/Mag

Filler, wt%	**0**	**2**	**5**	**10**	**20**
***Tg*, °C**	77	72	77	65	72

For comparison purposes, composites with equivalent concentrations to those of the CNF/Mag composites (2, 5 10 and 20 wt%), were prepared though the incorporation of either pristine CNFs (epoxy-CNF) or magnetite particles (epoxy-mag) in the resin.

As the weight ratio of CNFs to magnetite particles is 50:50 for the CNF/Mag composites, the following weight fractions were selected for the epoxy-CNF and epoxy-mag composites: 1.2, 2.5, 5 and 10 $wt\%$. In this way, either single-phase composite has an equivalent amount of magnetite or CNFs than their CNF/Mag analogues. The representative TGA (under N_2 atmosphere) shown in Figure 3.39 corroborates the equivalency of such composites.

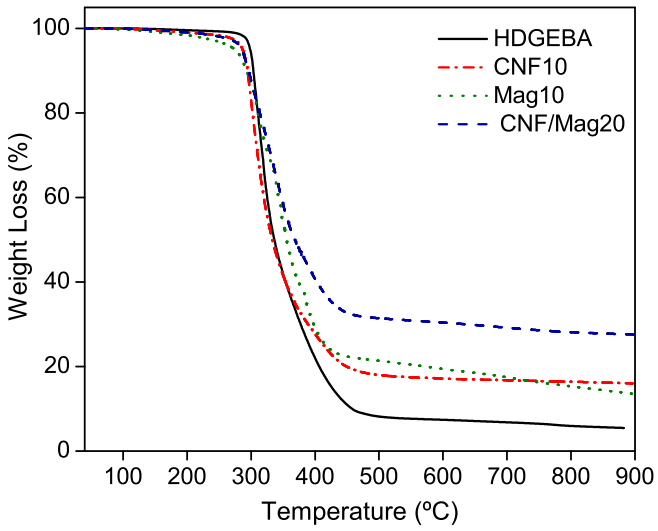

FIGURE 3.39: TGA curves performed under N_2 atmosphere of the epoxy resin (HDGEBA), epoxy-CNF or epoxy-Mag composites with a load of 10 $wt\%$ and CNF/Mag-epoxy composite with the equivalent 20 $wt\%$ load

II.2.2 DC-electrical conductivity

Results on the DC electrical conductivity of composites with CNF and CNF/Mag are shown in Figure 3.40. The conductivity of the neat epoxy is below the detection limit of the instrument used in these measurements, since it is an insulating material ($\sigma \approx 10^{-15}\ S \cdot m^{-1}$). The values obtained for the composites with decorated and non-decorated nanofibers increase with the CNF concentration, ranging between 10^{-6} (typical for insulating materials) to 0.2 $S \cdot m^{-1}$ (typical of semiconductors) for 1 and

10 *wt*% respectively. A similar trend in conductivity was observed for CNF/Mag composites, but the values were one order of magnitude below the ones observed for pristine CNFs. The elevated conductivity values of composites containing the lowest CNF and CNF/Mag concentrations indicate that even at low loadings, the system is beyond the percolation threshold.

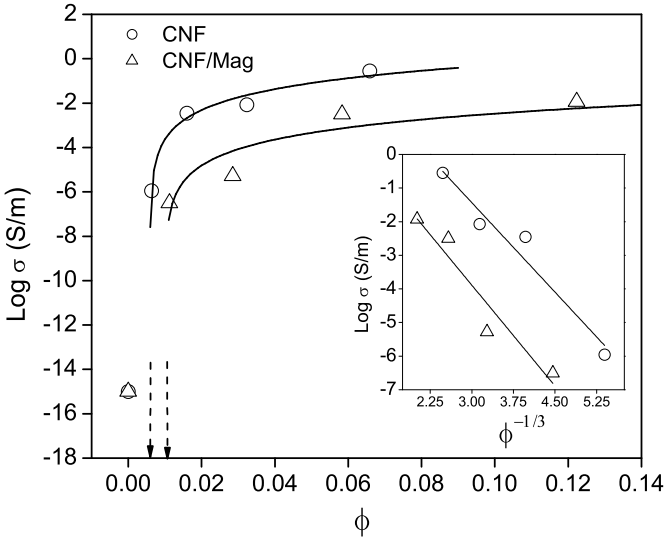

FIGURE 3.40: DC conductivity of CNF (◯) and CNF/Mag (△) composites as a function of filler volume fraction. Solid lines are the best fit to $\sigma \propto (\phi - \phi_C)^t$. Inset: DC conductivity as a function of $\phi^{\frac{-1}{3}}$ (see text for details)

The percolation threshold is related to the contact between fibers and depends strongly on their aspect ratio and dispersion degree. Thereby, it is difficult to compare results from different authors: reported values for CNF polymer composites might be between 7-8 *wt*%[75] or 0.5-1 *wt*%[76]. This discrepancy could be avoided by analyzing the data in terms of the percolation theory[77], having the conductivity (σ) as a function of the volume fraction (ϕ) as given by: $\sigma \propto (\phi - \phi_C)^t$, where ϕ_C represents the volume fraction at the percolation limit. As shown in Figure 3.40, percolation thresholds of 0.6 and 0.1 *vol*% were obtained for CNFs and CNF/Mag respectively (see the *vol*% and *wt*% correspondences in section 2.1.2). The exponent $t \sim 2.2$ was the same for

both fillers within the experimental error, being in accordance with reported values for analogue polymer/conductor composites[78].

The fact that both fillers (pristine CNFs and CNF/Mag) present a very similar percolation threshold indicates that the adsorbed magnetite does not appreciably alter the dispersion process of the filler. In similar polymer/conductor disordered systems, electronic conduction has been explained in terms of fluctuation-induced tunneling[78–80]. In this theoretical framework, electron transfer through the insulating gaps between conducting fibers or clusters, is what determines the bulk electrical conduction. Conductivity is then given by the minimum separation distance between CNFs, or the conductor-conductor junction width, and theory predicts $\log \sigma \propto r \cdot \xi^{-1}$, where r is the distance between the centerlines of adjacent conductors and ξ is the characteristic tunneling distance[81].

In consistency with the work of Connor *et al.*[78], the gap width of filler-filler junctions are proportional to $\phi^{\frac{-1}{3}}$ and as a consequence, $\log \sigma$ should vary linearly with $\phi^{\frac{-1}{3}}$. As shown in the inset of Figure 3.40, a linear variation is observed when $\log(\sigma)$ is plotted against $\phi^{\frac{-1}{3}}$. This suggests that in both systems (composites of CNFs and CNF/Mag) electron conduction indeed occurs through fluctuation-tunneling and that the conduction gap-width in CNF/Mag is similar to that of the composite with pristine CNFs. However, the lower intercept found for the CNF/Mag composites might indicate a reduced junction contact area. It seems that the oleic acid capped magnetite particles adsorbed on the CNF do not modify the contact width, but reduce the surface portion of the fibers or clusters available for electron tunneling. This fact is well in agreement with the TEM observations discussed previously.

II.2.3 Dielectric permittivity and magnetic permeability

II.2.3.1 Composites containing magnetite nanoparticles only

The magnetic permeability of composites containing magnetite nanoparticles is shown

in Figure 3.41. Although the fraction of magnetic inclusions is relatively high (higher than that employed in the ferrite-silica composites, section II.1), neither broad peaks in the imaginary permeability nor magnetic relaxations in the real component are seen, suggesting a poor magnetic activity. Therefore, the wavy trend in both magnitudes was attributed to fluctuations due to the experimental uncertainty. In all cases the real magnetic permeability is close to one and the imaginary part to zero. Nevertheless, it is possible to discern that the composite with the highest $wt\%$ presents a μ' value slightly higher that one and higher than the rest of composites, which could imply that nanoparticle fractions higher than 10 $wt\%$ are needed to observe a change in μ' and obtain an enhanced magnetic response.

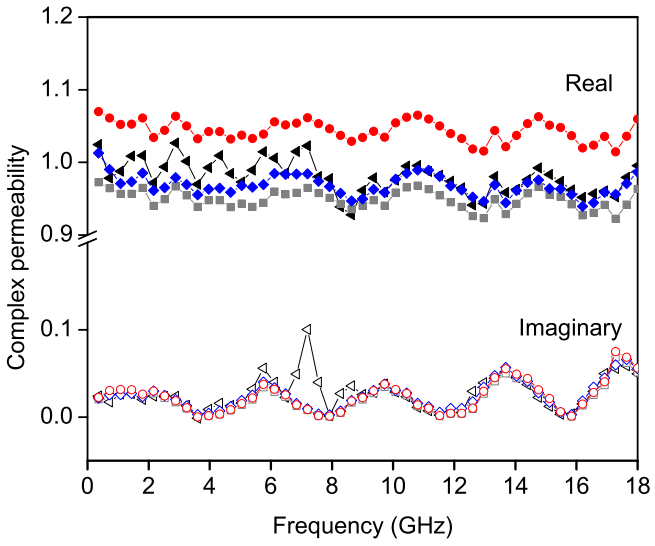

FIGURE 3.41: Complex permeability of the epoxy/Mag composites. Real permeability of composites with concentrations of: 1% (◀), 2.5% (■), 5% (♦) and 10% (●). The symbols of the imaginary components correspond to the ones listed for the real part but as open symbols

The values of real and imaginary permittivity are presented in Figure 3.42. Superimposed over a general decreasing trend, some maxima and minima are seen. This

feature might be related to the sample thickness, due to their poor conductivity and small permittivity magnitude.

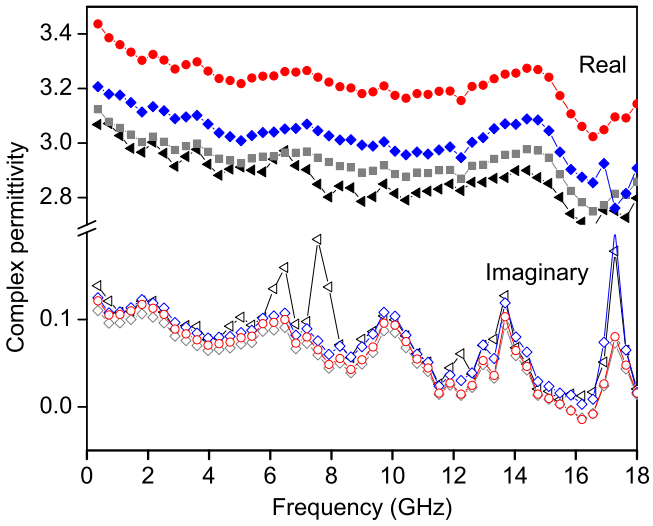

FIGURE 3.42: Complex permittivity of the epoxy/Mag composites. Real permittivity of composites with concentrations of: 1% (◀), 2.5% (■), 5% (◆) and 10% (●). The symbols of the imaginary components correspond to the ones listed for the real part but as open symbols

The effect of the magnetite nanoparticles on the dielectric properties of the composites is small. Only a slight increase in ϵ' with the concentration of magnetite is observed at 1 GHz: from $\approx$ 3, for the neat epoxy, to $\approx$ 3.4, for the Mag 10 $wt\%$. The loss tangent remains constant and very close to zero (0-0.04), for all compositions and frequencies, indicating that losses are negligible. This result reflects a weak interaction with the electric field and between the electric dipoles of nanoparticles, which can be addressed to the lack of interconnectivity between the nanoparticles, even for the sample with the highest magnetite content. This is in reasonable agreement with the work of Ali-zade[82], which states that for magnetite particles with a similar size, below volume fractions of *ca.* 0.03 electric dipole interactions between nanoparticles can be neglected. In addition, the percolation limit reported for hard-core spherical particles of $\approx$ 10 nm diameter is around 16 $vol\%$[83–85], which is far above the maximum

amount used in this work ($\approx 5\ vol\%$). Therefore, assuming a purely real permittivity, the effective permittivity of our epoxy/magnetite composites should follow a simple rule of mixtures. Among the equations that have been proposed for non-interacting systems of particles below the percolation limit [86], we have selected the Cummings equation due to its simplicity:

$$\log(\epsilon_{eff}) = \sum \phi_i \log(\epsilon_i) \tag{3.7}$$

where ϕ_i and ϵ_i are the volume fraction and permittivity of the *i-th* component. The calculated value is 38 ± 3 within the frequency range of $3.6 \times 10^8 - 81.7 \times 10^{10}\ Hz$, in excellent agreement with the reported values within a narrower frequency range [87].

II.2.3.2 Composites of CNFs and CNF/Mag

The real permittivity (ϵ', stored energy) of systems that are composed by dielectric/-conductor phases is a direct measure of the relationship between polarization and the applied field [88]. In contrast, energy loss mechanisms are represented by the imaginary permittivity (ϵ''), which represents both the conduction loss and the dielectric loss [89]. The conduction loss is mainly associated to the materials ohmic resistance, while the dielectric loss is generated by the induced polarization when the AC field interacts with the material. In the latter case, the loss in the GHz range can be mainly related to electric dipolar polarization rather than to electron or ion polarization [90], and in CNT/polymer composites is associated to the migration and accumulation of charge at the CNT/polymer interfaces (Maxwell–Wagner–Sillars polarization [91]).

To be able to contrast the ohmic and the dielectric behavior of our samples, we have analyzed both ϵ' and the AC-conductivity ($\sigma' = 2\pi f \epsilon''$) as shown in the double logarithmic plots of Figure 3.43. In a general view, composites show decreasing and increasing tendencies with frequency for both ϵ' and σ', respectively.

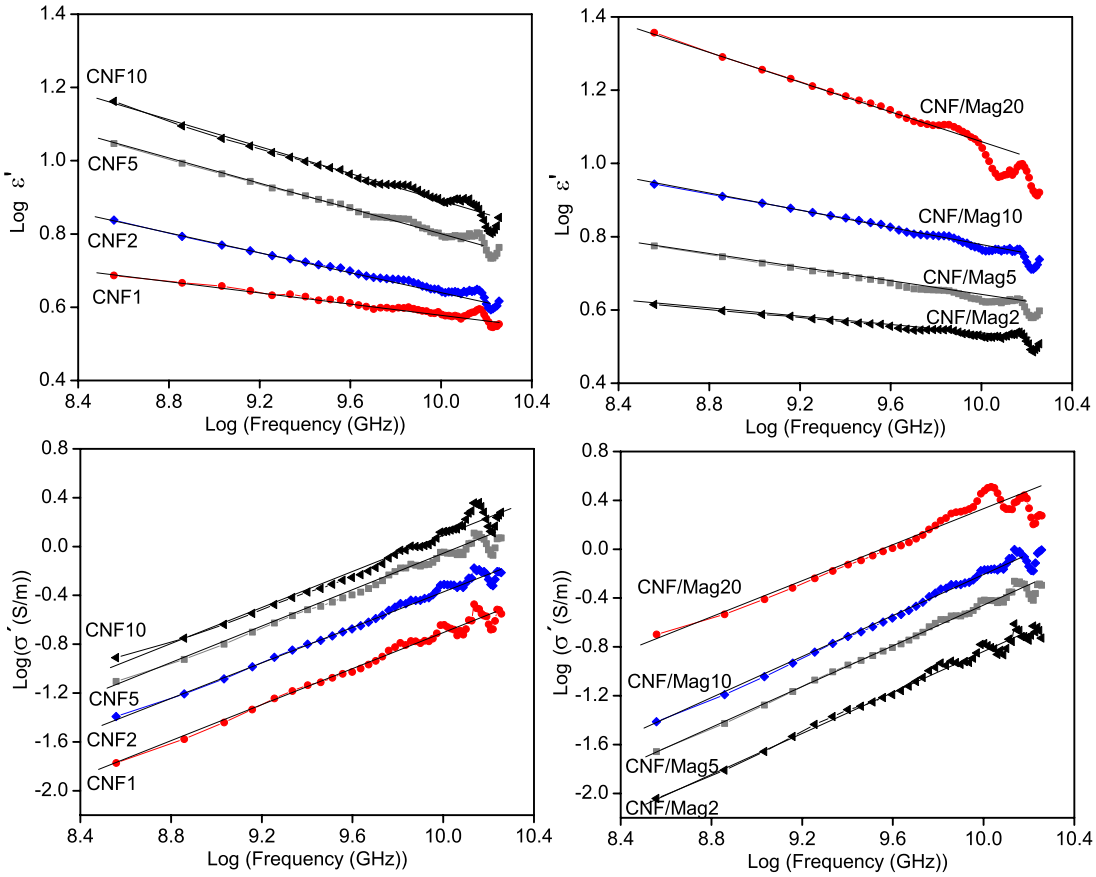

FIGURE 3.43: Double logarithmic plots of the real permittivity ϵ' (top plots), and conductivity σ (bottom plots) for: Epoxy/CNF (left), and Epoxy/CNF/Mag composites (right). Mass compositions are indicated in the insets. Lines correspond to the best linear fits of the initial portion of the curves

The frequency (f) dependence of σ' and ϵ', is typically explained in terms of the percolation theory of fractal structures[78,92], which considers $\sigma \propto f^x$ and $\epsilon \propto f^{-y}$, and where the exponents follow the general relation $x + y = 1$[93,94]. Linear fits of the first initial portions of plots in Figure 3.43 (a and b) yielded the following averaged values for both CNF and CNF/Mag systems: $x = 0.81 \pm 0.09$ and $y = 0.12 \pm 0.06$, well in agreement with the theory.

However, a further insight in the individual σ' revealed that CNF/Mag composites present slightly higher x values than those of their pristine CNF analogues, suggesting that conductivity of CNF/Mag might be changing with frequency in a greater extent.

Meanwhile, with regard to the y value, it can be seen that the frequency-dependent tendency of ϵ' starts at smaller $wt\%$ in CNFs than in CNF/Mag.

As illustrated in Figure 3.44, dielectric/conductor composites above percolation can be represented as the equivalent circuit formed by a capacitor (C) connected in parallel with a resistor (R)[95]. The capacitor represents those conductor/conductor junctions with non-negligible interparticle gap, thus having dielectric polymer regions within them prone to polarization. In accordance, the resistor represents the percolation paths formed by conductive inclusions with negligible interparticle gap, which present a non-frequency dependent conductivity (ohmic loss).

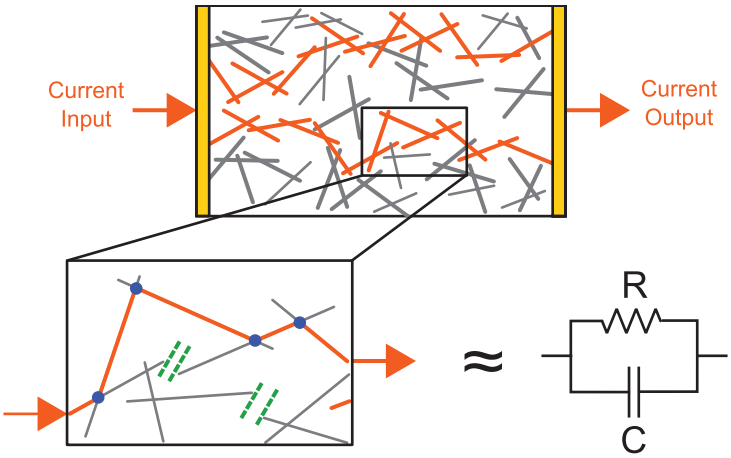

FIGURE 3.44: Illustrative simplification of the equivalent circuit model for describing the permittivity and the AC-conductivity dependence on frequency[96]

When such equivalent $R-C$ circuit is subjected to an AC-field, the conductivity can be expressed as the complex admittance (Y)[97], which determines, in analogy, how easily the circuit allows current to flow through its $R-C$ elements. The change of Y with frequency (f) can be expressed as a function of the resistance (R) and the capacitance (C) of the corresponding elements of the equivalent circuit as[97]:

$$Y = Y' + jY'' = \frac{1}{R} + j2\pi fC \tag{3.8}$$

Capacitive, or dielectric, losses are those that change with frequency, while resistive, or ohmic, losses do not depend on it[98]. At high enough frequencies, the potential energy needed for electrons to tunnel from one delocalized site to another decreases. In consequence, the impedance associated to the capacitive element diminishes and it contributes to lower the resistance of the bulk material to the transmission of electric charge. This implies that Y is enhanced due to favored spatial displacement of polarizable charges in the capacitive element. The crossover frequency (ω_0), at which conductive composites start to show the influence of capacitors, is related to the frequency of the applied field and to the closest conductor-conductor distance[99]. Thereby, ω_0 is higher for composites in which adjacent CNTs are closer to each other, or, in other words, when the resistive element dominates.

Since the AC-conductivity arises from $\sigma' = 2\pi f \epsilon''$[100], it has the contribution of both dielectric and ohmic losses indistinctly. As here the frequency is considerably high (GHz), none of the composites show a clear slope tendency change (ω_0). However, DC-conductivity measurements (II.2.2) showed that ohmic losses were lower for samples containing CNF/Mag, therefore, their slightly higher x values could suggest that dielectric losses might be superior in these samples than in those containing only CNFs.

The slope differences observed in ϵ' vs. f plots (y values) can be analyzed through the behavior of the capacitive element of the equivalent circuit. The capacitance, or the ability of storing charge, is enhanced whenever the distance between the conductors forming the capacitor decreases and when polarization between them is strong. Since ϵ' is a direct measure of the polarization, its decreasing trend with frequency, for all compositions, is a consequence of dipoles not being able to follow the alternating electric field at high frequencies[88].

On the other hand, when the $wt\%$ of conductive inclusions increases in composites, the average conductor-conductor distance decreases and the capacitance is enhanced. At low $wt\%$, the capacitance is almost unaltered, as the conductive inclusions are not close enough therefore, ϵ' does not show a strong dependence with frequency. As the

$wt\%$ increases, the conductor/polymer/conductor gaps are reduced and suffer strong polarization processes (Maxwell–Wagner–Sillars polarization[91]), which in turn are traduced in higher capacitances and enhanced ϵ' values. The frequency-dependent tendency of ϵ' starting at smaller $wt\%$ in CNFs than in CNF/Mag, might corroborate that magnetite does not modify the contact width between fibers, but probably reduces the availability of surface portions prone to form contacts. Thereby, when CNF/Mag composites start to present the frequency dependent behavior, polarization is stronger than in CNFs, as evidenced by the higher y value of CNF/Mag 20 $wt\%$ in comparison to CNF 10 $wt\%$. This observation, in accordance to the enhanced dielectric losses found in CNF/Mag composites, might validate the assumption that magnetite nanoparticles confer additional dielectric mechanisms of energy dissipation.

The magnetic permeability of composites is shown in figure Figure 3.45.

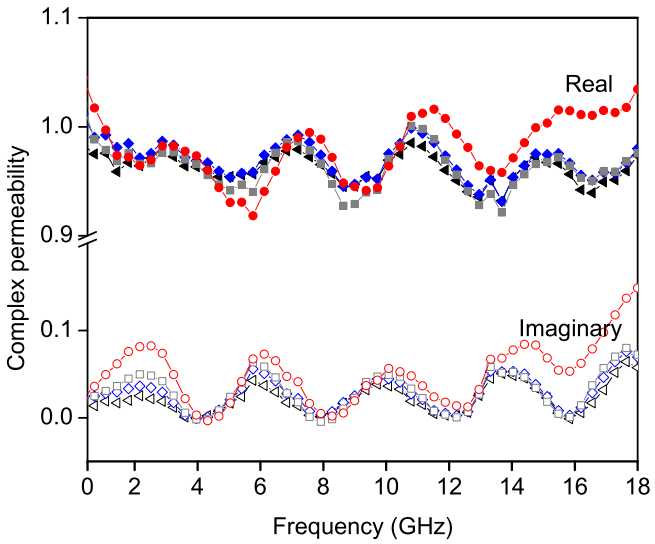

FIGURE 3.45: Complex permeability of the epoxy-CNF/Mag composites with concentrations of: 1% (◀), 2.5% (■), 5% (◆) and 10% (●). The symbols of the imaginary components correspond to the ones listed for the real part but as open symbols

In contrast to the electric permittivity, the magnetic permeability showed real and imaginary components close to one and zero respectively. Neither broad peaks or

relaxations nor enhancements in comparison with epoxy-Mag composites are seen, suggesting again a poor magnetic activity.

II.2.4 Shielding efficiency

The SE behavior of all samples can be represented by that observed for the higher compositions of both systems (CNF10 and CNF/Mag20), which showed the highest SEs. As shown in Figure 3.46 a, the total SE (SE_T), as well as the absorption (SE_A) and reflection (SE_R) components, increase steadily with frequency. The most important feature in this graph is that above 3-4 GHz, the main contribution to SE is absorption (SE_A), while reflection (SE_R) remains very low. The absorption contribution increases with frequency, reaching a maximum value of 18 dB for CNF/Mag 20 and 12 dB for the one that only contains 10 $wt\%$ of CNFs. Concerning the reflection component, typical multiple maxima related to reflections from the output interface of the slab are observed at low frequencies. As earlier addressed (see section II.1.2, Figure 3.35), these maximum and minimum dips appear when samples are electromagnetically thin or, in other words, when slabs are thinner than their skin depth. In these composites, since conductivity increases with frequency and therefore the slabs become electromagnetically thick at some point, these dips are only observed at low frequencies. Above 4 GHz, the reflection component remains at a very low level (~ 1 dB).

The higher attenuation of CNF/Mag composites in comparison to those containing equivalent loads of CNFs, suggests a synergistic shielding behavior when magnetite particles and CNFs are combined. Indeed, Figure 3.36 shows that the absorption coefficient, non-dependent on the sample thickness ($dB \cdot cm^{-1}$), increases in a higher extent for samples containing both magnetite and CNFs, especially for the highest contents. In detriment of electrical conduction, the presence of magnetite over the fibers might decrease the total contact area for electron diffusion between CNFs (see section II.2.2, Figure 3.40), however, as it became apparent in the discussion of dielectric results, the combination of CNFs with magnetite nanoparticles might also induce an additional

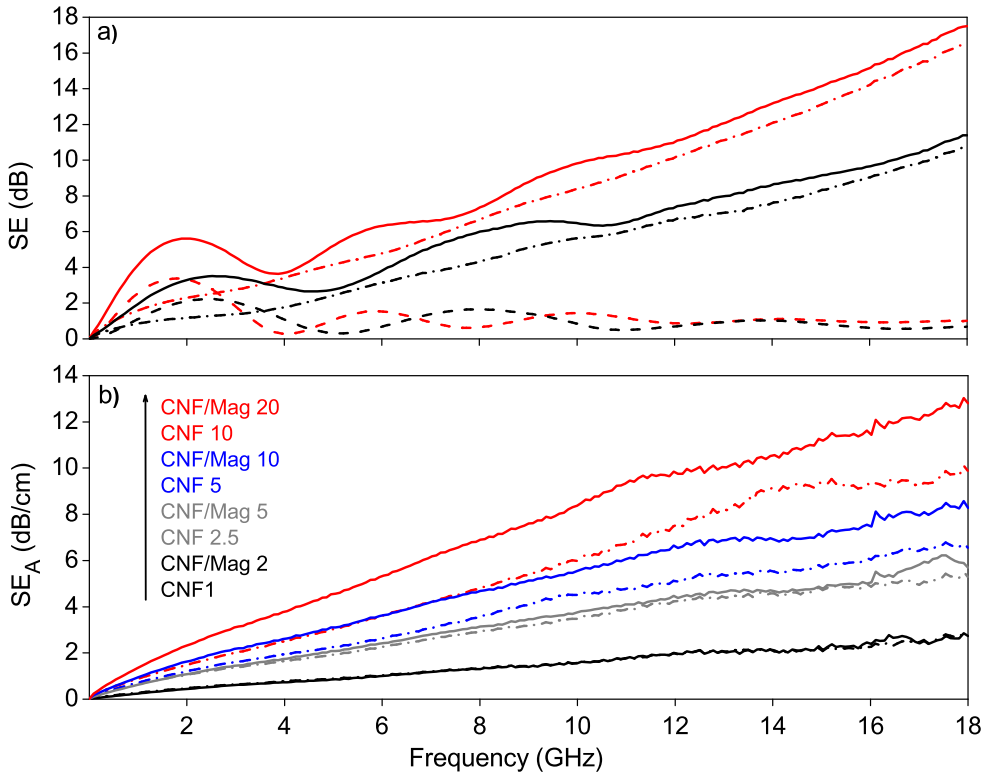

FIGURE 3.46: a) Electromagnetic shielding efficiency of CNF10 (black) and CNF/Mag20 (red) composites showing the total shielding efficiency (SE_T, solid lines), absorption shielding (SE_A (dash-dots) and reflection shielding (SE_R, dashes) components for both samples. Thickness of specimens: 13 *mm*. b) Absorption coefficients for CNF (dash-dots), CNF/Mag (solid lines) composites with the compositions indicated in the inset

energy dissipation mechanism. The influence of the magnetic character of the particles in this observation remains unclear, since $\mu' \approx 1$ and $\mu'' \approx 0$ in all cases. It is therefore suggested that the incorporation of magnetite nanoparticles may not turn the fibers magnetically active enough, but might be responsible of an enhanced interfacial polarization process [98]. Composites with nanoparticles (CNF/Mag) present an increased number of interfaces, hence their higher ϵ' values, which can polarize and activate this new absorption path of EM shielding.

II.2.5 Power balance: reflectivity

If most of the incident EM power is reflected at the surface of conductive shields, these cannot be considered efficient EMI absorbers, even if these present high SE_A values. Since the absorption component of the SE, equals to $SE_A = 10\log\left(\left(P_I - P_R\right)/P_T\right)$ and thereby, expresses the relative attenuation of EM power that has not been previously reflected at the input interface of slabs[101,102], in order to determine if our conductive composites can be employed as EMI absorbers it is necessary to evaluate the absolute P_A, P_R and P_T values (see section 2.3). Absolute power values are related to the direct outputs of the characterization equipment (S-parameters) and give complementary information about reflection that inherently occurs when EM waves strike conductive surfaces. The absolute power balances of composites that showed the highest conductivity values thus, having the highest CNF or CNF/Mag content, are shown in Figure 3.47.

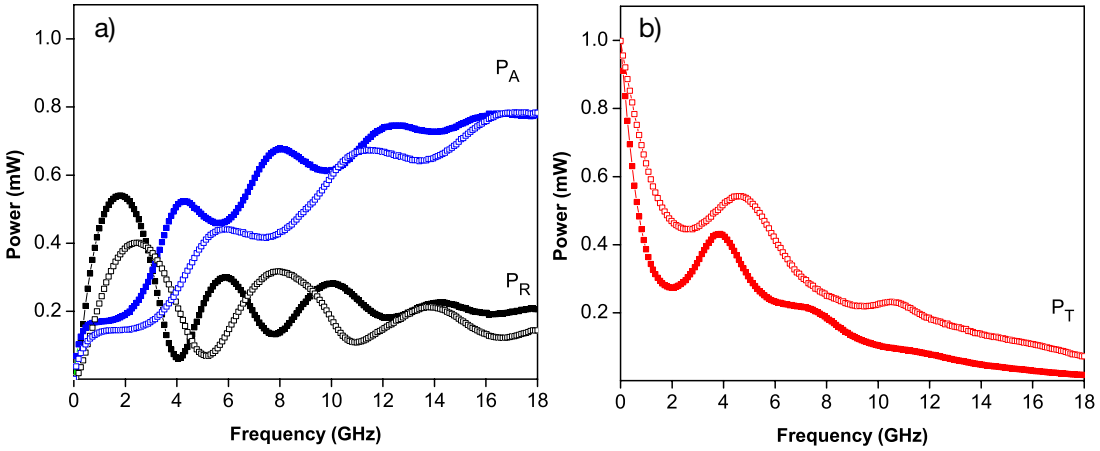

FIGURE 3.47: (a) Absorbed (P_A), reflected (P_R) and (b) transmitted (P_T) power of CNF10 (open symbols) and CNF/Mag20 (full symbols)

As observed in Figure 3.47 a, there are only slight differences in the absorbed powers of both samples. These are due to differences in the reflected power. For example, at 17 GHz, the reflected power of sample CNF is lower than that of CNF/Mag but the absorbed power is the same for both samples. Although this result may appear

to contradict results of Figure 3.46, in which CNF/Mag samples consistently showed higher absorption than CNF samples, it merely indicates that less energy is entering into the sample. Thereby, less energy is being absorbed. The effect of magnetite on the CNF/Mag composite can be clearly seen in Figure 3.47 b, where the transmitted power is considerably lower for CNF/Mag 20 than for CNF 10 therefore, assuring EM waves are able to penetrate into our CNF and CNF/Mag composites for then being dissipated through absorption.

II.3 COMPOSITES OF POLYMER-INFILTRATED SCAFFOLDS

Since the SE is enhanced with conductivity and the aspect ratio of nanocarbons, CNTs can lead to composites with higher SEs than those having CNFs. However, due to the high tendency of CNTs to form agglomerates, adequate conductivities to attain high SEs ($\geq 20\ dB$) are normally achieved only with high CNT loads.

3D-scaffolds of CNTs were prepared with the purpose of increasing the conductivity and reducing the fraction of CNTs in composites. In all cases, scaffolds showed densities lower than 0.07 $g \cdot cm^{-3}$, which indicates that CNTs are forming a percolating network within a large macroscopic volume. The large free volume of these hierarchically assembled CNT-scaffolds enabled infiltration with an epoxy resin to obtain the nanocomposites discussed below.

II.3.1 General characteristics

II.3.1.1 Morphology of the infiltrated scaffold composites

Figure 3.48 shows representative images of the composites prepared through infiltration of scaffolds containing magnetite-decorated CNxNTs (CM3, CM6) and non-decorated CNxNTs (C3 and C6).

In addition, the morphology of the annealed (360 $°C$) and infiltrated CM6 scaffold (CM6T) was also checked to assure the structure did not collapsed with the thermal treatment (Figure 3.49). The transversal sections of all composites indicate original structures were preserved upon the infiltration, since the walls of scaffolds (black regions) show the same morphology than the non-infiltrated structures (see sectionI.3.2, Figure 3.19 and Figure 3.18).

The surface of composites shows a different fracture in the walls of scaffolds than in those zones where there is only polymer (Figure 3.48). Epoxy resins are in general brittle, and their cryogenic fracture results smooth and clean. In these composites it is

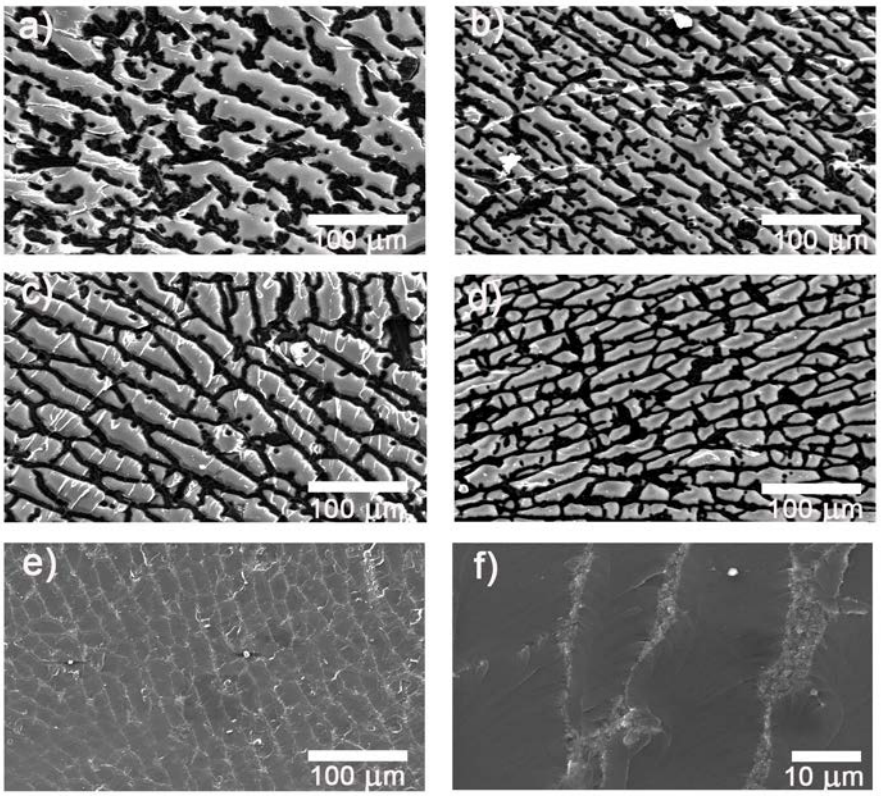

FIGURE 3.48: SEM images of the infiltrated composites: a) C3, b) C6, c) CM3, d) CM6. e) and f) representative lower- and higher-magnification images to show the effect of the CNT load in the fragile fracture of the matrix

observed that CNxNTs in the walls of scaffolds somehow restrain the resin's fragility, since a disruption of the fragile fracture is seen at these zones. Besides, the lack of voids at the scaffold/resin interface suggests a good interaction between CNxNTs and the epoxy matrix.

II.3.1.2 Thermal characterization of C3, CM3, C6 and CM6

The Tg of composites with decorated and non-decorated nanotubes (C3, CM3, C6 and CM6) did not decrease in comparison to the neat epoxy. Composites with the highest nanofiller loads (C6 and CM6) showed slightly higher Tg values when compared to the

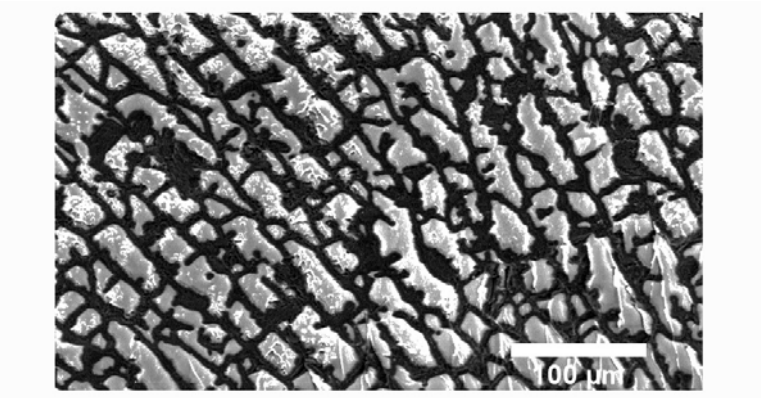

FIGURE 3.49: SEM of the composite with the thermally treated scaffold (CM6T)

neat resin (Table 3.8), which suggests that interactions at the scaffold-matrix interface are not worsening the properties of the resin.

TABLE 3.8: Glass transitions temperatures (Tg) of the composites

Scaffold	**HDGEBA**	**C3**	**CM3**	**C6**	**CM6**
$\boldsymbol{Tg}$, $\boldsymbol{°C}$	79	79	79	80	81

The thermal stability of composites was evaluated by TGA (Figure 3.50). The degradation profiles of all composites are very similar to that of the neat epoxy, which starts degrading at $\sim$320 $°C$. For composites, after the first weight loss (300-360 $°C$), it appears that the degradation of CNxNTs (decorated and non-decorated) is coupled to the degradation steps of the epoxy resin, occurring at 400 and 562 $°C$. In the case of composites of scaffolds containing non-decorated CNTs (C3 and C6) the ultimate degradation step occurs at almost the same temperature than for the epoxy. suggesting that the thermal stability of composites is not severely modified by the addition of the filler. In the case of composites having magnetite-decorated CNxNTs (CM3 and CM6) this last degradation step is shifted towards lower temperatures when compared to the neat epoxy and to composites with non-decorated CNTs. This observation is consistent with the TGA analysis made for the non-infiltrated scaffolds (see section I.3.3, Figure 3.21).

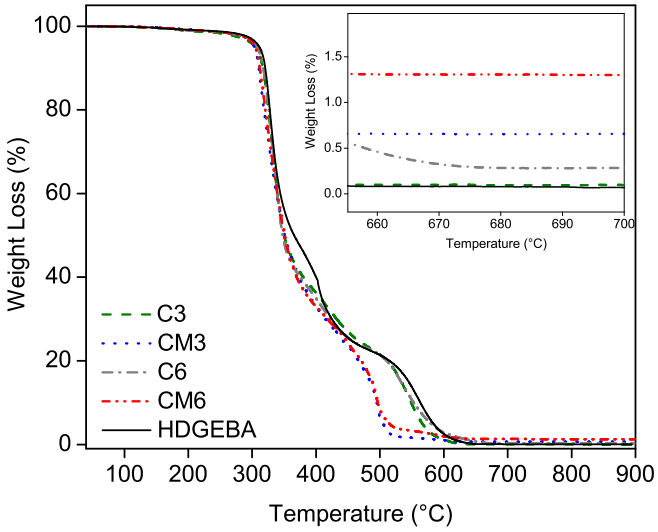

FIGURE 3.50: TGA of the composites (black) and the neat epoxy resin (red): a) C3, b) CM3, c) C6 and d) CM6

TGA results of maximal degradation rates and residual masses are summarized in Table 3.9. In all cases $M_{R\%}$ is extremely small. Although this residual mass can only correspond to original $wt\%$ of magnetite in CNxNTs (for CM3 and CM6) or to the original amount of catalyst residue (for C3 and C6), and thereby the $wt\%$ of CNxNTs or CNxMag in composites can be known, it would be extremely imprecise to recalculate their $wt\%$ in the composites through these $M_{R\%}$ values.

TABLE 3.9: Composite's residual mass ($M_{R\%}$) and maximal degradation rates (T_m) of the three major degradation steps observed in the TGA curves

Scaffold	**C3**	**CM3**	**C6**	**CM6**
$\boldsymbol{T_{m\ 200-400}}$, $\boldsymbol{°C}$	331	317	332	317
$\boldsymbol{T_{m\ 400-500}}$, $\boldsymbol{°C}$	422	498	412	493
$\boldsymbol{T_{m\ 500-700}}$, $\boldsymbol{°C}$	544	599	534	590
$\boldsymbol{M_{R\%}}$	0.009	0.66	0.27	1.3

Nevertheless, SEM images allow us to assume that in all cases, scaffolds are totally infiltrated by the resin. Thus, if the void fraction of scaffolds is completely replaced by the resin, it implies that the $wt\%$ of fillers in composites should be similar than

the initial 3.4 and 6.7 $wt\%$ of CNxNTs and CNxMag in the primary dispersions. In addition, the increase of volume when water (in primary solutions) is converted into to ice (in cryogels) and the higher density of the resin ($1.12\ g \cdot cm^{-3}$) when compared to that of ice, enables to assume that in any case, the $wt\%$ of CNxNTs or CNxMag in composites is lower that in the original dispersions (3.4 $wt\%$ for C3 and CM6 or 6.7 $wt\%$ for C6 and CM6).

II.3.2 DC-electrical conductivity

DC-conductivity was measured along the longitudinal axis (freezing direction) of each scaffold composite (Table 3.10). Conductivity increases with the $wt\%$ of nanotubes ($CM3 < CM6$ and $C3 < C6$), since there are more charge transporters available for conduction. In addition, the conductivity of CM6T is glaringly higher than that of CM6. This confirms that with the thermal treatment of CM6, interconnections between adjacent CNTs were enhanced, probably due to the partial conversion of CHI into amorphous carbon.

Conversely, although C3 and C6 have a greater net amount of nanotubes, they present conductivities around one order of magnitude lower than CM3 and CM6.

TABLE 3.10: DC-conductivity of CNT-scaffold composites

Scaffold	**C3**	**C3M**	**C6**	**CM6**	**CM6T**
$\boldsymbol{\sigma\ (S \cdot m^{-1})}$	0.02	0.13	0.31	1.74	7.36

A plausible explanation could be that magnetite nanoparticles favor CNT interconnections at some extent. However, it was observed that the primary dispersions of decorated CNxCNTs did not show agglomerates, unlike those of non-decorated CNxCNTs, which showed poorly disaggregated nanotube bundles.

CNT/polymer composites present a bulk DC-conductivity that is limited by the resistance at the conductor/conductor junctions (R_{jct}). Given two extreme cases: a) x number of CNTs with x number of single-tube junctions and b) two rigid bundles of

x number of CNTs, having only one junction (Figure 3.51), the bulk conductivity will be limited by the R_{jct} between single CNTs (a) or the Rjct between bundles (b) [103]. For two overlapping bundles, the bulk resistance would equal R_{jct}. Meanwhile, for x number of tubes with x number of parallel single-tube junctions, the resistance would be $(1/x)\ R_{jct}$. Thereby, samples containing CNT bundles would present lower conductivities than those containing well-dispersed CNTs. Therefore, the worst dispersibility of non-decorated CNxCNTs might be the cause for C3 and C6 showing lower conductivities than CM3 and CM6.

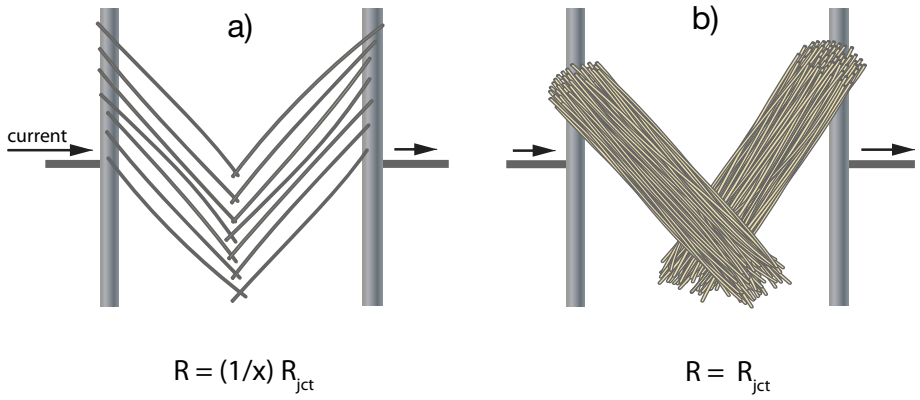

FIGURE 3.51: Schematic illustration for explaining the percolative DC-electrical conductivity of CNT/polymer composites with: a) x single-tube junctions and b) two bundles with one junction [103]

II.3.3 Magnetic permeability and electric permittivity

Real and imaginary permittivities of all composites are shown in Figure 3.52 a and b. As previously observed for CNF/polymer composites (section II.2.3), both systems (with magnetite-decorated and non-decorated CNTs) present higher ϵ' and ϵ'' when the load of CNTs increases. In the case of ϵ' this is a direct consequence of a higher number of interfaces prompt to polarization (Maxwell–Wagner–Sillars effect). For ϵ'', it is due to the reduction of the average distance between adjacent CNTs, which in turn implies higher dielectric and ohmic losses. Therefore, the ϵ'' tendency is in well agreement with

the DC-conductivity of samples. In addition, slopes of the double logarithmic plots in Figure 3.52 c, reveal how σ' presents a more capacitive-like behavior (for samples with lower CNxNTs $wt\%$: C3 and CM3), which start to change to a more resistive comportment when the $wt\%$ of CNxNTs increases (C6 and CM6).

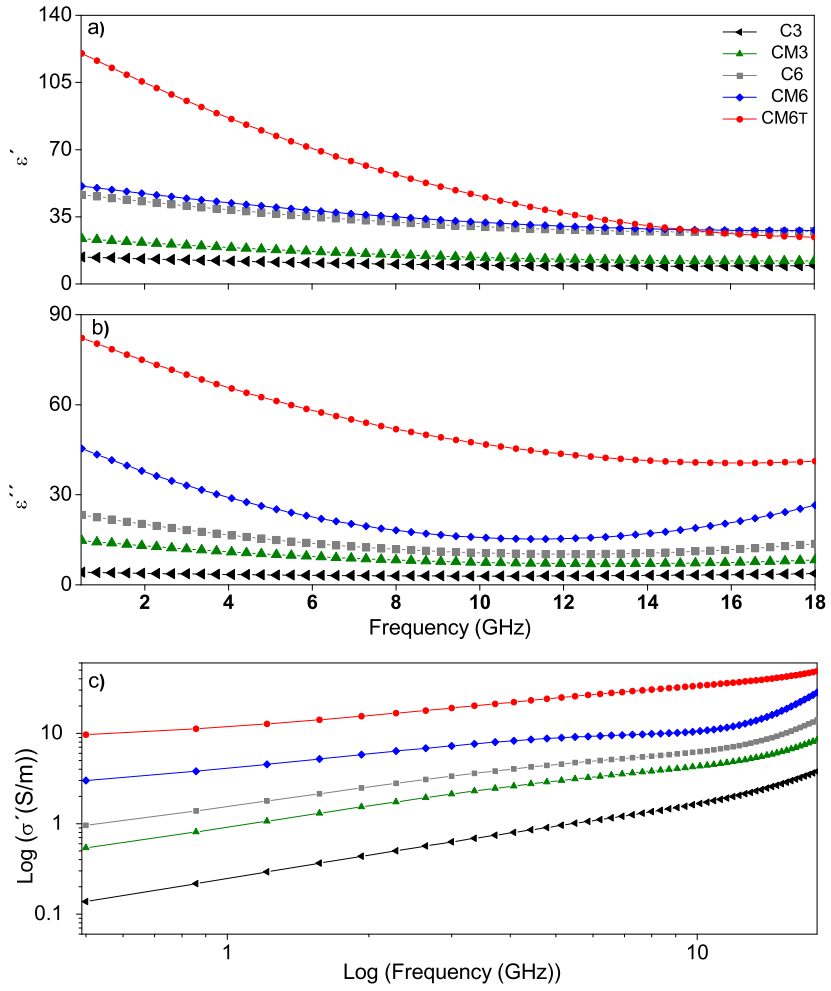

FIGURE 3.52: a) Real permittivity (ϵ'), (b) imaginary permittivity (ϵ'') of the composite's scaffolds and (c) double logarithmic plots of the AC-conductivity vs. frequency

However, none of the samples presents a purely resistive response and in addition, it is difficult to discern if magnetite-containing samples show stronger dielectric losses

(higher ϵ'' and σ') than their non-decorated analogues, due enhanced interfacial polarization or due to the higher DC-conductivity (ohmic loss) that they present. In addition, CM6T presents both higher ohmic and dielectric losses than CM6, which might be a consequence of replacing the dielectric polymer within CNTs by a more lossy material (amorphous carbon).

When comparing composites with equal $wt\%$, it can be seen that, although samples containing magnetite (CM3 and CM6) are substantially more conductive, they present very similar ϵ' values than C3 and C6, respectively. C3 and C6 have a higher net amount of CNxNTs, which could imply an enhanced polarization degree, however these samples showed strong CNT agglomeration, which is in detriment of polarization. CM3 and CM6 yet have the contribution of a significant amount of polarizable interfaces, since magnetite nanoparticles are decorating the surface of CNxNTs. Therefore, similar ϵ' values suggests that scaffold's structure, which is the only common feature between C3 and CM3 or C6 and CM6, might prevail over the rest of factors affecting the value of ϵ' in composites.

The dielectric behavior found in aerogels and foams, might be extended to that of CNT-scaffolds due to their high porosity. Aerogels present high volume fractions of void areas, hence their effective permittivity (ϵ_{eff}) is limited to the low dielectric constant of air within their structure[104]. Although there are several factors altering the effective permittivity of composites, it has been corroborated that almost all phase combinations, geometries and distributions, are circumscribed between the less restrictive limits (Wiener bounds), which are given by[105]:

$$\epsilon_{eff,max} = \Phi_1\epsilon_1 + \Phi_2\epsilon_2 \tag{3.9}$$

$$\epsilon_{eff,min} = \left(\frac{\Phi_1}{\epsilon_1} + \frac{\Phi_2}{\epsilon_2}\right)^{-1} \tag{3.10}$$

Where Φ represents the volume fraction, ϵ the permittivity and the subscript numbers correspond to each of the two constituents of the composite. For materials containing

high volume fractions of components with low permittivity, the effective permittivity should lay somewhere close to the lowest bound (equation (3.10)) but obviously restricted by the intrinsic permittivity of the filler[106]. Since during the preparation of scaffolds CNTs have been forced to occupy only certain small volumes (densities $< 0.07\ g \cdot cm^{-3}$), the dielectric constant of composites (ϵ') could be restraint by the low dielectric constant of the polymer.

Besides, the volume occupied by the polymer is much higher than that occupied by CNTs. Both factors could limit polarization processes in our scaffold composites, hence an enhanced dielectric loss together with a low dielectric constant value. This hypothesis could contribute to justify the small variation of ϵ' between scaffolds having the same $wt\%$ of either CNxNTs or CNxMag, despite the higher electrical conductivity and dielectric loss of samples containing CNxMag (CM3 and CM6). Indeed, CM3 and CM6 present higher loss tangents (ϵ''/ϵ' ratio) than C3 and C6, respectively, as shown in Figure 3.53. In the case of CM3, ϵ''/ϵ' is even higher than that of C6.

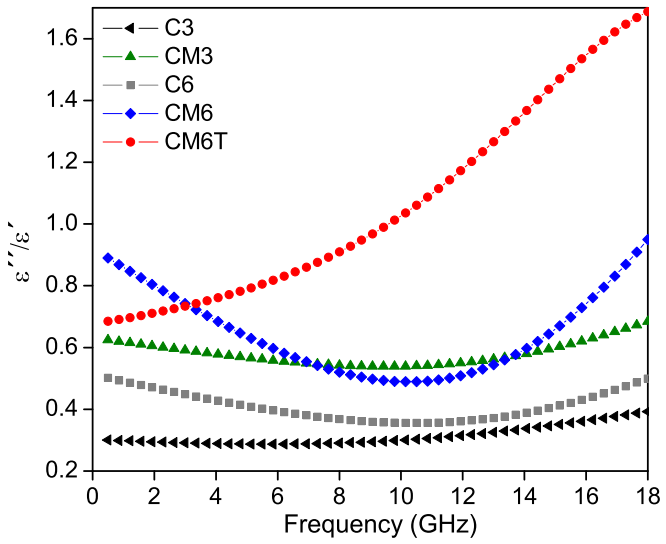

FIGURE 3.53: Dielectric loss tangent ($\tan\delta_E = \epsilon''/\epsilon'$) of the CNT scaffold composites

Both CM3 and CM6 scaffolds presented higher void fractions than their non-decorated analogues (see section I.3.2) and in composites this could be traduced in a higher volume fraction of infiltrated polymer. Thereby, the higher loss tangent of CM3 and CM6 might be taken as a further proof of the limiting effect that low loads of highly interconnected CNTs have in the effective permittivity of composites.

In the case of the thermally treated sample (CM6T), there is an obvious increment in the low-frequency ϵ' value when compared to CM6, suggesting that the polymeric binder (CHI) in the immediacy of CNTs has indeed been replaced by a higher dielectric constant material such as carbon. This change would involve a higher polarization at the capacitive regions, and would increase the magnitude of ϵ', especially at low frequencies, where dipoles are strongly influenced by the alternating field.

With regard to the magnetic permeability, as shown in Figure 3.54, both real and imaginary components of are close to one and zero, respectively, for all composites.

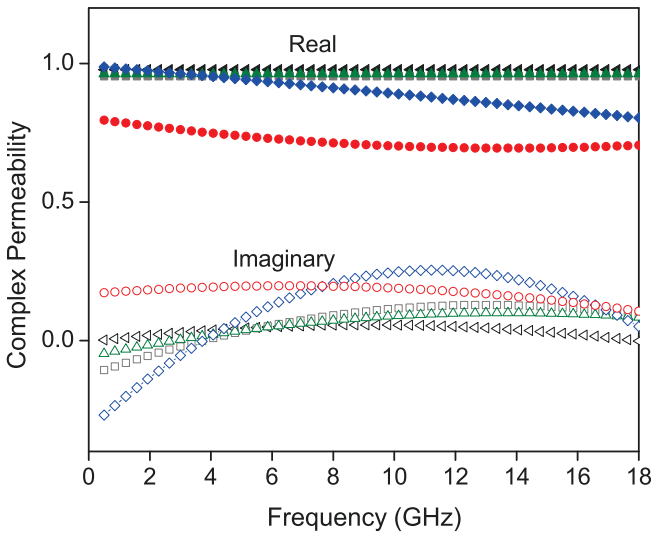

FIGURE 3.54: Complex permeability of the magnetite decorated CNT and pristine CNT scaffold composites: C3 (◀), CM3 (▲), C6 (■), CM6(♦) and CM6T(●). The symbols of the imaginary components correspond to the ones listed for the real part but as open symbols

However, in samples containing the highest magnetite amounts (CM6 and CM6T), μ' and μ'' present certain frequency dependence. It might be possible that the template role of CNxNTs enables magnetite particles to growth closely packed enough to each other to favor certain magnetic loss between them, although further understanding is needed to interpret this observation.

II.3.4 Shielding efficiency

Figure 3.55 shows the total SE (SE_T) of all scaffold's composites over 1 to 18 GHz. Once the incident electromagnetic wave enters into the material, enhanced electrical conduction implicates a better dissipation of energy across sample. Then, in well agreement with both the DC-conductivity and the dielectric loss (ϵ'') observations, SE_T is enhanced with the CNT concentration ($C3 < C6$ and $CM3 < CM6$), it is higher for magnetite-containing samples ($C3 < C3M$ and $C6 < CM6$), it is higher for CM6T than for CM6, and it is enhanced with frequency in all cases.

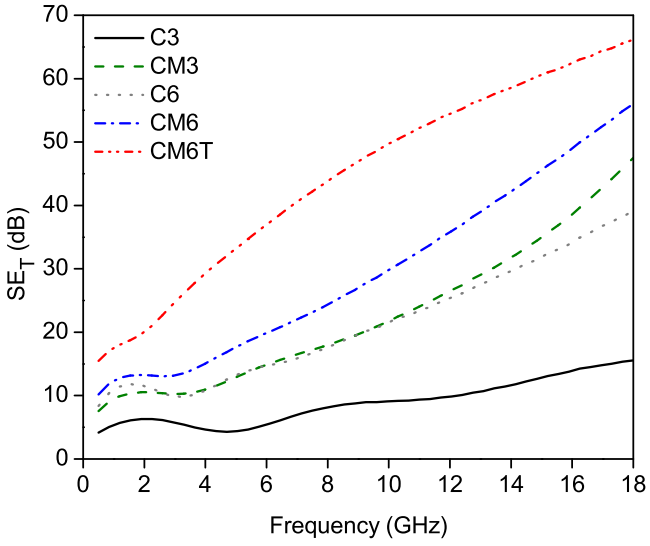

FIGURE 3.55: Total shielding efficiency (SE_T) of the magnetite-decorated CNT (CM3, CM6 and CM6T) and pristine CNT (C3 and C6) scaffold composites

Contributions of absorption and reflection to the total SE are shown in Figure 3.56. SE_R has non-negligible values only at low frequencies, where samples are electromagnetically thin. SE_A in contrast, increases with frequency for all samples, almost at the same extent than SE_T, suggesting absorption is the main EM dissipation mechanism within all composites. Except for the C3 composite, all SE_A magnitudes are comparable or higher than 20 dB for frequencies above 10 GHz, emphasizing that samples are able to block EM energy efficiently. Specially in the case of CM6T, the SE_A is beyond 20 dB for almost all frequencies, which infers that this sample starts to be electromagnetically thick at lower frequencies than the rest.

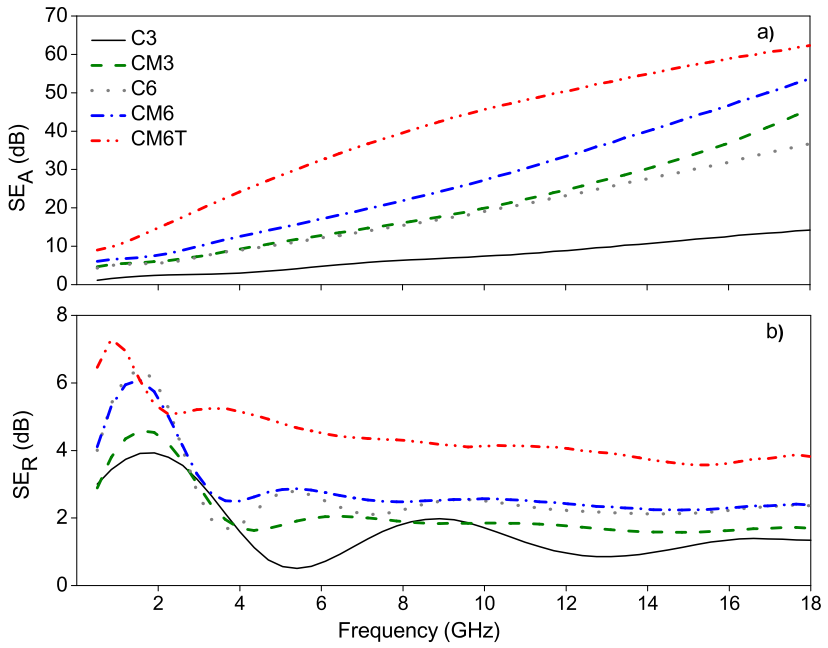

FIGURE 3.56: (a)Absorption (SE_A) and (b) reflection (SE_R) shielding efficiency of the magnetite-decorated CNT (CM3, CM6 and CM6T) and pristine CNT (C3 and C6) scaffold composites

Concerning magnetite containing samples, it is difficult to discriminate if the enhanced SEs of C3M and CM6 arise from the presence and the magnetic character of the particles, or from the enhanced conductivity of composites. Nevertheless, it is significant

that CM3 presents a SE_A comparable to that of C6, if not higher, given that CM3 is less conductive and showed less dielectric loss than C6.

II.3.5 Power balance: reflectivity

Results of the power balance of the scaffold composites are shown in Figure 3.58 and Figure 3.57. In consistency with SE results, the transmitted power is low for all materials and especially at high frequencies. Samples containing higher CNT loads are more reflective (enhanced P_R, $C3 < CM3$ and $C6 < CM6$) as a consequence of a higher electrical conductivity. Therefore, P_A decreases with increasing the CNT content, due to the lower amount of power transmitted inside the sample available for absorption. Power blocked by absorption is higher than that blocked by reflection for all materials above 5 GHz, except for CM6T. In this latter case, the conductivity (7.36 $S \cdot m^{-1}$) might be high enough for being predominantly reflective. In contrast, for the rest of composites, $P_R < P_A$ suggests all materials present limited reflectivity despite being reasonably conductive (C3M and CM6).

This limited reflectivity might also be ascribed to the effect of the structure of scaffolds. Reflectivity depends on the impedance mismatch at the propagating medium (air)/shield interface[107] , and Z_{in} (composites' input impedance) is inversely proportional to the effective complex permittivity of composites. Therefore, the impedance mismatch might be reduced whenever the effective ϵ is reduced[108]. As ϵ accounts for the contributions of both ϵ' and ϵ'', limited reflectivity of conductive samples (high ϵ'') could be only ascribed to the dielectric constant matrix (low) in the global ϵ' of composites. A low global ϵ' could decrease the effective permittivity of composites without sacrificing their dielectric loss (ϵ''). This could justify the similar reflectivity of C3 and CM3 or C6 and CM6, in despite that CM3 and CM6 are more conductive than C3 and C6, respectively.

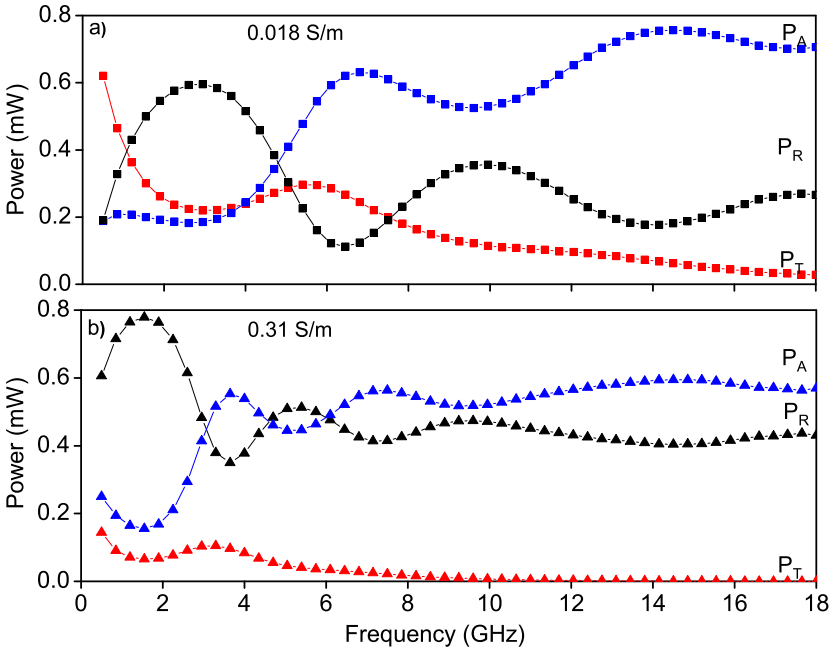

FIGURE 3.57: Power balance showing the power blocked by absorption (P_A, blue) and by refection (P_R, black) and the transmitted power (P_T, red) of composites: a) C3 b) C6

Another factor that should be considered in future investigations, and might also contribute to reduce the impedance mismatch of all samples, is the anisotropic conductivity. Measurements are done along the longitudinal axis of scaffolds (lengthwise to channels) and thus, low reflectivity could be additionally addressed to the low portion of conductive material that is exposed to the impinging EM wave at the first incident plane. Conversely, the smallest dimension that defines the open cellular-like polymer/-conductor surface (elongated, 20-30 μm wide pores) is far smaller than the incident wavelength. Thereby, we are not sure on how this type of non-regular conductivity affects the way that incident EM waves interact with the surface of composites.

Although magnetically permeable inclusions might also contribute to decrease the impedance mismatch of conductive composites, neither the real nor the imaginary

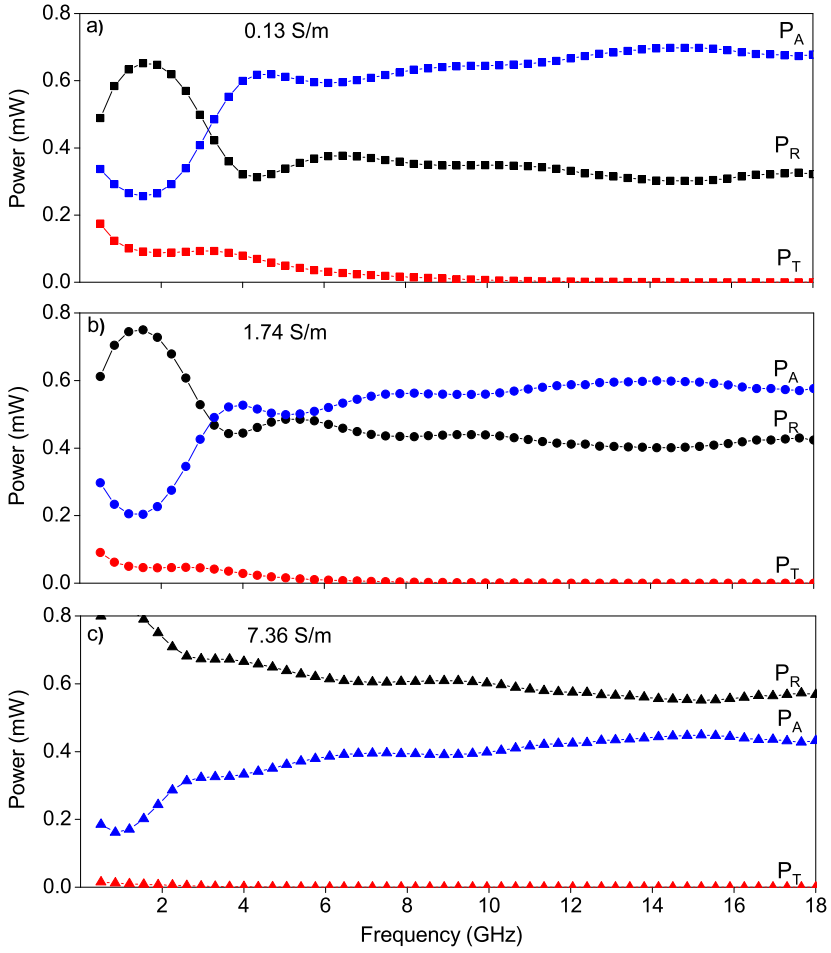

FIGURE 3.58: Power balance showing the power blocked by absorption (P_A, blue) and by refection (P_R, black) and the transmitted power (P_T, red) of composites: a) CM3 b) CM6 and c) CM6T

part of the permeability of CM3 and CM6 (magnetite-containing samples) showed remarkable differences in comparison to C3 and C6 (Figure 3.54). This indicates that the composites' interaction with the EM field is mainly electric, in consistency with most reported works having only conductive, or both conductive and magnetic nanoinclusions. However, for samples containing the highest quantity of magnetite nanoparticles (CM6 and CM6T) it was observed a slight dependency of both μ' and μ'' with frequency

and in addition CM3 presented a SE_A comparable or higher than that of C6. Further research and understanding may be needed in order to give a plausible explanation to these observations.

Concerning absorption, CM3 and CM6 present more constant and higher average P_A values than those of their non-decorated analogues. Furthermore, for C3 and C6 reflection is predominant below 5 GHz and for magnetite-containing samples (CM3 and CM6) reflection dominates only below 3.6 GHz.

From all the above observations it is suggested that composites containing magnetite (CM3 and CM6) boost the wave entrance within their structures in a very similar extent than their C3 and C6 analogues, in despite of being more conductive. Once inside the composite, EM waves are dissipated in a higher extent in CM3 and CM6 composites, due to their higher dielectric and ohmic losses.

II.4 CNT-SPONGES

When the distance between adjacent CNTs decreases, the dissipation of EM energy within the composite is favored. Since in CNT/polymer composites the matrix completely embeds the percolating network, the potential barrier of conduction will be always limited by the CNT/polymer/CNT interfaces.

To analyze the effects of further enhancing CNT/CNT interactions, flexible and tough CNT-sponges were synthesized through a one-pot CVD procedure. Sponges are composed solely by randomly interconnected CNTs, without any polymer binder. In addition, they are ultra-light: their density is as low as 0.02 $g \cdot cm^{-3}$. The EMI shielding properties of these CNT-sponges are described in this section.

II.4.1 DC-electrical conductivity

The DC-electrical conductivity of CNT-sponges was measured to evaluate the bulk electrical isotropy of samples and to discern the interconnectivity degree between adjacent CNTs. I-V plots for the three cross sections of cubic samples (length, width and thickness), are shown in Figure 3.59. The mean electrical conductivity was 278 ± 18 $S \cdot m^{-1}$, in accordance with the reported values of CNT-sponges synthesized under similar conditions [30].

In addition, it can be seen that the resistance along the three cross sections is very similar, which proves that sponges do not have any preferential spatial orientation, as confirmed by SEM images presented on previous sections.

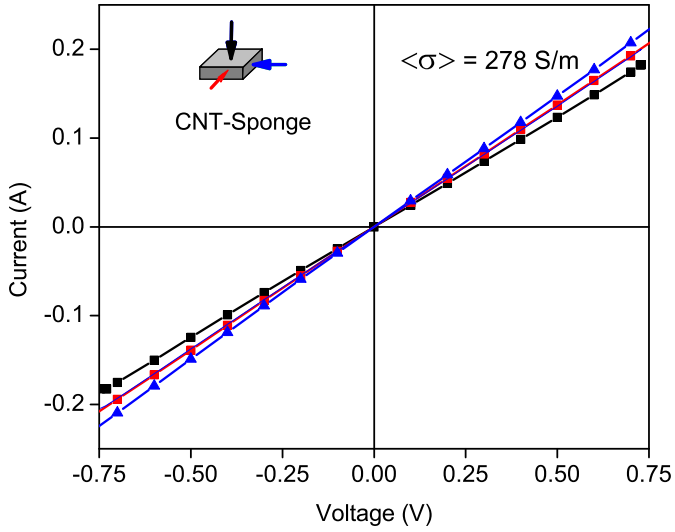

FIGURE 3.59: a) V-I plots for the three faces of CNT-sponge. From the slopes an average conductivity value of $278 \pm 18\ S \cdot m^{-1}$ was obtained

II.4.2 Shielding efficiency

Evaluation of SE_T of the CNT-sponges yields values that depend on the sponge thickness (d). SE_T values for the 2.38 mm thick CNT-sponge slab (Figure 3.60) correspond to 22 dB in almost the entire frequency window (2-18 GHz), being absorption the dominant attenuation mechanism and no difference was observed with the sponge face-orientation.

Since the synthesized CNT-sponges possess extremely low densities, comparisons with other lightweight EMI shields should be addressed using the specific shielding efficiency (SEE), which is given in $dBcm^3 \cdot g^{-1}$. The SEE for CNT-sponges reach values ranging between 550 (for the 1.56 mm thick slab) and 1100 $dBcm^3 \cdot g^{-1}$ (for the 2.38 mm thick slab), which are higher than those reported for a number of systems, as shown in Table 3.11.

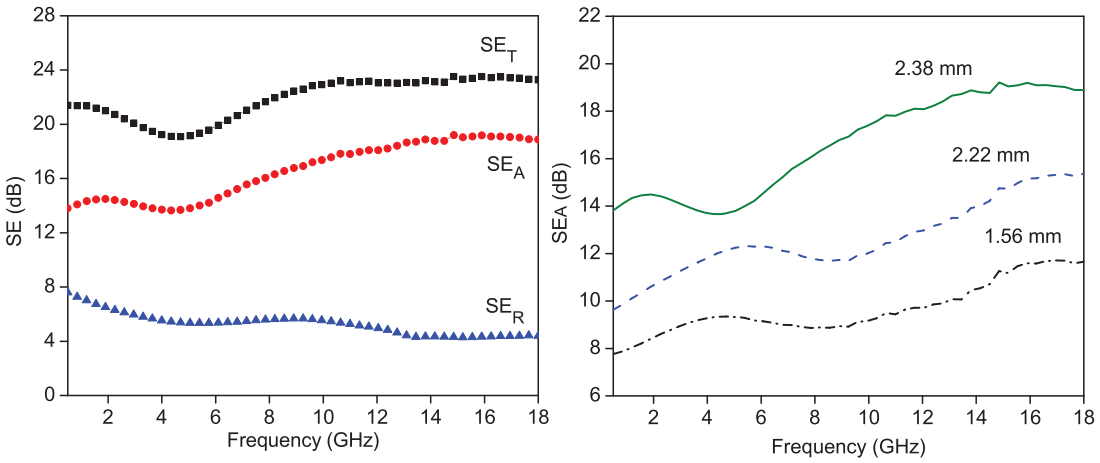

FIGURE 3.60: Contribution of absorption (SE_A) and reflection (SE_R) to the total EMI shielding efficiency (SSE_T) as a function of frequency for a CNT-sponge slab of 2.38 mm (left). absorption shielding efficiency (SE_A) for CNT-sponge slabs with different thickness (right)

TABLE 3.11: Specific shielding efficiency of reported carbon composites

System	**SEE, $dBcm^3 \cdot g^{-1}$**	**Ref**
CNT/polycaprolactone	324	[108]
CNT/polystyrene	33.1	[109]
graphene/PDMS	330	[110]
carbon foam decorated with MWCNTs	163	[111]
graphene/polyetherimide	44.1	[112]
graphene/polystyrene	64.4	[113]
commercial carbon foams	147-176	[114]
CNT-sponge (present work)	1100	

II.4.3 Enhanced conductivity implications

The balance of absolute powers ($P_A = P_I - P_T - P_R$, $P_I = 1\ mW$) for the 2.38 mm-thick CNT-sponge slab is shown in Figure 3.61. The most important feature is that P_I is null for all frequencies, which validates the CNT-sponge as an effective GHz-EMI shielding material. However, it can be seen that for all measured frequencies, power blocked by reflection is higher than that by absorption.

Although some authors have concluded from similar observations that reflection was

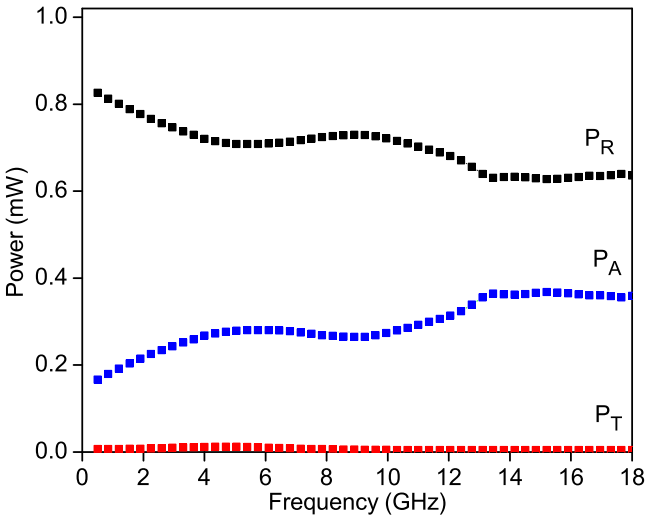

FIGURE 3.61: Power balance of the 2.38 mm thick CNT-sponge slab showing the absolute reflected (P_R), absorbed (P_A) and transmitted (P_T) powers

the main shielding mechanism[115,116], it merely implies that due to the high electrical conductivity of the sample, reflection at the input interface is strong. For this slab thickness (2.38 mm), reflection from the output interface can be neglected at all frequencies because the calculated skin depth, (δ) even at 1 GHz (considering the DC-conductivity of 278 $S \cdot m^{-1}$), is 1 mm. In this situation the SE of the material arises from absorption and reflection mechanisms within the surface (δ), where the shield mostly interacts with the incident EM wave.

Indeed, as shown in Figure 3.62, the CNT-sponge behaves as monolithic conductive shield. SE_A is enhanced when thickness increases, since it is proportional to the ratio of d/δ. Meanwhile, SE_R increases strongly for the thinner slab ($d < \delta$) and for the rest of thicknesses, it tends to converge at 4-5 dB above 10 GHz ($d > \delta$). This implies that the active cross section for shielding is being reduced with frequency, at the same extent than the skin depth.

When analyzing the relative complex permittivity (Figure 3.63), the confirmation that

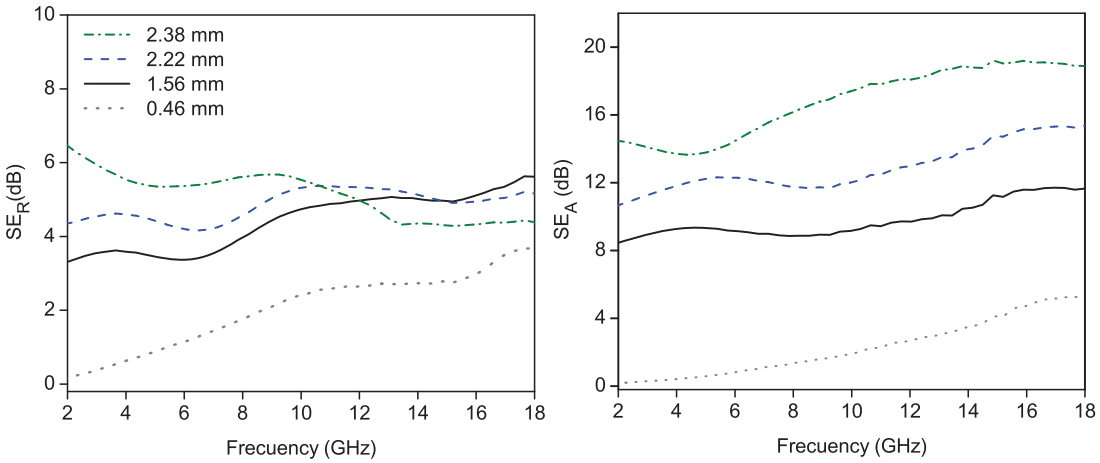

FIGURE 3.62: SE_A and SE_R for different CNT-sponge slab thichnesses

the CNT-network exhibits a high connectivity degree is seen in the dielectric loss (ϵ'') at the mid-low frequency range. ϵ'' is higher than the real permittivity, which indicates that ohmic losses are predominant in the sample. In contrary to most CNT-polymer with high electrical conductivity, resistive loss dominates because the conductive paths lack from capacitive barriers.

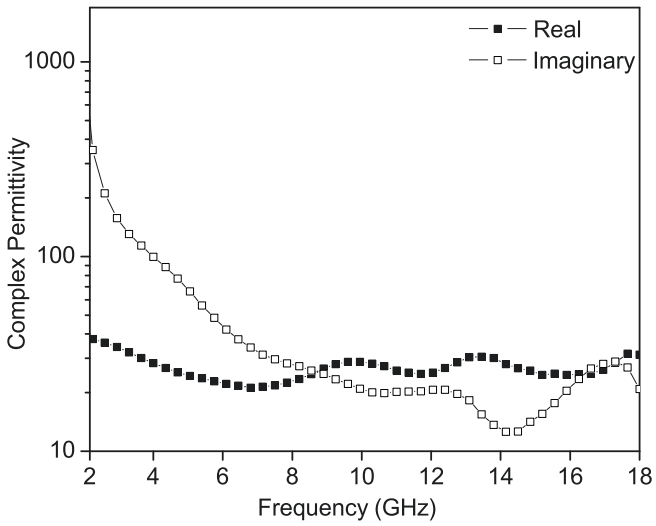

FIGURE 3.63: Complex permittivity of the CNT-sponge

However, at higher frequencies ϵ'' decreases sharply to lower values than those that

one would expect for a nanocomposite in which the DC-conductivity is 278 $S \cdot m^{-1}$. This effect has been previously observed and has been addressed to direct reflection of incident EM waves at the surface of conductive nanocomposites [116,117]. Given the limited penetration of incident EM waves, the measured value of imaginary permittivity (or AC-conductivity: $\sigma' = 2\pi f \epsilon''$) would be also affected by the skin effect and accordingly, should decrease with frequency. In addition, the presence of peaks in the permittivity profiles has been attributed to resonances occurring as a consequence of a significant skin effect in highly conductive samples [118,119]. For the CNT-sponge the real permittivity presents two broad peaks around 10 and 14 GHz while the imaginary permittivity shows a valley at 14.3 GHz. These observations might suggest that the conductivity of the sample is high enough for observing the influence of the skin effect on its dielectric properties.

With regard to the real permittivity, it presents low values along all the swept frequencies, which is noteworthy for a material composed of highly conductive CNT percolating networks. The CNT-sponge is extremely lightweight, which indicates that it has a high volume fraction of air. In accordance, the effective complex permittivity of this material should be governed, at least partially, by the low dielectric constant matrix (air) filling the gaps between CNT networks [105]. However, due to the enhanced electrical conductivity of the sponge, it appears that the effect of the low dielectric constant matrix cannot counteract the effect of the strong ohmic losses, as evidenced by the high reflectivity of the sample ($P_R > P_A$).

II.5 SUMMARY

• Epoxy composites prepared with micrometric ferrite-silica particles, annealed at 700 and 900 $°C$, showed homogeneous distributions and enhanced thermal properties. The high surface area of the ferrite-silica inclusions might be responsible of strengthening the interactions at the filler-matrix interface. The methodology that was employed for the preparation of composites provides an efficient route to disperse nanoparticles in polymers by simple mechanical mixing. However, the EMI SE of these composites did not show any remarkable feature. It was seen that neither absorption nor reflection, had a strong dependence on the magnetic character of the nanoparticles. It is suggested that composites with higher concentrations of ferrite-silica particles than those used in this work (maximal: 25 $wt\%$) are needed for enhancing the magnetic permeability, permittivity and EMI SE of composites. The preparation protocol could be extended to other epoxy formulations having less density and fewer limitations for the incorporation of higher ferrite-silica loads.

• CNFs and Magnetite/CNFs (CNF/Mag) were properly dispersed in an epoxy resin to yield composites with conductivity values of up to 0.3 $S \cdot m^{-1}$. Both type of fillers presented a similar percolation thresholds, indicating that the magnetite nanoparticles adsorbed over the surface of CNFs do not appreciably alter the dispersion process of CNFs. DC conductivity measurements suggest that the gap width for electrical conduction does not vary when nanoparticles are present, although it seems they might reduce the contact area between CNFs.

The increment of permittivity with the $wt\%$ of both type of fillers, and the low magnetic permeability ($\mu' \approx 1$ and $\mu'' \approx 0$) found in all cases, indicate that composites interact mainly with the electric portion of the incident EM energy. It is suggested that the presence of magnetite nanoparticles over the CNFs is responsible of an enhanced interfacial polarization process. As the CNF/Mag load increases, there are more charges prompt to polarization at the numerous magnetite-CNF interfaces. When in contact

with CNFs, magnetite nanoparticles seem to show a synergistic influence on the effective permittivity and SE of composites. CNF/Mag composites showed higher SEs than composites containing only CNFs. Appropriate conductivity, in addition to the dielectric synergism between CNFs and magnetite nanoparticles, provides composites with enhanced absorption SEs.

• Highly percolating nanocomposites have been prepared by infiltration of hierarchically assembled CNT-scaffolds. Upon infiltration, all composites preserved the original skeleton of CNTs and showed remarkable electrical conductivities (from 0.08 to 7.36 $S \cdot m^{-1}$). The conductivity of samples containing magnetite decorated CNxNTs was consistently higher than that of composites prepared with non-decorated CNxNTs having the same $wt\%$, even if these latter had lower net proportions of CNTs. These differences were attributed to the better dispersion of CNxMag nanotubes in the primary aqueous solutions. In addition, the conductivity could be conveniently enhanced without increasing the $wt\%$ of CNTs by converting the polymeric binder of scaffolds into carbon.

The dielectric loss (ϵ'') increased in all composites with the CNT load and ϵ'' was higher for samples containing magnetite decorated CNxNTs. The dielectric constants varied only slightly between composites with large dielectric loss differences. This has been partly attributed to the high porosity of scaffolds, which in composites implies a high volume fraction of a low dielectric constant polymer. Composites presented high SEs ($> 20\ dB$ above $9\ GHz$) and absorption was the main contribution in all cases (> 20 dB above $10\ GHz$). Besides, up to a conductivity of $1.74\ S \cdot m^{-1}$ composites showed a limited reflectivity ($P_A > P_R$), which suggests that EM waves are able to penetrate into the samples for then been strongly dissipated.

• An ultra-light and flexible CNT sponge (density $\leq 0.02\ g \cdot cm^{-3}$) has been found to serve as a high performance EMI shielding material. Due to its extreme lightweight, the specific SE of the CNT-sponge was found to be as high as 1100 $dBcm^3 \cdot g^{-1}$, having a total SE above $20\ dB$ in the whole 1-18 GHz range, and being able to shield

by absorption ($SE_A > SE_R$). To the best of our knowledge this SEE value appears to be the highest reported hitherto. Indeed, the synthesis and properties of CNT-sponges have been described in detail in some early published works[54,55], although they have never been studied as EMI shields. Only denser epoxy composites filled with analogously synthesized CNTs have been evaluated and found efficient as wide-band microwave absorbers[10].

Concerning absorption, efficient EM absorbers should fulfill the antagonistic requirements of being low reflective and highly absorptive, which our CNT-sponges do not fully satisfy. The sponges' net EMI absorption ability is strongly remarkable, but their high electrical conductivity (278 Sm^{-1}) favors incident EM waves to reflect at the input interface. Therefore, CNT sponges would have a great potential for microwave-absorbing applications if combined in a multilayer structure that could prevent reflection.

Bibliography

[1] M. Crespo, M. González, and J. Pozuelo. Magnetic silica:epoxy composites with a nano- and micro-scale control. *Mater. Chem. Phys.*, 144(3),335–342, 2014.

[2] M. Crespo, N. Méndez, M. González, J. Baselga, and J. Pozuelo. Synergistic effect of magnetite nanoparticles and carbon nanofibres in electromagnetic absorbing composites. *Carbon*, 74,63–72, 2014.

[3] M. Crespo, M. González, A. L. Elías, L. Pulickal Rajukumar, J. Baselga, M. Terrones, and J. Pozuelo. Ultra-light carbon nanotube sponge as an efficient electromagnetic shielding material in the ghz range. *Phys. Status Solidi RRL*, 8(8),698–704, 2014.

[4] H. V. Kiran, A. L. Shashimohan, D. K. Chakrabarty, and A. B. Biswas†. Structural and magnetic properties of copper-nickel ferritres. *Phys. Status Solidi A*, 66(2),743–747, 1981.

[5] Y. Jia, W. Han, G. Xiong, and W. Yang. Diatomite as high performance and environmental friendly catalysts for phenol hydroxylation with H¡ sub¿ 2¡/sub¿ O¡ sub¿ 2¡/sub¿. *Sci. Technol. Adv. Mat.*, 8(1–2),106–109, 2007.

[6] M. M. Rashad, R. M. Mohamed, , M. Ibrahim, L. Ismail, and E. Abdel-Aal. Magnetic and catalytic properties of cubic copper ferrite nanopowders synthesized from secondary resources. *Adv. Powder Technol.*, 23(3),315–323, 2012.

[7] J. Msomi and T. Moyo. Effect of domain transformation on the magnetic properties of $Cu_xNi_{1-x}Fe_2O_4$ ferrites. *J. Magn. Magn. Mater.*, 321(19),1246–1250, 2009.

[8] J. Z. Jiang, G. F. Goya, and H. R. Rechenberg. Magnetic properties of nanostructured $CuFe_2O_4$. *J. Phys.: Condens. Matter*, 11(20),4063–4078, 1999.

[9] K. Maaz, S. Karim, A. Mumtaz, S. Hasanain, J. Liu, and J. L. Duan. Synthesis and magnetic characterization of nickel ferrite nanoparticles prepared by co-precipitation route. *J. Magn. Magn. Mater.*, 321(12),1838–1842, 2009.

[10] X. Tan, G. Li, Y. Zhao, and C. Hu. The effect of Cu content on the structure of $Ni_{1-x}Cu_xFe_2O_4$ spinels. *Mater. Res. Bull.*, 44(12),2160–2168, 2009.

[11] F. S. Tehrani, V. Daadmehr, A. T. Rezakhani, R. H. Akbarnejad, and S. Gholipour. Structural, magnetic, and optical properties of zinc-and copper-substituted nickel ferrite nanocrystals. *J. superconductivity novel magnetism*, 25(7),2443–2455, 2012.

[12] S. G. Doh, E. B. Kim, B. H. Lee, and J. H. Oh. Characteristics and synthesis of Cu-Ni ferrite nanopowders by coprecipitation method with ultrasound irradiation. *J. Magn. Magn. Mater.*, 272–276,2238–2240, 2004.

[13] B. Folch, J. Larionova, Y. Guari, L. Datas, and C. Guerin. A coordination polymer precursor approach to the synthesis of $NiFe$ bimetallic nanoparticles within hybrid mesoporous silica. *J. Mater. Chem.*, 16(45),4435–4442, 2006.

[14] V. M. Gun'ko, R. Leboda, J. Skubiszewska-Zięba, V. V. Turov, and P. Kowalczyk. Structure of Silica Gel Si-60 and Pyrocarbon/Silica Gel Adsorbents Thermally and Hydrothermally Treated. *Langmuir*, 17(11),3148–3161, 2001.

[15] Z. J. Li, C. R. Liu, and Q. S. Zhao. Effect of heat treatment on the pore structure properties of silica gel powders derived from water glass. *J. Non-Cryst. Solids*, 265(1-2),189–192, 2000.

[16] C. J. Brinker, K. D. Keefer, D. W. Schaefer, and C. S. Ashley. Sol-gel transition in simple silicates. *J. Non-Cryst. Solids*, 48(1),47–64, 1982.

[17] R. Köhn and M. Fröba. Nanoparticles of 3d transition metal oxides in mesoporous MCM-48 silica host structures: Synthesis and characterization. *Catal. Today*, 68(1–3),227–236, 2001.

[18] A. B. Fuertes and D. M. Nevskaia. Control of mesoporous structure of carbons synthesised using a mesostructured silica as template. *Microporous Mesoporous Mater.*, 62(3),177–190, 2003.

[19] R. Hergt, S. Dutz, and M. Röder. Effects of size distribution on hysteresis losses of magnetic nanoparticles for hyperthermia. *J. Phys. Condens. Matter*, 20(38),385214, 2008.

[20] Y. W. Duan, X. L. Kou, and J. G. Li. Size dependence of structure and magnetic properties of $La_{0.7}Sr_{0.3}MnO_3$ nanoparticles. *Phys. B*, 355(1–4),250–254, 2005.

[21] E. J. Choi, Y. Ahn, and Y. D. Her. Size Dependence of Magnetic Properties of Co-Ferrite Nanoparticles. *J. Korean Phys. Soc.*, 50(2),460–463, 2007.

[22] Y. Zhu, J. C. Zhang, J. Zhai, and Y. M. Zheng. Multifunctional carbon nanofibers with conductive, magnetic and superhydrophobic properties. *ChemPhysChem*, 7(2),336–341, 2006.

[23] M. González, I. Martín-Fabiani, J. Baselga, and J. Pozuelo. Magnetic nanocomposites based on hydrogenated epoxy resin. *Mater. Chem. Phys.*, 132(2-3),618–624, 2012.

[24] X. Lepró, Y. Vega-Cantú, F. J. Rodríguez-Macías, Y. Bando, D. Golberg, and M. Terrones. Production and characterization of coaxial nanotube junctions and networks of CNx/CNT. *Nano Lett.*, 7(8),2220–2226, 2007.

[25] A. Zamudio, A. Elías, J. Rodríguez-Manzo, F. López-Urías, G. Rodríguez-Gattorno, F. Lupo, M. Rühle, D. Smith, H. Terrones, D. Díaz, and M. Terrones. Efficient anchoring of silver nanoparticles on n-doped carbon nanotubes. *Small*, 2(3),346–350, 2006.

[26] K. Jiang, A. Eitan, L. L. S. Schadler, P. M. Ajayan, R. W. Siegel, N. Grobert, M. Mayne, M. Reyes-Reyes, H. Terrones, and M. Terrones. Selective attachment

of gold nanoparticles to nitrogen-doped carbon nanotubes. *Nano Lett.*, 3(3),275–277, 2003.

[27] M. S. Dresselhaus, A. Jorio, M. Hofmann, G. Dresselhaus, and R. Saito. Perspectives on carbon nanotubes and graphene raman spectroscopy. *Nano Lett.*, 10(3),751–758, 2010.

[28] S. Nardecchia, D. Carriazo, M. L. Ferrer, M. C. Gutiérrez, and F. del Monte. Three dimensional macroporous architectures and aerogels built of carbon nanotubes and/or graphene: synthesis and applications. *Chem. Soc. Rev.*, 42(2),794–830, 2013.

[29] L. Liu, W. Ma, and Z. Zhang. Macroscopic carbon nanotube assemblies: preparation, properties, and potential applications. *Small*, 7(11),1504–1520, 2011.

[30] X. Gui, J. Wei, K. Wang, A. Cao, H. Zhu, Y. Jia, Q. Shu, and D. Wu. Carbon nanotube sponges. *Adv. Mater.*, 22(5),617–621, 2010.

[31] X. Gui, Z. Lin, Z. Zeng, K. Wang, D. Wu, and Z. Tang. Controllable synthesis of spongy carbon nanotube blocks with tunable macro- and microstructures. *Nanotechnol.*, 24(8),085705, 2013.

[32] Y. Naito and K. Suetake. Application of Ferrite to Electromagnetic Wave Absorber and its Characteristics. *IEEE Trans. Microw. Theory Techn.*, 19(1),65–72, 1971.

[33] D. R. Patil and B. K. Chougule. Effect of copper substitution on electrical and magnetic properties of $NiFe_2O_4$ ferrite. *Mater. Chem. Phys.*, 117(1),35–40, 2009.

[34] G. F. Goya and H. R. Rechenberg. Superparamagnetic transition and local disorder in $CuFe_2O_4$ nanoparticles. *Nanostruct. Mater.*, 10(6),1001–1011, 1998.

[35] J. Zhu, S. Wei, I. Y. Lee, S. Park, J. Willis, N. Haldolaarachchige, D. P. Young, Z. Luo, and Z. Guo. Silica stabilized iron particles toward anti-corrosion magnetic polyurethane nanocomposites. *RSC Adv.*, 2(3),1136–1143, 2012.

[36] M. Chen, H. Qu, J. Zhu, Z. Luo, A. Khasanov, A. S. Kucknoor, N. Haldolaarachchige, D. P. Young, S. Wei, and Z. Guo. Magnetic electrospun fluorescent polyvinylpyrrolidone nanocomposite fibers. *Polym.*, 53(20),4501–4511, 2012.

[37] X. Ji, J. E. Hampsey, Q. Hu, J. He, Z. Yang, and Y. Lu. Mesoporous Silica-Reinforced Polymer Nanocomposites. *Chem. Mater.*, 15(19),3656–3662, 2003.

[38] K. Moller, T. Bein, and R. X. Fischer. Entrapment of PMMA Polymer Strands in Micro- and Mesoporous Materials. *Chem. Mater.*, 10(7),1841–1852, 1998.

[39] S. Nikkeshi, M. Kudo, and T. Masuko. Dynamic viscoelastic properties and thermal properties of Ni powder-epoxy resin composites. *J. Appl. Polym. Sci.*, 69(13),2593–2598, 1998.

[40] S. Kwon, T. Adachi, W. Araki, and A. Yamaji. Thermo-viscoelastic properties of silica particulate-reinforced epoxy composites: Considered in terms of the particle packing model. *Acta Mater.*, 54(12),3369–3374, 2006.

[41] Y. Tanaka, Y. Nakahara, and K. Takemoto. Effect of surface structure of porous silica microballoons on dynamic mechanical properties of amine cured epoxy resin composites. *Angew. Makromol. Chem.*, 191(1),71–80, 1991.

[42] O. Becker, R. J. Varley, and G. P. Simon. Thermal stability and water uptake of high performance epoxy layered silicate nanocomposites. *Eur. Polym. J.*, 40(1),187–195, 2004.

[43] J. C. Paterson-Jones. The mechanism of the thermal degradation of aromatic amine-cured glycidyl ether-type epoxide resins. *J. Appl. Polym. Sci.*, 19(6),1539–1547, 1975.

[44] N. Grassie, M. I. Guy, and N. H. Tennent. Degradation of epoxy polymers: Part 4—Thermal degradation of bisphenol-A diglycidyl ether cured with ethylene diamine. *Polym. Degrad. Stab.*, 14(2),125–137, 1986.

[45] Y.-L. Liu, W.-L. Wei, K.-Y. Hsu, and W.-H. Ho. Thermal stability of epoxy-silica hybrid materials by thermogravimetric analysis. *Thermochim. Acta*, 412(1–2),139–147, 2004.

[46] C. D. Doyle. Estimating thermal stability of experimental polymers by empirical thermogravimetric analysis. *Anal. Chem.*, 33(1),77–79, 1961.

[47] J. Wen and G. L. Wilkes. Organic/Inorganic Hybrid Network Materials by the Sol-Gel Approach. *Chem. Mater.*, 8(8),1667–1681, 1996.

[48] J. Macan, I. Brnardić, S. Orlić, H. Ivanković, and M. Ivanković. Thermal degradation of epoxy-silica organic-inorganic hybrid materials. *Polym. Degrad. Stab.*, 91(1),122–127, 2006.

[49] S.-J. Park and M.-S. Cho. Thermal stability of carbon-$MoSi_2$-carbon composites by thermogravimetric analysis. *J. Mater. Sci.*, 35(14),3525–3527, 2000.

[50] A. N. Yusoff, M. H. Abdullah, S. H. Ahmad, S. F. Jusoh, A. A. Mansor, S. A. A. Hamid, and I. Introduction. Electromagnetic and absorption properties of some microwave absorbers. *J. Appl. Phys.*, 92(2),876, 2002.

[51] L. Deng and M. Han. Microwave absorbing performances of multiwalled carbon nanotube composites with negative permeability. *Appl. Phys. Lett.*, 91(2),023119, 2007.

[52] Based on: DrBob, Optical-coating-2, commons.wikimedia.org, 2004.

[53] Y. J. Chen, M. S. Cao, T. H. Wang, and Q. Wan. Microwave absorption properties of the ZnO nanowire-polyester composites. *Appl. Phys. Lett.*, 84(17),3367–3369, 2004.

[54] I. Kong, S. Hj, M. Hj, D. Hui, A. Nazlim, D. Puryanti, S. Hj Ahmad, M. Hj Abdullah, and A. Nazlim Yusoff. Magnetic and microwave absorbing properties of magnetite-thermoplastic natural rubber nanocomposites. *J. Magn. Magn. Mater.*, 322(21),3401–3409, 2010.

[55] E. P. Wolffarth, editor. *Ferromagnetic Materials: A Handbook on the Properties of Magnetically Ordered Substances, Volume 2.* North-Holland Publishing Company, 1980.

[56] N. Rezlescu and E. Rezlescu. Dielectric properties of copper containing ferrites. *Phys. Status Solidi A*, 23(2),575–582, 1974.

[57] P. C. P. Watts, W. K. Hsu, A. Barnes, and B. Chambers. High Permittivity from Defective Multiwalled Carbon Nanotubes in the X-Band. *Adv. Mater.*, 15(78),600–603, 2003.

[58] S. M. Abbas, A. K. Dixit, R. Chatterjee, and T. C. Goel. Complex permittivity, complex permeability and microwave absorption properties of ferrite-polymer composites. *J. Magn. Magn. Mater.*, 309(1),20–24, 2007.

[59] H. Bayrakdar. Complex permittivity, complex permeability and microwave absorption properties of ferrite-paraffin polymer composites. *J. Magn. Magn. Mater.*, 323(14),1882–1885, 2011.

[60] R. Valenzuela. Novel applications of ferrites. *Phys. Res. Int.*, 2012, 2012.

[61] Z. Shi, J. Zhang, D. Gao, Z. Zhu, Z. Yang, Z. Zhang, and D. Xue. Magnetic resonance of the $NiFe_2O_4$ nanoparticles in the gigahertz range. *Nanoscale Res. Lett.*, 8(1),404, 2013.

[62] M. Antunes, M. Mudarra, and J. Velasco. Broad-band electrical conductivity of carbon nanofibre-reinforced polypropylene foams. *Carbon*, 49(18),708–717, 2011.

[63] L. Guadagno, B. De Vivo, A. Di Bartolomeo, P. Lamberti, A. Sorrentino, V. Tucci, L. Vertuccio, and V. Vittoria. Effect of functionalization on the

thermo-mechanical and electrical behavior of multi-wall carbon nanotube/epoxy composites. *Carbon*, 49(6),1919–1930, 2011.

[64] Y. Qing, W. Zhou, F. Luo, and D. Zhu. Epoxy-silicone filled with multi-walled carbon nanotubes and carbonyl iron particles as a microwave absorber. *Carbon*, 48(14),4074–4080, 2010.

[65] Y. J. Kim, T. S. Shin, H. D. Choi, J. H. Kwon, Y. C. Chung, and H. G. Yoon. Electrical conductivity of chemically modified multiwalled carbon nanotube/epoxy composites. *Carbon*, 43(1),23–30, 2005.

[66] Q. P. Feng, J. P. Yang, S. Y. Fu, and Y. W. Mai. Synthesis of carbon nanotube/epoxy composite films with a high nanotube loading by a mixed-curing-agent assisted layer-by-layer method and their electrical conductivity. *Carbon*, 48(7),2057–2062, 2010.

[67] N. Li, Y. Huang, F. Du, X. He, X. Lin, H. Gao, Y. Ma, F. Li, Y. Chen, and P. C. Eklund. Electromagnetic interference (EMI) shielding of single-walled carbon nanotube epoxy composites. *Nano Lett.*, 6(6),1141–1145, 2006.

[68] M. H. Al-Saleh and U. Sundararaj. A review of vapor grown carbon nanofiber/polymer conductive composites. *Carbon*, 47(1),2–22, 2009.

[69] S. Yang, K. Lozano, A. Lomeli, H. D. Foltz, and R. Jones. Electromagnetic interference shielding effectiveness of carbon nanofiber/LCP composites. *Compos. Part A*, 36(5),691–697, 2005.

[70] A. P. Ramirez, R. C. Haddon, O. Zhou, R. M. Fleming, J. Zhang, S. M. McClure, and R. E. Smalley. Magnetic Susceptibility of Molecular Carbon: Nanotubes and Fullerite. *Sci.*, 265(5168),84–86, 1994.

[71] K.-Y. Park, J.-H. Han, S.-B. Lee, J.-B. Kim, J.-W. Yi, and S.-K. Lee. Fabrication and electromagnetic characteristics of microwave absorbers containing carbon nanofibers and NiFe particles. *Compos. Sci. Technol.*, 69(7-8),1271–1278, 2009.

[72] A. P. Singh, P. Garg, F. Alam, K. Singh, R. Mathur, R. Tandon, A. Chandra, and S. Dhawan. Phenolic resin-based composite sheets filled with mixtures of reduced graphene oxide, γ-Fe2O3 and carbon fibers for excellent electromagnetic interference shielding in the X-band. *Carbon*, 50(10),3868–3875, 2012.

[73] A. Allaoui and N. E. Bounia. How carbon nanotubes affect the cure kinetics and glass transition temperature of their epoxy composites? - A review. *Express Polym. Lett.*, 3(9),588–594, 2009.

[74] K. S. Khare and R. Khare. Effect of Carbon Nanotube Dispersion on Glass Transition in Cross-Linked Epoxy-Carbon Nanotube Nanocomposites: Role of Interfacial Interactions. *J. Phys. Chem. B*, 117(24),7444–7454, 2013.

[75] B. H. Cipriano, A. K. Kota, A. L. Gershon, C. J. Laskowski, T. Kashiwagi, H. A. Bruck, and S. R. Raghavan. Conductivity enhancement of carbon nanotube and nanofiber-based polymer nanocomposites by melt annealing. *Polym.*, 49,4846–4851, 2008.

[76] S. Bal. Experimental study of mechanical and electrical properties of carbon nanofiber/epoxy composites. *Mater. Des.*, 31(5),2406–2413, 2010.

[77] D. Stauffer and A. Aharony. *Introduction to percolation theory.* Taylor and Francis, 1991.

[78] M. T. Connor, S. Roy, T. A. Ezquerra, and F. J. B. Calleja. Broadband ac conductivity of conductor-polymer composites. *Phys. Rev. B: Condens. Matter Mater. Phys.*, 57(4),2286–2294, 1998.

[79] P. Sheng. Fluctuation-induced tunneling conduction in disordered materials. *Phys. Rev. B: Condens. Matter Mater. Phys.*, 21(6),2180–2195, 1980.

[80] P. Sheng, E. K. Sichel, and J. I. Gittleman. Fluctuation-induced tunneling conduction in carbon-polyvinylchloride composites. *Phys. Rev. Lett.*, 40,1197–1200, 1978.

[81] A. V. Kyrylyuk and P. van der Schoot. Continuum percolation of carbon nanotubes in polymeric and colloidal media. *Proc. Natl. Acad. Sci.*, 105(24),8221–8226, 2008.

[82] R. A. Ali-Zade. Permittivity of nanocomposites based on magnetite nanoparticles and polymer matrices (collagen and polystyrene). *Russ. J. Phys. Chem. A*, 84(9),1570–1575, 2010.

[83] I. Balberg. Recent developments in continuum percolation. *Philos. Mag. B*, 56(6),991–1003, 1987.

[84] I. Balberg, C. H. Anderson, S. Alexander, and N. Wagner. Excluded volume and its relation to the onset of percolation. *Phys. Rev. B: Condens. Matter Mater. Phys.*, 30(7),3933–3943, 1984.

[85] M. A. Miller. On structural correlations in the percolation of hard-core particles. *J. Chem. Phys.*, 131(6),066101, 2009.

[86] A. Prasad and K. Prasad. Effective permittivity of random composite media: A comparative study. *Phys. B*, 396(1–2),132–137, 2007.

[87] P. C. Fannin, C. N. Marin, I. Malaescu, and N. Stefu. Microwave dielectric properties of magnetite colloidal particles in magnetic fluids. *J. Phys.: Condens. Matter*, 19(3),036104, 2007.

[88] V. A. Labunov, A. L. Danilyuk, A. L. Prudnikava, I. Komissarov, B. G. Shulitski, C. Speisser, F. Antoni, F. Le Normand, and S. L. Prischepa. Microwave absorption in nanocomposite material of magnetically functionalized carbon nanotubes. *J. Appl. Phys.*, 112(2),024302, 2012.

[89] A. Pakhomov, S. Wong, X. Yan, and X. Zhang. Low-frequency divergence of the dielectric constant in metal-insulator nanocomposites with tunneling. *Phys. Rev. B: Condens. Matter Mater. Phys.*, 58(20),R13375–R13378, 1998.

[90] R. Waser, U. Böttger, and S. Tiedke, editors. *Polar Oxides: Properties, Characterization, and Imaging*, chapter Sol-Gel Processing and Applications. Wiley, 2006.

[91] Z.-M. Dang, J.-K. Yuan, S.-H. Yao, and R.-J. Liao. Flexible nanodielectric materials with high permittivity for power energy storage. *Adv. Mater.*, 25(44),6334–6365, 2013.

[92] M. Terrones, O. Martín, M. González, J. Pozuelo, B. Serrano, J. C. Cabanelas, S. M. Vega-D/'iaz, and J. Baselga. Interphases in graphene polymer-based nanocomposites: Achievements and challenges. *Adv. Mater.*, 23(44),5302–5310, 2011.

[93] R. B. Laibowitz and Y. Gefen. Dynamic scaling near the percolation threshold in thin Au films. *Phys. Rev. Lett.*, 53(4),380–383, 1984.

[94] Y. Gefen, A. Aharony, and S. Alexander. Anomalous diffusion on percolating clusters. *Phys. Rev. Lett.*, 50(77),77–80, 1983.

[95] J. Sandler, M. S. P. Shaffer, T. Prasse, W. Bauhofer, K. Schulte, and A. H. Windle. Development of a dispersion process for carbon nanotubes in an epoxy matrix and the resulting electrical properties. *Polym.*, 40(21),5967–5971, 1999.

[96] Z. Wang and X. Ye. A numerical investigation on piezoresistive behaviour of carbon nanotube/polymer composites: mechanism and optimizing principle. *Nanotechnol.*, 24(26),265704, 2013.

[97] J. K. W. Sandler, J. E. Kirk, I. A. Kinloch, M. S. P. Shaffer, and A. H. Windle. Ultra-low electrical percolation threshold in carbon-nanotube-epoxy composites. *Polym.*, 44(19),5893–5899, 2003.

[98] M.-J. Jiang, Z.-M. Dang, M. Bozlar, F. Miomandre, and J. Bai. Broad-frequency dielectric behaviors in multiwalled carbon nanotube/rubber nanocomposites. *J. Appl. Phys.*, 106(8),084902, 2009.

[99] B. E. Kilbride, J. N. Coleman, J. Fraysse, P. Fournet, M. Cadek, a. Drury, S. Hutzler, S. Roth, and W. J. Blau. Experimental observation of scaling laws for alternating current and direct current conductivity in polymer-carbon nanotube composite thin films. *J. Appl. Phys.*, 92(7),4024, 2002.

[100] S. Barrau, P. Demont, A. Peigney, C. Laurent, and C. Lacabanne. Dc and ac conductivity of carbon nanotubes–polyepoxy composites. *Macromol.*, 36(14),5187–5194, 2003.

[101] I. Huynen, N. Quiévy, C. Bailly, P. Bollen, C. Detrembleur, S. Eggermont, I. Molenberg, J. M. Thomassin, L. Urbanczyk, and T. Pardoen. Multifunctional hybrids for electromagnetic absorption. *Acta Mater.*, 59(8),3255–3266, 2011.

[102] N. Quievy and P. Bollen. Electromagnetic absorption properties of carbon nanotube nanocomposite foam filling honeycomb waveguide structures. *IEEE Electrmagn. Compat.*, 54(1),43–51, 2012.

[103] D. Hecht, L. Hu, and G. Grüner. Conductivity scaling with bundle length and diameter in single walled carbon nanotube networks. *Appl. Phys. Lett.*, 89(13),133112, 2006.

[104] Y. A. Attia, editor. *Sol-Gel Processing and Applications*. Springer US, 1994.

[105] X. Xiao, R. Streiter, G. Ruan, R. Song, T. Otto, and T. Gessner. Modelling and simulation for dielectric constant of aerogel. *Microelectron. Eng.*, 54(3-4),295–301, 2000.

[106] Z. Fang, X. Cao, C. Li, H. Zhang, J. Zhang, and H. Zhang. Investigation of carbon foams as microwave absorber: Numerical prediction and experimental validation. *Carbon*, 44(15),3368–3370, 2006.

[107] Q. Liu, D. Zhang, and T. Fan. Electromagnetic wave absorption properties of porous carbon/Co nanocomposites. *Appl. Phys. Lett.*, 93(1),013110, 2008.

[108] J.-M. Thomassin, C. Pagnoulle, L. Bednarz, I. Huynen, R. Jerome, and C. Detrembleur. Foams of polycaprolactone/MWNT nanocomposites for efficient EMI reduction. *J. Mater. Chem.*, 18(7),792–796, 2008.

[109] Y. Yang, M. C. Gupta, K. L. Dudley, and R. W. Lawrence. Novel carbon nanotube-polystyrene foam composites for electromagnetic interference shielding. *Nano Lett.*, 5(11),2131–2134, 2005.

[110] Z. Chen, C. Xu, C. Ma, W. Ren, and H.-M. Cheng. Lightweight and flexible graphene foam composites for high-performance electromagnetic interference shielding. *Adv. Mater.*, 25(9),1296–300, 2013.

[111] R. Kumar, S. R. Dhakate, T. Gupta, P. Saini, B. P. Singh, and R. B. Mathur. Effective improvement of the properties of light weight carbon foam by decoration with multi-wall carbon nanotubes. *J. Mater. Chem. A*, 1(1),5727–5735, 2013.

[112] J. Ling, W. Zhai, W. Feng, B. Shen, J. Zhang, and W. G. Zheng. Facile preparation of lightweight microcellular polyetherimide/graphene composite foams for electromagnetic interference shielding. *ACS Appl. Mater. Interfaces*, 5(7),2677–2684, 2013.

[113] D.-X. Yan, P.-G. Ren, H. Pang, Q. Fu, M.-B. Yang, and Z.-M. Li. Efficient electromagnetic interference shielding of lightweight graphene / polystyrene composite. *J. Mater. Chem.*, 22,18772–18774, 2012.

[114] F. Moglie, D. Micheli, S. Laurenzi, M. Marchetti, and V. Mariani Primiani. Electromagnetic shielding performance of carbon foams. *Carbon*, 50(5),1972–1980, 2012.

[115] M. H. Al-Saleh and U. Sundararaj. Electromagnetic interference shielding mechanisms of CNT/polymer composites. *Carbon*, 47(7),1738–1746, 2009.

[116] I. M. De Rosa, F. Sarasini, M. S. Sarto, and A. Tamburrano. EMC Impact of Advanced Carbon Fiber/Carbon Nanotube Reinforced Composites for Next-Generation Aerospace Applications. *IEEE Electrmagn. Compat.*, 50(3),556–563, 2008.

[117] Z. Fang, C. Li, J. Sun, H. Zhang, and J. Zhang. The electromagnetic characteristics of carbon foams. *Carbon*, 45(15),2873–2879, 2007.

[118] J. Liu, R. Che, H. Chen, F. Zhang, F. Xia, Q. Wu, and M. Wang. Microwave absorption enhancement of multifunctional composite microspheres with spinel Fe_3O_4 Cores and Anatase TiO_2 shells. *Small*, 8(8),1214–1221, 2012.

[119] R. C. Che, L. M. Peng, X. F. Duan, Q. Chen, and X. L. Liang. Microwave Absorption Enhancement and Complex Permittivity and Permeability of Fe Encapsulated within Carbon Nanotubes. *Adv. Mater.*, 16(5),401–405, 2004.

CHAPTER 4

CONCLUSIONS & FUTURE PERSPECTIVES

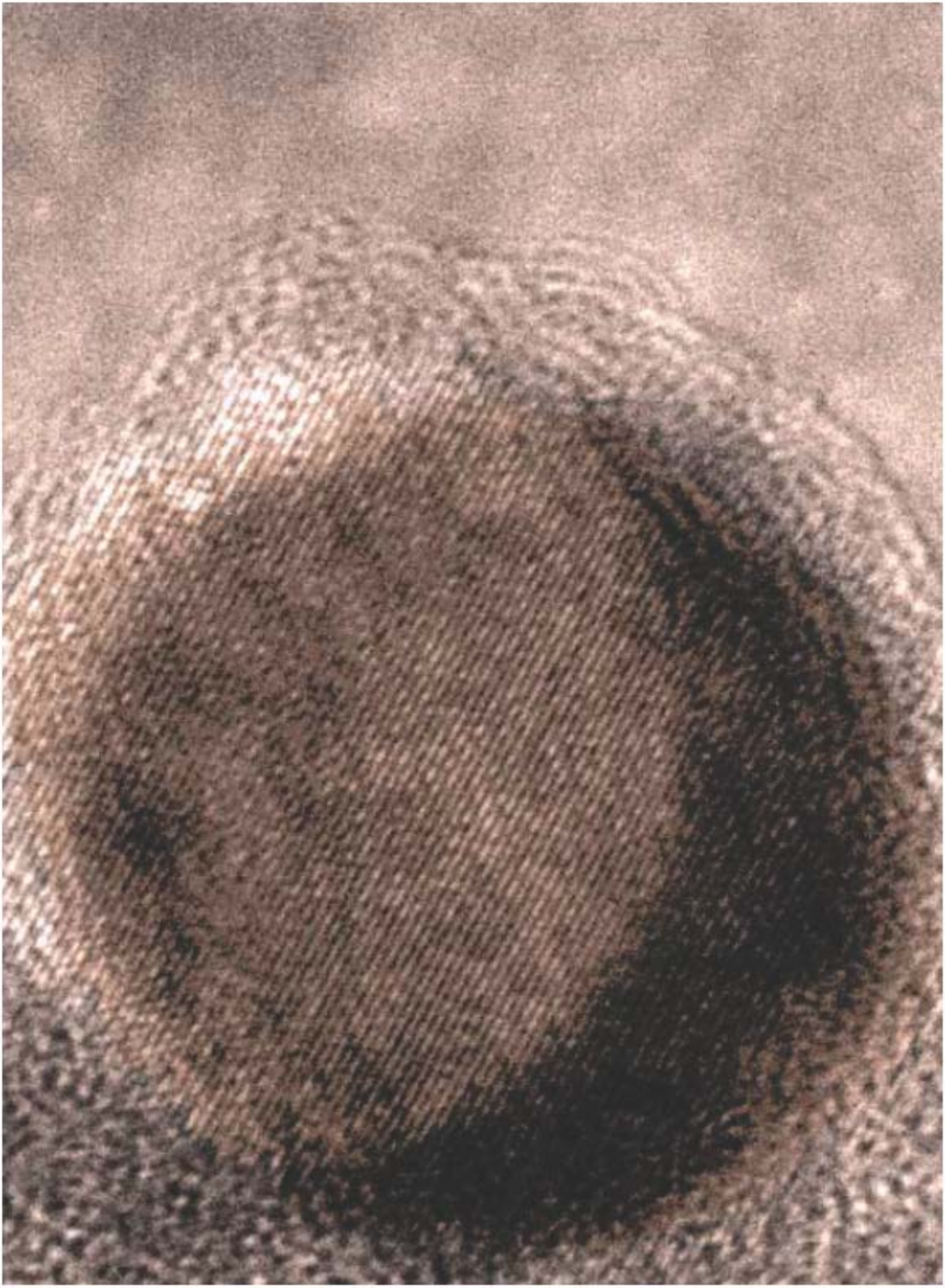

Conclusions & future perspectives

Composites with conductive and magnetic nanoparticles have been prepared through a variety of strategies and have been tested as EMI shields. The proper assortment of electrical conductivity, permittivity and magnetic permeability allows preparing composites with tailored EM characteristics.

Nanoferrites can be synthesized within mesoporous silica microparticles (template) and their morphology can be controlled by means of the template constraint and the annealing temperature. Epoxy composites prepared through the incorporation of the silica-ferrite hybrids showed homogeneous reinforcement dispersions, implying a good dispersion of the nanoparticles as well. However, self-supported EMI shielding materials could not be obtained through composites containing solely magnetic nanoparticles. The SE of these composites did not show any remarkable feature. It was seen that neither absorption nor reflection had a strong dependence on the magnetic character of the nanoparticles. It is thus concluded that composites with higher concentrations of magnetic nanoinclusions than those herein reported might be needed in order to have materials with enhanced magnetic permeability, permittivity and EMI SE.

Conductive hybrids of CNFs and magnetite nanoparticles can be prepared by simply placing both components in a non-polar solvent. Composites prepared with either CNFs or CNF/Mag showed homogeneous reinforcement dispersions, although the maximum conductivity that could be reached was $\sim 0.3\ S \cdot m^{-1}$ ($10\ wt\%$). When combined with magnetic nanoparticles, composites presented higher absorption coefficients ($13\ dB \cdot cm^{-1}$) than those of composites containing only CNFs ($10\ dB \cdot cm^{-1}$). This effect was attributed to interfacial polarization, since when nanoparticles are introduced within the conductive fibers there is a greater number of boundaries and interfaces prone to polarization. In consequence it is concluded that this mechanisms contributes to dissipate or absorb EM waves within conductive composites.

Anisotropic scaffolds of CNxCNTs and magnetite-decorated CNxCNTs can be prepared by freeze-drying (uniaxially) aqueous dispersions of these CNTs and a polymeric binder. Scaffolds presented densities lower than 0.07 $g \cdot cm^{-3}$, which indicates that the original amount of nanotubes (< 6 $wt\%$) forms a percolating network through a large macroscopic volume. In contrast to CNF-epoxy composites prepared by regular blending, infiltration of CNT-scaffolds yielded composites with superior conductivities (from 0.08 to 7.36 $S \cdot m^{-1}$). This can be attributed to the better interconnectivity between CNTs, since they have been brought closer during the formation of scaffolds; although CNTs are embedded within the polymeric binder, they are forced to form contacts. Favoring CNT interconnectivity enhances the SE (> 20 dB above 9 GHz), which in combination with limited CNT loads and a proper conductivity (~ 1 $S \cdot m^{-1}$) seems to enhance the absorption of composites (≥ 20 dB above 10 GHz), without increasing their front-face reflectivity ($P_A > P_R$). As reflection occurs due to the impedance mismatch, and increases with the effective permittivity, limited reflectivities were attributed to: a) the enhanced interconnectivity between adjacent CNTs in scaffolds, which favors the dissipation of energy through ohmic losses rather than by dielectric means; b) the high volume fraction of polymer (low ϵ') and the low CNT loads that scaffold composites present.

Flexible and mechanically robust CNT-sponges can be synthesized through CVD. Through the optimal conditions, isotropic sponges of at least 2.8 mm in thickness could be obtained. Despite their lightweight (0.02 $g \cdot cm^{-3}$) CNT-sponges showed higher conductivities than the rest of materials (ca. to 278 $S \cdot m^{-1}$), due to their superior CNT interconnectivity. As it was seen in the case of CNT-scaffolds, through the appropriate microstructure it seems feasible to tune the reflectivity of conductive nanocomposites. However, front-face reflectivity could be restricted only up to a certain conductivity or permittivity value. Although CNT-sponges have a specific SE as high as 1100 $dBcm^3g^{-1}$, and a constant SE above 20 dB between 1 and 18 GHz, their high electrical conductivity favors the wave to reflect at the input interface ($P_A < P_R$).

Results verify the wide variety of options that polymer composites with magnetic nanoparticles and nanocarbons can offer depending upon the final shielding application in which they might be needed.

Appendix A

In most magnetic nanocomposites permeability is small, since the effective permeability of composites is strongly dependent on the volume fraction [1]. Therefore, the limited concentrations that are feasible for nanoinclusions have been pointed out to be responsible of the low magnitude of permeability [2]. Due to this limitation, most reported results are focused on using magnetic nanocomposites as quarter wave-thick microwave absorbers (Dallenbach layers) [3]. The aim in such case is to achieve zero reflections with a coating of minimum thickness when applied over a metal substrate.

Composites prepared in this work were intended to serve as self-supported EMI suppressors and not as quarter wave-thick shields therefore, shielding has been evaluated by means of the SE. However, since the shielding performance of composites having only magnetic nanoparticles is normally reported in terms of the reflection loss (RL), it has been considered important to explain the fundamental theory of such evaluation method.

Total impedance matching, or zero-reflection, is achieved when the input impedance (Z_{in}) equals the impedance of free space (Z_0), as given by [4]:

$$Z_{in} = \sqrt{\frac{\mu_r}{\epsilon_r}} \tanh \left[j \frac{2\pi}{c} \sqrt{\mu_r \epsilon_r} f d \right] = z_0 \tag{A.1}$$

where d, μ_r and ϵ_r are the thickness, the relatively permeability and the relatively permittivity of the coating layer respectively; $c = 3 \cdot 10^{-8}\ m \cdot s^{-1}$ and f is the frequency of the electromagnetic wave. The reflection loss (RL) of the incident electromagnetic wave normal to the metal-backed absorber can be expressed as:

$$RL\,(dB) = 20 \log \left| \frac{Z_{in} - 1}{Z_{in} + 1} \right| \tag{A.2}$$

For microwave absorption, the RL should be as negative as possible. Nevertheless, a RL of less than -20 dB is normally considered as an acceptable shielding threshold, at which Z_{in} and Z_0 can be said to be matched [5]. In order to satisfy this condition with a coating layer of minimum thickness, both μ_r and ϵ_r can be manipulated.

In magnetic composites, there exists a complex interplay between both magnitudes [6]. In a variety of systems that rendered poor absorption with only magnetic nanoparticles, the increase of permittivity with core/shell structures improved their absorption due to additional interfacial polarization contributions. Some examples include Fe nanoflakes coated with SiO_2 [7], Al_2O_3-coated $FeNi_3$ nanoparticles [8], ZnO-coated Fe nanocapsules [9], or Co/graphite nanoparticles [10]. Particularly interesting are some works in which this effect is evidenced with varying the thickness of the shell, its chemical nature or by adding new shells to the structure. For example the case of microspheres with Fe_3O_4@SiO_2 yolks and SnO_2 shells (Figure A.1) [11]. The permittivity increased when Fe_3O_4@SiO_2 microspheres were coated with an additional SiO_2 shell, and then entrapped with a SnO_2 layer, forming the yolk-shell structure. The RL of composites prepared with these particles increased in the same manner as permittivity, reaching values of up to -30 dB for slab thicknesses of only 2 mm, as shown in Figure A.1.

Spinel Fe_3O_4 cores with Anatase-TiO_2 shells were also studied in another work, regarding the size of both the magnetic cores and the dielectric shells [11]. It was found that the maximum RL (-23.3 dB) was obtained at 7 GHz with the particles with

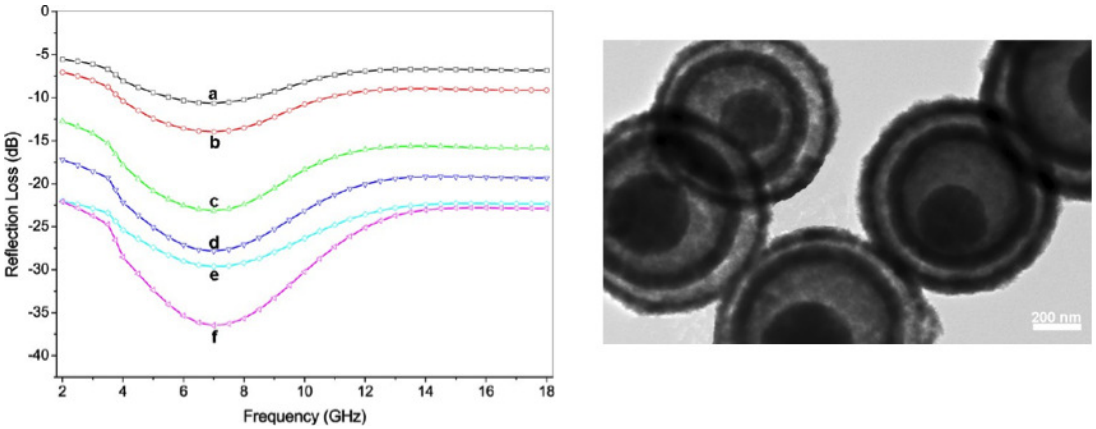

FIGURE A.1: Frequency dependence of real and imaginary parts of complex permittivity and permeability of the EP composites containing Fe_3O_4 particles (a), Fe_3O_4@SiO_2 microspheres (b), single-shelled Fe_3O_4@SiO_2 yolk-shell microspheres (c), and double-shelled Fe_3O_4@SiO_2 yolk-shell microspheres (d-f) with varying inter-shell distances. The representative SEM image on the right shows the microstructure of the yolk-shell nanoparticles [11]

the biggest cores (150 nm) and the thickener shells (150 nm), which showed also the highest permeability and permittivity values.

Recently a wide variety of core/shell nanoparticles (Fe/SiO_2, Ni/SiO_2, Fe/B_2O_3, Ni/B_2O_3, Fe/Al_2O_3, Fe/MnO_2, Fe/Y_2O_3, Fe/CeO_2, and Fe/La_2O_3) were successfully synthesized by a one-pot arc discharge method [12]. Owing to the variability of the particles' permeability and permittivity, composites prepared through their incorporation could provide high RL with limited slab thicknesses (1.46-5 mm) in practically all the S-Ku microwave bands (Figure A.2).

In all these examples, the ability of absorption depends on the best matching thickness (t_m) or, in analogy, to the matching frequency (f_m), which for magnetic and codielectric materials are respectively related to the magnetic loss (μ'') and to the dielectric loss (ϵ'') by [12,13]:

$$\mu'' = \frac{c}{2\pi f_m d} \tag{A.3}$$

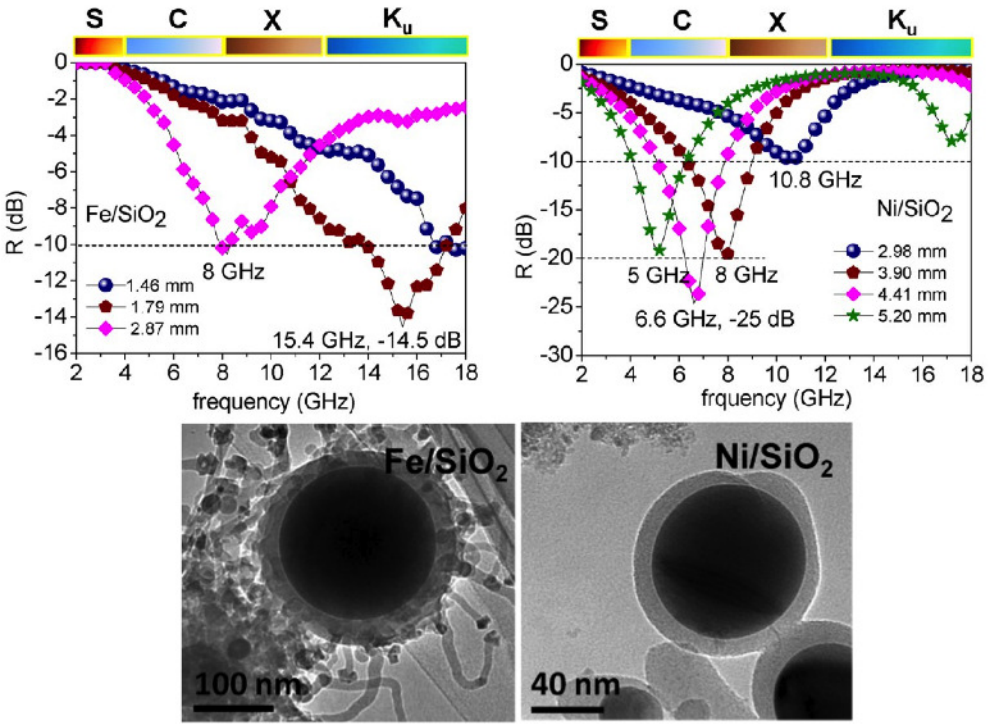

FIGURE A.2: Microwave RL of Fe/SiO_2 and Ni/SiO_2 and their corresponding SEM images showing the core-shell structure [12]

$$\epsilon'' = \frac{c}{2\pi f_m d} \tag{A.4}$$

where c is the speed of light in vacuum and d is the thickness of the shield. Therefore μ'' and ϵ'', together with the thickness of the slab, can be adjusted to satisfy the best matching conditions and hence minimize reflection.

Bibliography

[1] V. Sunny, P. Kurian, P. Mohanan, P. Joy, and M. Anantharaman. A flexible microwave absorber based on nickel ferrite nanocomposite. *J. Alloy. Compd.*, 489(1),297–303, 2010.

[2] A. N. Lagarkov and K. N. Rozanov. High-frequency behavior of magnetic composites. *J. Magn. Magn. Mater.*, 321(14),2082–2092, 2009.

[3] X. C. Tong. *Advanced materials and design for electromagnetic interference shielding.* CRC Press, 2009.

[4] H. S. Cho. M-Hexaferrites with planar magnetic anisotropy and their application to high-frequency microwave absorbers. *IEEE Trans. Magn.*, 35(5),3151–3153, 1999.

[5] L. Deng and M. Han. Microwave absorbing performances of multiwalled carbon nanotube composites with negative permeability. *Appl. Phys. Lett.*, 91(2),023119, 2007.

[6] X. F. Zhang, P. F. Guan, and X. L. Dong. Transform between the permeability and permittivity in the close-packed Ni nanoparticles. *Appl. Phys. Lett.*, 97(3),033107, 2010.

[7] L. Yan, J. Wang, X. Han, Y. Ren, Q. Liu, and F. Li. Enhanced microwave absorption of Fe nanoflakes after coating with SiO_2 nanoshell. *Nanotechnol.*, 21(9),095708, 2010.

[8] W. Liu, W. Zhong, H. Y. Jiang, N. J. Tang, X. L. Wu, and W. Y. Du. Synthesis and magnetic properties of $FeNi_3/Al_2O_3$ core-shell nanocomposites. *Eur. Phys. J. B*, 46(4),471–474, 2005.

[9] X. G. Liu, D. Y. Geng, H. Meng, P. J. Shang, and Z. D. Zhang. Microwave-absorption properties of ZnO-coated iron nanocapsules. *Appl. Phys. Lett.*, 92(17),173117, 2008.

[10] X. F. Zhang, P. F. Guan, and X. L. Dong. Multidielectric polarizations in the core/shell Co/graphite nanoparticles. *Appl. Phys. Lett.*, 96(22),223111–223114, 2010.

[11] J. Liu, J. Cheng, R. Che, J. Xu, M. Liu, and Z. Liu. Double-shelled yolk–shell microspheres with Fe_3O_4 cores and SnO_2 double shells as high-performance microwave absorbers. *J. Phys. Chem. C*, 117(1),489–495, 2013.

[12] X. F. Zhang, H. Huang, and X. L. Dong. Core/shell metal/heterogeneous oxide nanocapsules: the empirical formation law and tunable electromagnetic losses. *J. Phys. Chem. C*, 117(16),8563–8569, 2013.

[13] F. Qin and C. Brosseau. A review and analysis of microwave absorption in polymer composites filled with carbonaceous particles. *J. Appl. Phys.*, 111(6),061301, 2012.